DISSERTATION

"Development of a non-destructive beam-profile monitor based on scintillating fibre planes and SIPMs"

Ausgeführt zum Zwecke der Erlangung des akademischen Grades eines
Doktors der technischen Wissenschaften, unter der Leitung von

Priv.-Doz. Dipl.-Ing. Dr. Johann Marton

Stefan-Meyer-Institut für subatomare Physik
der Österreichischen Akademie der Wissenschaften

Eingereicht an der Technischen Universität Wien,

Fakultät für Physik

von

Mag. rer. nat. Mariana Rihl
Matrikelnummer 0500889

Begutachtet von

Dipl.-Ing. Dr. Werner Riegler	und	Prof. Dr. Peter Krizan
CERN, EP-AIO		University of Ljubljana,
		Department of Physics

Vienna, February 2018

"Learn what the rest of the world is like. The variety is worthwhile."
- Richard Feynman

Abstract

CERN's Large Hadron Collider (LHC) is currently the largest particle accelerator in the world. To ensure particle energies at LHC's design values and enable collisions at high energies, the working settings and beam parameters are constantly monitored by the beam instrumentation division. The aim of this thesis is to present a new type of detector to monitor one such beam parameter, the transverse beam profile, and to present the results of an analysis of another beam attribute which reduces the luminosity of collider experiments.

Part one of this thesis introduces a detector that uses beam-gas interactions to measure the transverse beam profile. The design of the detector is described in detail and the various components that ensure data quality are introduced. Tests that were conducted to investigate the performance of the detector, like timing and efficiency parameters, are presented as well.
The first part is concluded with a summary of the work performed on the detector so far and an outlook of future tasks, use, and applications.

Part two introduces the concept of longitudinally stray charges in the LHC, called ghost charges. It is described how those ghost charges occur, why they have an impact on the luminosity of collider experiments, and how they are measured.
Ghost charge data for three different beam types (protons at intermediate energy, high energy and lead beams) are presented. The results can be used to correct the measured luminosity values for the three types of beams.
A summary of the results concludes the second part of the thesis.

Kurzfassung

Der große Hadronen-Beschleuniger (*engl.* Large Hadron Collider, LHC) am CERN, der Europäischen Organisation für Kernforschung, ist derzeit der größte Teilchenbeschleuniger der Welt. Um die geplanten Teilchenenergien zu erreichen, werden die Einstellungen des Beschleunigers und Eigenschaften des (Protonen-)Strahls kontinuierlich von der Abteilung der Strahldiagnose (beam instrumentation) überprüft.

Das Ziel dieser Arbeit ist es, einen neuen Typ von Teilchendetektor vorzustellen, der das transversale Strahlprofil messen und beobachten kann. Weiters werden die Analyseergebnisse der Messung einer anderen Strahleigenschaft präsentiert, die die Luminosität von Kollisionsexperimenten vermindert.

Der erste Teil der Arbeit stellt einen neuen Teilchendetektor vor, der Interaktionen von Strahl und Gas misst, um das transversale Strahlprofil zu eruieren. Das Design des Detektors wird detailliert beschrieben, und verschiedene Komponenten, die eine gute Datenqualität sichern, werden vorgestellt. Weiters werden Tests vorgestellt, die durchgeführt wurden, um die Leistungsfähigkeit des Detektors zu untersuchen. Zu diesen Tests gehört die Untersuchung der genauen Zeiteinstellungen für die unterschiedlichen Komponenten und die Vermessung der Pulshöhenspektren.

Der erste Teil wird mit einer Zusammenfassung der vervollständigten Arbeiten und einem Ausblick auf zukünftige Aufgaben, Möglichkeiten und Anwendungen abgeschlossen.

Im zweiten Teil der Arbeit wird das Konzept der "Geisterladungen" (*ghost charges*) im LHC, Ladungen die in longitudinaler Richtung diffundiert sind, vorgestellt. Es wird erklärt, wie und warum diese Ladungen entstehen, wie man sie messen kann, und weshalb sie einen Einfluss auf die gemessene Luminosität haben.

Es werden die Daten von Geisterladungen von drei verschiedenen Strahlentypen (Protonen mit mittlerer und hoher Energie, sowie Blei-Ionen) präsentiert. Die Ergebnisse dieser Geisterladungsmessungen können dazu verwendet werden, die gemessene Luminosität für diese drei Typen von Strahl zu korrigieren.

Eine Zusammenfassung der Ergebnisse schließt den zweiten Teil der Arbeit ab.

Contents

1. Introduction

CERN, the European Organization for Nuclear Research, hosts the Large Hadron Collider (LHC), currently the largest particle accelerator in the world. Among the achievements since the foundation of CERN are the discovery of $W-$ and $Z-$Boson, weak neutral currents, light neutrinos and most recently the Higgs-Boson.

While the discovery of the Higgs-Boson completed the Standard Model of particle physics, theories beyond the standard model still lack experimental proof. To find new particles, the LHC increased the energy and luminosity during the beginning of Run 2 (which started in March 2016). In order to achieve higher energies and high luminosity, the beam parameters have to be well known and adjusted. Beam instrumentation is thus an important factor in running the LHC at its maximum design values.

The aim of this thesis is to present a novel beam-imaging detector that was installed at the LHC during the long shut-down between 2012 and 2016. In addition, results from specific data acquisitions are presented that use a very similar concept as the new beam-imaging detector.

Chapter 2 is an introduction to CERN and some of the concepts and tools that are relevant for this thesis.

Section 2.1 comprises a short overview of CERN's accelerator complex, while section 2.2 explains the concept of luminosity in collider experiments.

Several beam profile monitors that are used in the LHC, are highlighted in section 2.3. Their advantages and limits are also mentioned.

Section 2.4 presents LHCb, one of the four large experiments at the LHC, which was used to acquire some of the data presented in this thesis and also served as blue print for some of the data acquisition technology used for the new beam imaging detector.

Chapter 3 is dedicated to the *Beam-Gas-Vertex Detector*, BGV, the new transverse beam profile monitor, installed at the LHC.

Section 3.1 includes a description of the design of the detector with the expected particle energy distribution.

In section 3.2, the different components of the detector, consisting of a vacuum chamber and scintillating fibre modules, are described in detail. Another important aspect of the

detector is the reliably working read-out chain, which is presented in section 3.3 and explains the function of all of the different components and adaptions to the relevant hardware components.

In order to control the whole detector remotely, a control system was set up. This system allows for all relevant devices to be turned on through one master panel and represents all tuneable hardware components digitally. It is presented in section 3.4.

During commissioning of the detector, several relevant parameters for efficient and qualitative data taking were tested. These parameters include time propagation and sampling in the different hardware components like readout chip, analog-digital conversion boards, trigger delays and control boards to propagate the trigger correctly. The different tests and results are presented in the subsections of section 3.5.

To ensure the quality of the data, the combination of the external trigger with the timing and fast control board had to be calibrated. The calibration process and results are presented in section 3.6.

Section 3.7 describes the process to measure photon electron peaks with the complete detector setup. The parameters to acquire the data are shown as well as the corrections that had to be applied to analyse the data. The photon electron peak distances are given after explaining the different steps of the analysis.

Chapter 4 presents so-called "*ghost charges*", which can be measured by different beam instrumentation tools and have an impact on the efficiency of collider experiments.

The theory behind these charges, how they are defined, and what impact they have on the total luminosity of a run is explained in section 4.1.

The different tools to measure ghost charges are presented in section 4.2, with an emphasis on the methods used to obtain the data in this thesis.

An overview of the measurements taken into account for the analysis is given in section 4.3.

In section 4.4 the procedure to analyse the data and evaluate the errors is explained.

Sections 4.5 to 4.7 present the results of the ghost charge analysis for dedicated luminosity runs at different energies and with different interaction particles (protons and lead ions) taken in 2015.

Finally, a summary and outlook of the presented topics concludes this thesis.

2. CERN and Beam Instrumentation at the LHC

2.1. CERN and the LHC accelerator complex

CERN, the European Organisation for Nuclear Research near Geneva, has provided the infrastructure for many different particle physics experiments over the last 60 years. The Large Hadron Collider (LHC) is CERN's biggest particle accelerator. It has been built to provide particle collisions at high energies which allow experiments to look into unsolved physics questions.

There are eight arcs and eight straight sections at the LHC, four of which are collision points. The detectors at these interaction points are equipped with detectors and are referred to as experiments. The four big experiments at the LHC are called ATLAS, CMS, ALICE and LHCb.
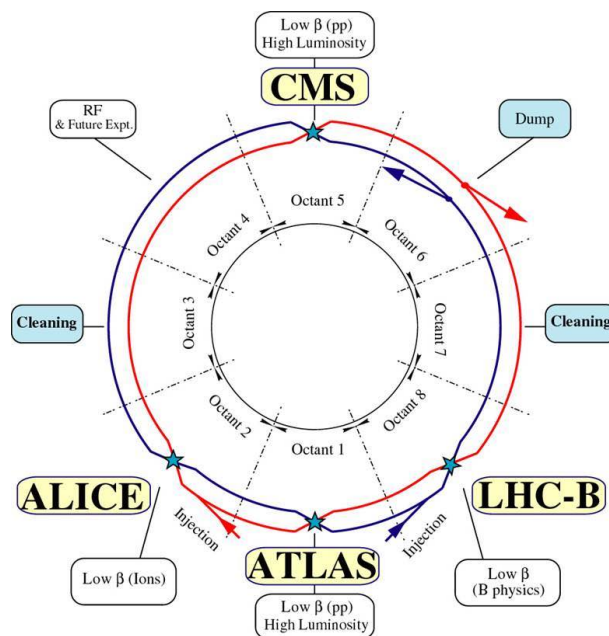

Figure 2.1.: Schematic view of the Large Hadron Collider at CERN with its four large experiments and injection direction of the two beams. Source: P. Lefèvre [1].

The positions of the four experiments at the 27 km long LHC as well as the position of
beam injection and beam dump are displayed in figure 2.1.

The LHC synchrotron is designed to store and accelerate particles from 450 GeV to 7 TeV.
This means that particles need to be accelerated in a so-called "accelerator chain" before
they can be injected into the LHC. The LHC accelerator chain is shown in figure 2.2 and
consists of the following accelerators for protons:

The **Linac2** is a linear accelerator which accelerates the protons from the proton source
to 50 MeV. From the Linac2, the protons enter the **Booster**, a small proton synchrotron
which accalerates the protons to about 1.4 GeV before injecting them into the **Proton
Synchrotron (PS)**. The protons in the PS get accelerated up to 25 GeV before being
transferred either directly to non-LHC experiments or into the next larger accelerator in
the LHC accelerator chain, which is the **Super Proton Synchrotron (SPS)**. The SPS
then accelerates the particles to 450 GeV, which is the design injection energy for the
LHC. The particle energy in the LHC can currently reach a maximum of 6.5 TeV [2],
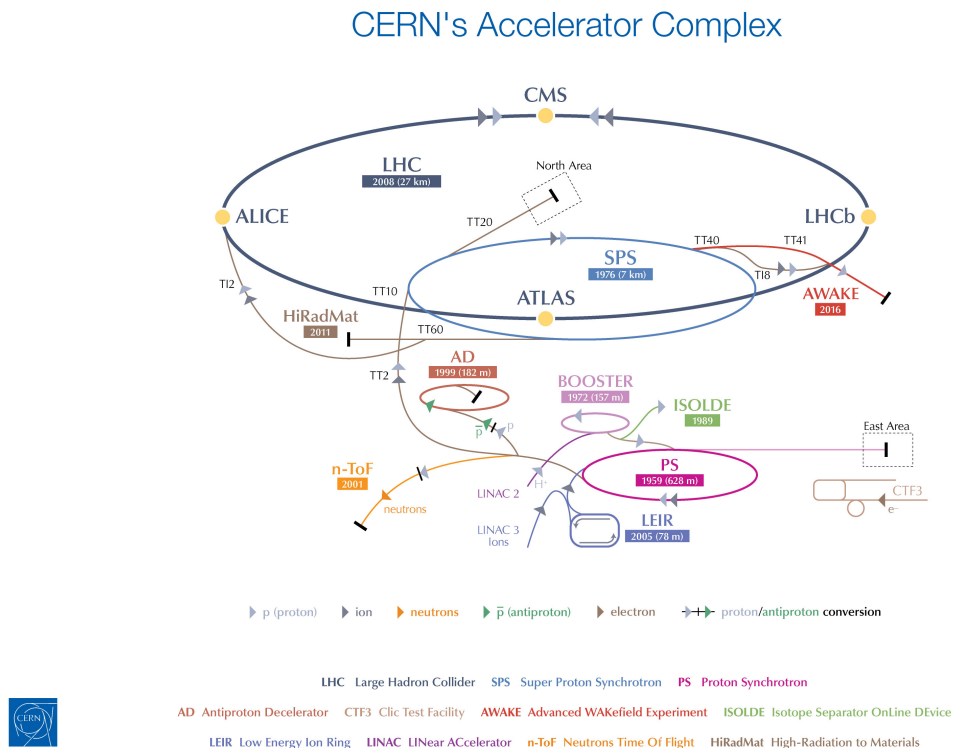which is close to the design value of 7 TeV [3].

Figure 2.2.: The CERN accelerator complex with the LHC injector chain and non-LHC
accelerators and experiments. Source: F. Marcastel [4].

The injection chain for lead ions is similar to the chain described above. However, lead ions are accelerated in the Linac3 and the Low Energy Ion Ring (LEIR) before being injected into the PS.

The beams inside the accelerator complex are bunched and there is a different number of bunches and different bunch spacings in the accelerators leading up to the LHC. The LHC itself has 3564 bunch slots - spaces to accomodate bunches - and is designed to accelerate 2808 bunches containing about 10^{11} protons each, with a minimum distance of 25 ns.

The remaining empty slots serve as additional time for injection and dump kicker elements in the whole accelerator chain.

The beams can be diagnosed with a variety of instruments. Some beam profile monitors (a subsection of beam diagnostics instruments) like wire scanners and synchrotron radiation monitors, are described in more detail in section 2.3.

2.2. Luminosity

There are two quantities in a particle collider experiment that are important for the output of a large sample of produced particles from an interaction. The first one is the centre of mass energy at the interaction point (IP), written as $\sqrt{s}$, the other one is luminosity $\mathcal{L}$, a parameter that relates the production rate R of particles per unit of time to the production cross-section σ_p (the probability of two particles interacting) at the IP. The instantaneous luminosity is defined as

$$\mathcal{L} = \frac{R}{\sigma_p} \tag{2.1}$$

with the units $[\text{cm}^{-2}\text{s}^{-1}]$.

The beams in the LHC are bunched and the bunches are focused in the transverse dimensions before colliding in the IP [5]. The luminosity for one colliding bunch pair is given by

$$\mathcal{L} = 2c\, N_1 N_2\, f_{rev}\, \cos\phi \int \rho_1(x,y,z,t)\, \rho_2(x,y,z,t)\, dx\, dy\, dz\, dt, \tag{2.2}$$

where N_j is the number of particles per colliding bunch for beam $j = 1, 2$, f_{rev} is the revolution frequency and $2c$ a kinematic factor (with c being the speed of light), assuming relativistic velocities of the beam particles. The ρ_j are normalised particle density functions and ϕ is the half crossing angle between the two beams. Since ϕ is very small at the LHC IPs, $\cos\phi \simeq 1$.

Assuming the transverse beam profile to be a Gaussian distribution, equation 2.2 can

be solved as is presented in detail in [6]. The luminosity for two idealistic and identical Gaussian bunches with the same σ in both transverse directions in a head-on collision can then be expressed as

$$\mathcal{L}_{gauss} = \frac{N_1 N_2}{4\pi\sigma^2} \cdot f_{rev} \,, \tag{2.3}$$

with σ being the transverse size of the beam.

To achieve a high $\mathcal{L}_{gauss}$, the respective parameters of equ. 2.3 can be adjusted. The number of particles per bunch is limited by the number of particles that can be put into one bunch and decreases during the duration of a fill. The revolution frequency is a fixed accelerator parameter for the LHC and cannot be further increased. As a result, to increase $\mathcal{L}_{gauss}$, the transverse beam size has to be small.

In the case of negligible dispersion, the beam width is related to the transverse emittance ϵ and the beam optics parameter β^* [6]:

$$\sigma^2 = \epsilon\beta^* \quad . \tag{2.4}$$

While β^* is the result of the beta-function at the IP and thus a constant, the emittance ϵ is defined as the area of the phase space ellipse of the motion of the particle ensemble in the (x, p_x)- or (y, p_y)-plane [7]. The emittance needs to be kept small to achieve small beam sizes. It is therefore crucial for the performance of the accelerator to be able to monitor and understand the behaviour of the transverse beam sizes.

2.3. Beam Profile Monitors at the LHC

The ideal goal of beam profile monitors at the LHC are fast, precise, continuous non-invasive measurements of the absolute bunch-by-bunch beam size through a machine cycle. There are many different types of beam profile monitors used at the LHC which complement each other to achieve that goal [8]. The beam profile monitors most commonly used at the LHC are briefly described in this section.

One of the most stable methods to acquire the 1-dimensional transverse beam profile uses wire scanners. These consist of a (carbon) wire with a diameter of the order of 10 μm which is moved through the beam. At high energies, secondary particle showers caused by interactions between the wire and the beam, are detected with scintillators and photomultipliers (PMTs) outside the vacuum of the beam line. The correlation between the wire position and the detected signal rate gives the transverse beam profile [9, 10]. Since the measurement of the transverse beam profile with the wire scanner is proven to

be a reliable method, it is frequently used to calibrate other tools.

Limitations of wire scanners can be the resolution due to unwanted vibrations during the passage of the wire through the beam, the damage of wires due to heat and radiation damages [11] as well as superconducting magnet quenches caused by particle showers. This effect can occur at high energies and limits the intensity at which wire scanners can still be used.

A different approach to measuring the beam width is the beam synchrotron radiation telescope (BSRT), which makes use of synchrotron radiation. This radiation is a special form of bremsstrahlung and occurs when a relativistic, charged particle deviates from its path due to a magnetic field that acts on the particle. At the LHC there is one BSRT per beam. The synchrotron light gets emitted by the beam passing through an undulator (for low beam energies, e.g. at injection) and a dipole magnet (for high beam energies). The photons, which are in the visible wavelength range, get redirected with an extraction mirror from the beam line onto an optical table [12]. The optical components on the table allow for the splitting of the photon beam to send the light to measure the longitudinal attributes of the particle beam. One of these tools is the longitudinal density monitor (LDM)[1], where the single photons from the synchrotron light are measured with an avalanche photodiode detector, see also section 4.2. To measure the transverse beam profile, after passing through several focusing lenses that are also installed on the optical table, the synchrotron photons pass onto a photocathode which is connected to a microchannel plate (MCP). The MCP multiplies the electrons from the photocathode, which get accelerated onto a phosphor screen. The intensified image is then captured by a CCD camera.

This telescope is the only beam profile monitor presented here, that can simultaneously measure the longitudinal and transverse profile of the beam. It is limited in transverse resolution by the geometry of the sources of the synchrotron light (undulator or dipole magnet). Heating, caused by the extraction mirror, is another limiting factor to this profile measurement [13].

Another method to measure beam profiles uses rest gas in the LHC. The ionisation profile monitor (IPM[2]) measures electrons that are produced through ionisation. These ionisation electrons are produced in a small volume by injecting neon gas into the LHC vacuum during beam circulation. The electrons are accelerated in an electric field which is provided by two electrodes with a potential difference of 4 kV. A MCP in the electric field amplifies the electron shower before it hits a phosphor screen. The photons from the phosphor screen pass through a right-angle prism to change their direction. They then

---

[1]The LDM is referred to as BSRL in LHC official documents.
[2]Also referred to BGI, beam gas ionisation monitor in LHC official documents.

pass through a window out of the vacuum and are measured by a CCD camera.

In order to keep the transverse spread of the ionisation electrons low, a magnetic field with field lines along the electric field is applied. [14].

While the IPM provides a good signal and precise transverse profiles, it is prone to high currents in the MCP due to electron clouds, saturation of the MCP and artefacts of the camera. In addition, it has limitations during the ramping and squeezing of the beam [8].

Another way of using residual gas is the measurement of interaction vertices between the beam and the gas with scintillating fibre mats and photon detectors. This method, called the beam-gas vertex detector (BGV) is the main subject of the present thesis and is described in chapter 3.

2.4. The LHCb experiment at CERN

2.4.1. Overview

LHCb, "a Large Hadron Collider Beauty" experiment, is one of the four large experiments at the LHC. It is located at interaction point 8, as is shown in figure 2.1.

LHCb investigates heavy flavour physics and different sectors of CP violation to understand why there is an asymmetry between antimatter and matter in our universe. In addition, it looks for physics beyond the standard model (BSM) and, if found, seeks to explore such phenomena [15, 16].

The mass of the beauty and charm containing mesons is small, compared to the centre of mass energy of the colliding beams. As a result, these produced mesons remain close to the beam line. The LHCb detector is built as a single-arm spectrometer to cover the space through which the beauty and charm containing mesons are travelling. A schematic of the detector is shown in figure 2.3.

The beams collide in the interaction point, indicated by z=y=0 in figure 2.3. The interaction vertices are detected by the VErtex LOcator (VELO), which consists of silicon strip detectors and is described in more detail in section 2.4.2.

The first Ring Imaging CHerenkov detector (RICH1) is located directly behind the VELO and followed by the Tracker Turicensis (TT).

The particles produced in the interaction then pass through a dipole magnet, where their trajectories are bent depending on their charge and momentum.

Behind the magnet are three tracking stations (T1-T3), the second RICH (RICH2) and the calorimeter system, consisting of a scintillating pad detector and a pre-shower detector
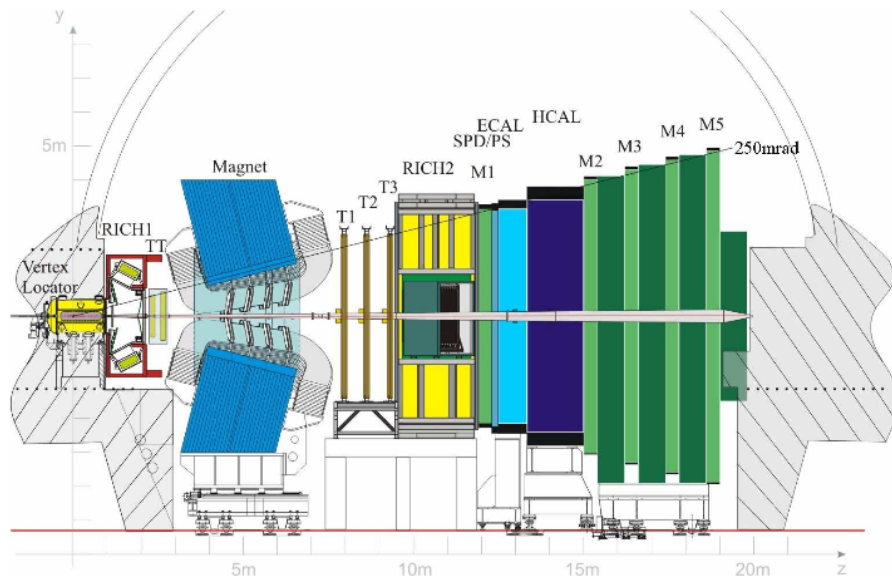
Figure 2.3.: Cross section of the LHCb detector with the different sub-detectors. The interaction point is on the left side of the drawing with z=y=0. Source: [17].

(SPD/PS) and the electromagnetic and hadronic calorimeters (ECAL and HCAL). The detector is completed with the muon detectors (M1-M5).

2.4.2. The VErtex LOcator

The VELO measures the interaction vertices. These vertices can originate from different types of interactions like collisions between two beam bunches, beam-gas interactions or decaying particles.

It consists of two halves which can be retracted during beam injection and ramping and are put into closed position when the LHC is in "stable beams" mode. Inside each half there are 21 silicon strip modules, each containing a R- and a ϕ-measuring sensor, that are mounted back to back. They measure the radial distance R from the beam line and the azimuthal angle ϕ respectively. A drawing of the detector module is shown in figure 2.4.

The modules are mounted perpendicularly to the beam line, see figure 2.5 and are as close as 8 mm from the beam when the VELO is closed. The silicon strip sensors are read out with "*Beetle chips*", which are radiation-hard, analog readout chips, developed for the LHCb experiment [19]. The VELO readout system is re-used for the BGV readout chain and will be described in more detail in section 3.3.
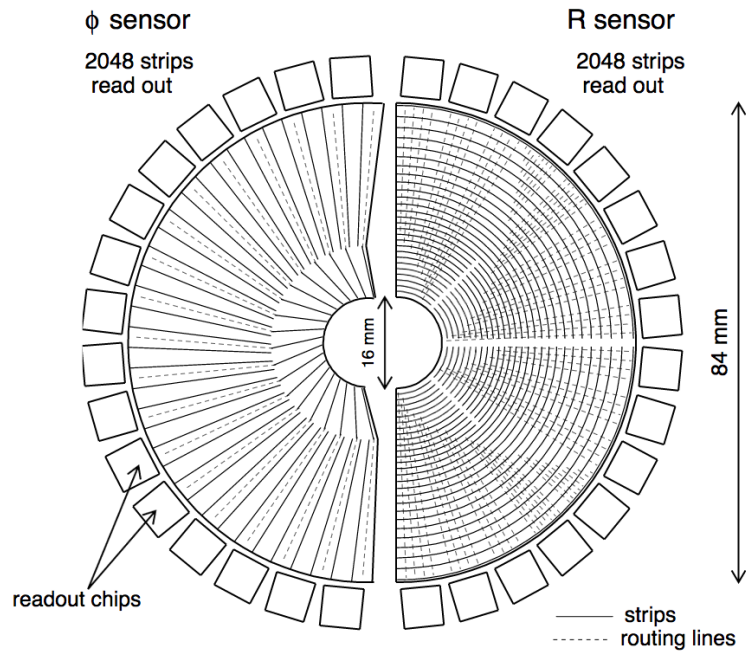
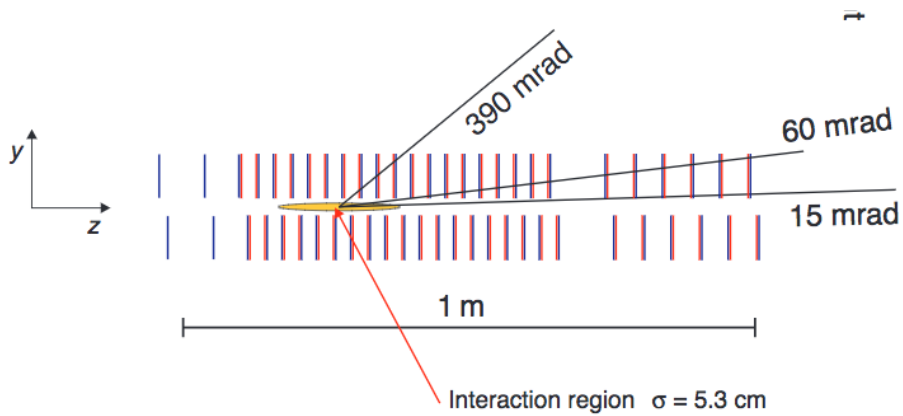Figure 2.4.: Schematic drawing of two sensors with R- and ϕ measuring strips. Source: [18].

Figure 2.5.: Cross section of the closed VELO in x-direction. Only the z-direction (longitudinal) is respecting the given scale. The luminous region as well as the silicon hybrids have different dimensions than displayed. Source: [18].

3. Beam-Gas-Vertex Detector

3.1. Design Considerations

Several beam profile monitors were introduced in section 2.3. While they are all valuable tools to monitor the LHC beams, they face certain limitations related to the beam's properties. The beam-gas vertex detector (BGV) was designed, built and installed close to LHC's point 4 to complement the different monitors in order to measure the transverse beam profile at all states and energies of the LHC.

The BGV is based on the beam-gas imaging (BGI) method that is used at LHCb to measure the luminosity during dedicated fills. Hereby, neon gas is injected into the LHC vacuum and the charged particles produced by the interactions of protons (or lead ions) with the neon nuclei are detected in tracking stations. It is then possible to derive the interaction vertices from the measured tracks. The spatial distribution of these interaction vertices then provides an image of the (transverse) beam width. The concept of measuring beam-gas vertices with the BGV is shown in figure 3.1.
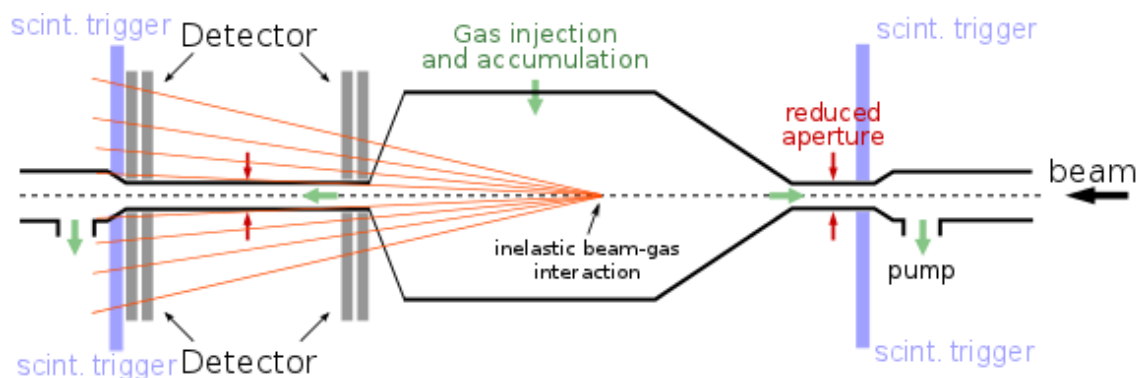

Figure 3.1.: Concept of beam-gas interactions in detector volume and detector modules. P. Hopchev [20]. The dimensions of the BGV are different than displayed.

As can be seen in figure 3.1, part of the standard LHC beam pipe is replaced with a vessel that accommodates the gas target. The aperture of the beam pipe is reduced just

before and after the target chamber to allow for the tracking detector stations, which are located outside the beam pipe, to be closer to the beam.

The particles produced during these interactions are mainly charged pions and photons from neutral pion decays. The energy of the outgoing particles goes up to the nominal beam energy (450 to 7000 GeV) [21], as is shown in the distribution plots in figure 3.2.

All particle tracks undergo multiple scattering while passing through matter. This is expected to limit the track extrapolation error on average more than the detector resolution. Some particles interact in the material and produce secondary particles which reach the detector (about 60 hits per beam-gas interaction event), thus degrading the vertex resolution [22].
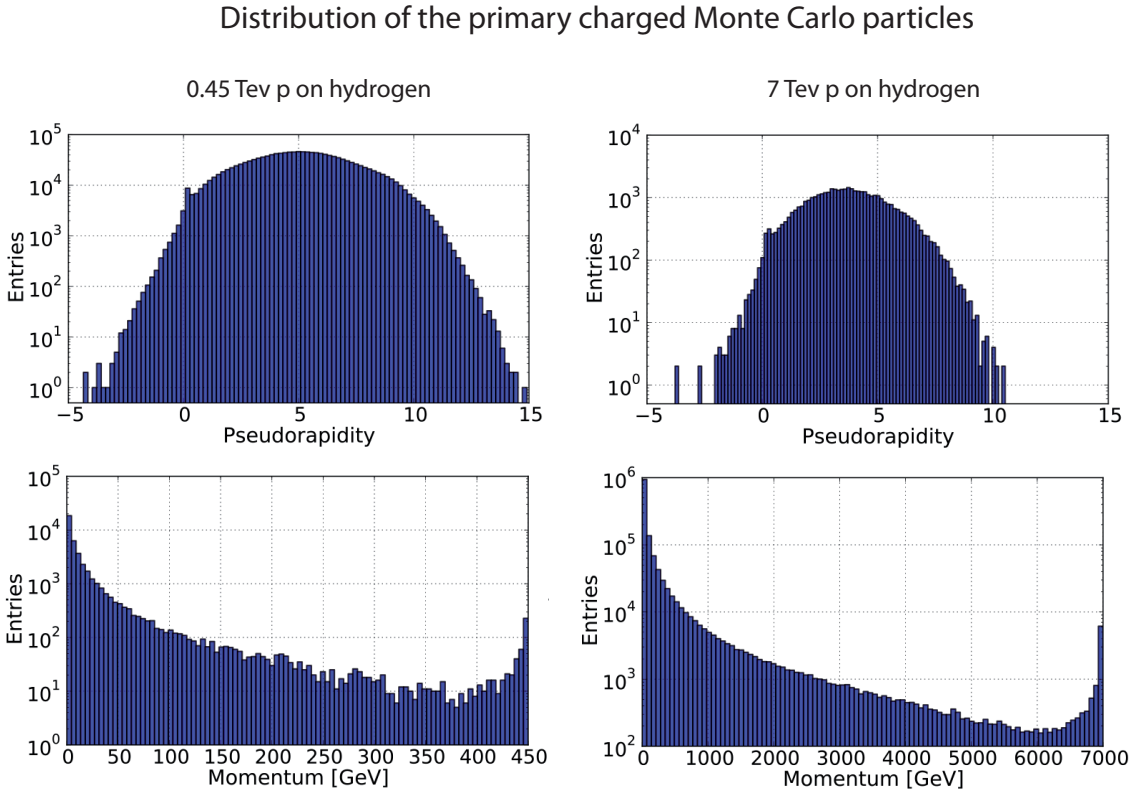

Figure 3.2.: Momentum and pseudorapidity distribution of the primary charged Monte Carlo particles of interactions between 450 GeV protons and hydrogen gas on the left and 7 TeV protons and hydrogen on the right. P. Hopchev [21].

The tracking stations to measure the interactions between the beam and the gas are made out of 8 scintillating fibre modules, each containing two fibre planes, where one mat is rotated by 2° to the other one. The light of the fibres is read out with silicon

photomultipliers (SiPMs).

Simulations show that the BGV vertex resolution is dominated by multiple scattering [22]. In order to reduce the material close to the interaction point, modules with 4 layers of scintillating fibres were installed in the station close to the target vessel ("near station") while 5-layer modules were installed at the station 1 m from it ("far station"). The expected number of photoelectrons per minimum ionising particle (MIP) is around 20 for the 4-layer modules and 25 for the 5-layer modules before fixing a mirror to one side and 28 to 35 photoelectrons with a mirror [23].

Since the detector modules are installed as close as possible to the beam pipe, radiation does have an impact on the modules. Similar to LHCb SciFi tracker SiPMs, the expected yearly dose for the BGV SiPMs is of the order of 10 Gy [24, 25]. The expected impact of the radiation on the scintillating fibre mats is too low to cause a substantial loss of light yield in the fibres, even close to the beam pipe. However, radiation will over time cause an increased dark current rate in the SiPMs and potentially cause more noise clusters. While the detector has a large enough light yield that the increased dark current should not interfere with the actual hits, the reduction of noise clusters is preferred. Due to these predicted effects, a cooling system was designed to cool down the SiPMs to temperatures as low as $-40°$ C and thus reduce the dark current.

3.2. Detector

3.2.1. Target volume and detector modules

The target chamber of the BGV is about 3 m long, 20 cm wide, and tapered, as is shown in the BGV layout in figure 3.3. It provides an effective target length of about 1 m. The target chamber is made out of aluminium and has an exit window that was produced in such way that the radiation length x/X_0 is reasonably small (about 1 % or less) to reduce scattering of the particles which exit in a polar angle between 10 and 100 mrad [26].

At the same time, the exit window has to be very stable to withstand atmospheric pressure.

The interactions between the protons (or Pb-ions) and the neon gas are measured with scintillating fibre modules which are installed outside of the LHC vacuum pipes. The scintillating fibre mats and photodetectors were developed in close collaboration with the Scintillating Fibre (SciFi) Tracker project of the LHCb upgrade [25].

Kuraray SCSF-78MJ scintillating fibres with a 250 μm (246$\pm$6 μm) diameter and a length of $240 - 340$ mm are glued into tightly packed mats of 4 and 5 layers respectively, see figures 3.4 and 3.5.
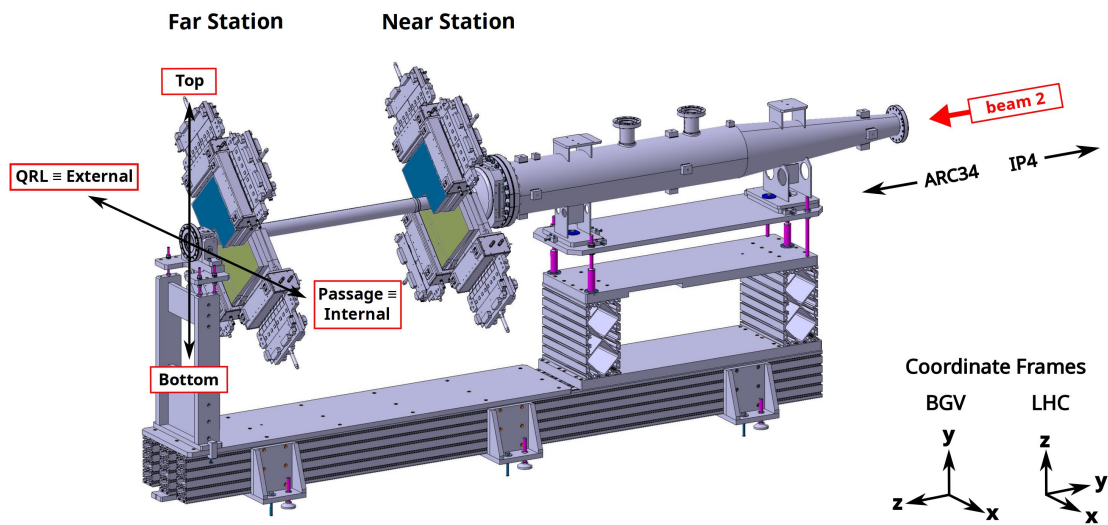
Figure 3.3.: Layout of the BGV with the gas target vessel on the right and the two tracking detector stations on the left. P. Hopchev [20].
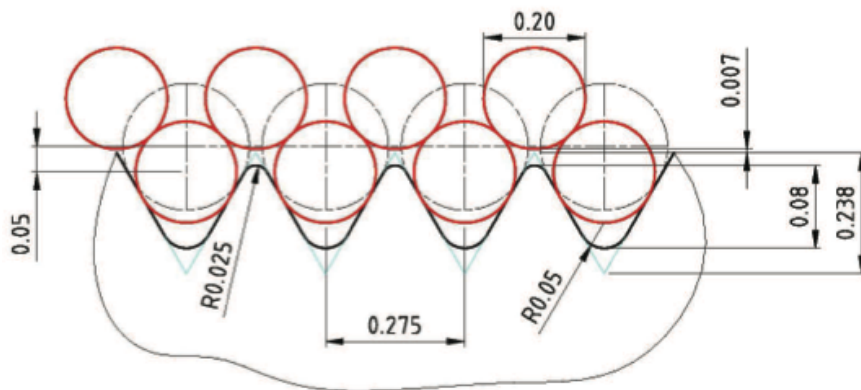

Figure 3.4.: Schematic of fibres guided in winding grooves to be wound into mats. The displayed fibre diameter is smaller than the actual fibre diameter. Source: T. Kirn [27].
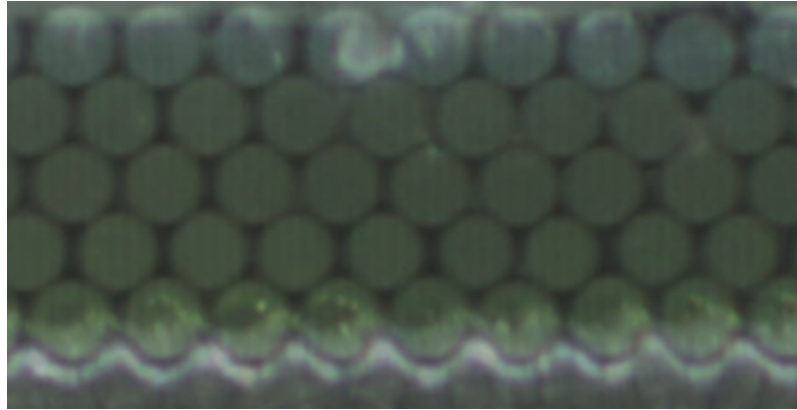
Figure 3.5.: Photo of glued fibre mats with 5 layers. Source: T. Kirn [27].

The glue to pack the fibres into mats is Epotek 301, loaded with 25% TiO_2 to minimise crosstalk between the fibres [27]. A mirror is fixed on one end of the fibres to increase the light yield.

The fibre mats have the dimensions of about 340×260 mm with a cutout of 98×98 mm to allow for the modules to be installed close to the beam pipe, thus covering the area around it, and provide an overlap between the top and bottom modules. A drawing of the whole module including fibre mat dimensions, cooling outlets and front-end electronics is shown in figure 3.6. Figure 3.7 shows how the four modules of one tracking station are aligned to cover the surface around the beam pipe. A photo of a two module assembly is shown in figure 3.8. The black surface with the cutout covers the SciFi mats to make sure that the SiPMs only detect photons from particle interactions. The green front-end boards contain the attenuator circuit, the Beetle chips, as well as connections for data output and detector control.

The modules are read out with SiPMs from Hamamatsu, model S10943-3183(x), which will be described in more detail in section 3.2.2. To attenuate the intrinsic noise from radiation damage, the SiPMs are cooled down to temperatures as low as $-40°$ C with a cooling system using C_6F_{14}. To avoid short-circuits in the SiPMs, dry air is flushed through cold boxes to inhibit condensation on the cooled SiPMs.

The BGV is triggered with two scintillator stations positioned on either side of the detector, as indicated by the blue shapes in figure 3.9. The detector modules are triggered when a particle hits the far station (downstream) scintillator. The scintillator station upstream of the BGV vessel serves as veto, reducing data acquisition of tracks emerging from vertices that were produced upstream of the gas tank.
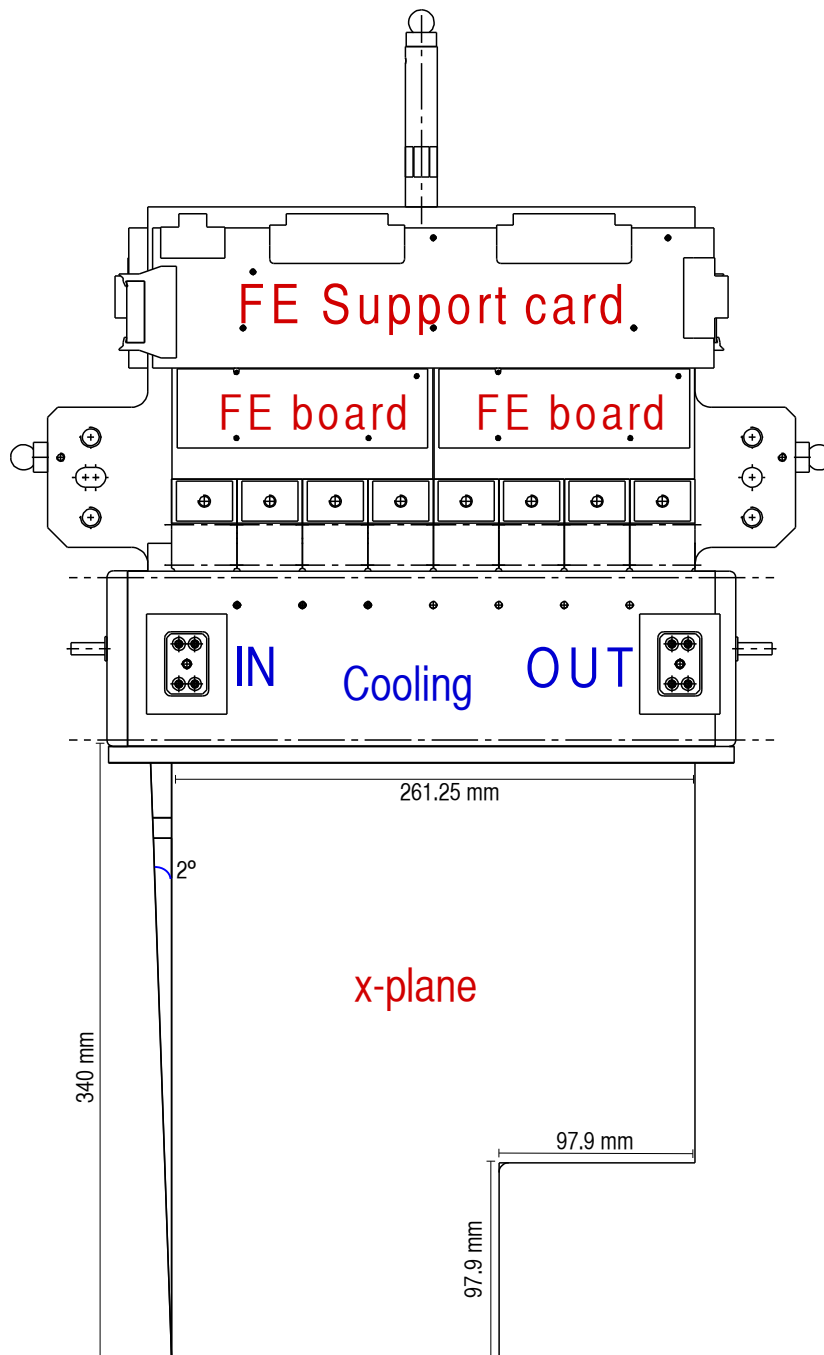
Figure 3.6.: Schematic of the complete SciFi module including cooling and front end readout boards. O. Girard [20]
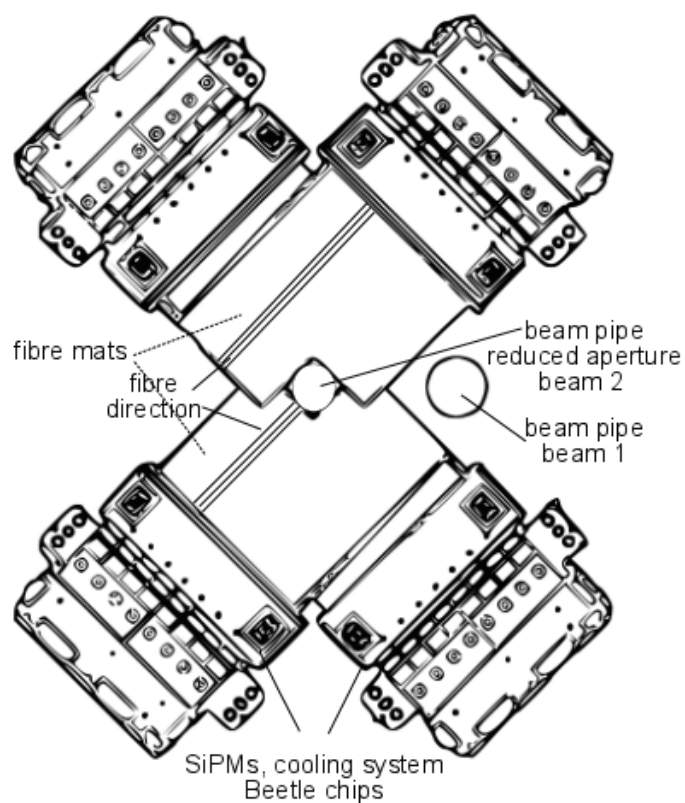
Figure 3.7.: Schematic of detector modules overlapping around the beam pipe.
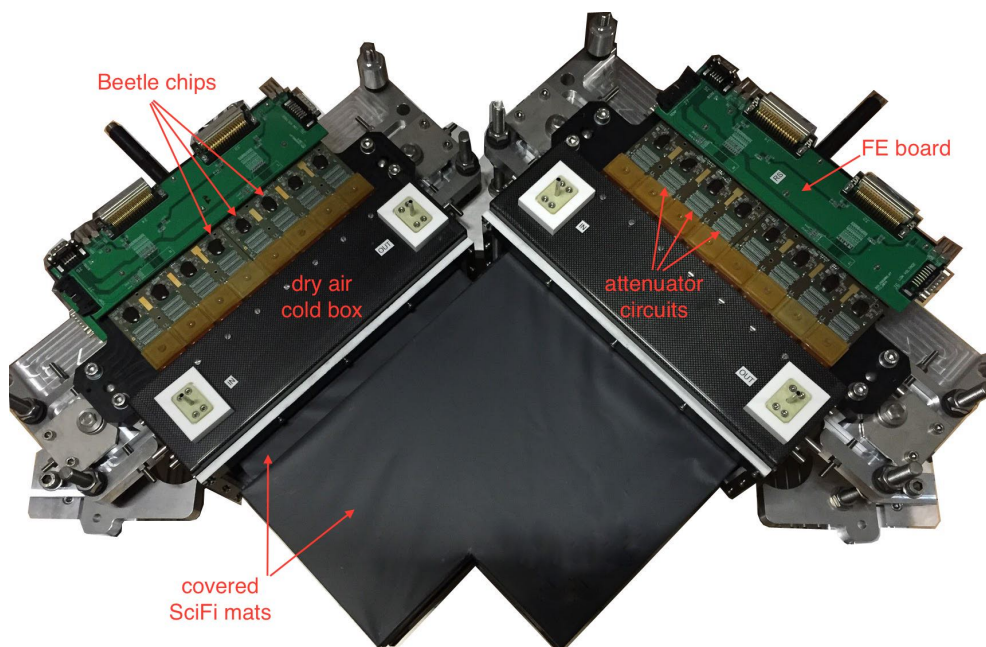

Figure 3.8.: Photo of two detector modules, ready to be mounted around the beam pipe. Photo courtesy of C. Barschel.

detector modules
beam 2   Scintillator Triggers   far station   detector modules   Gas target   Scintillator Triggers
beam 1   downstream   near station   vessel   upstream
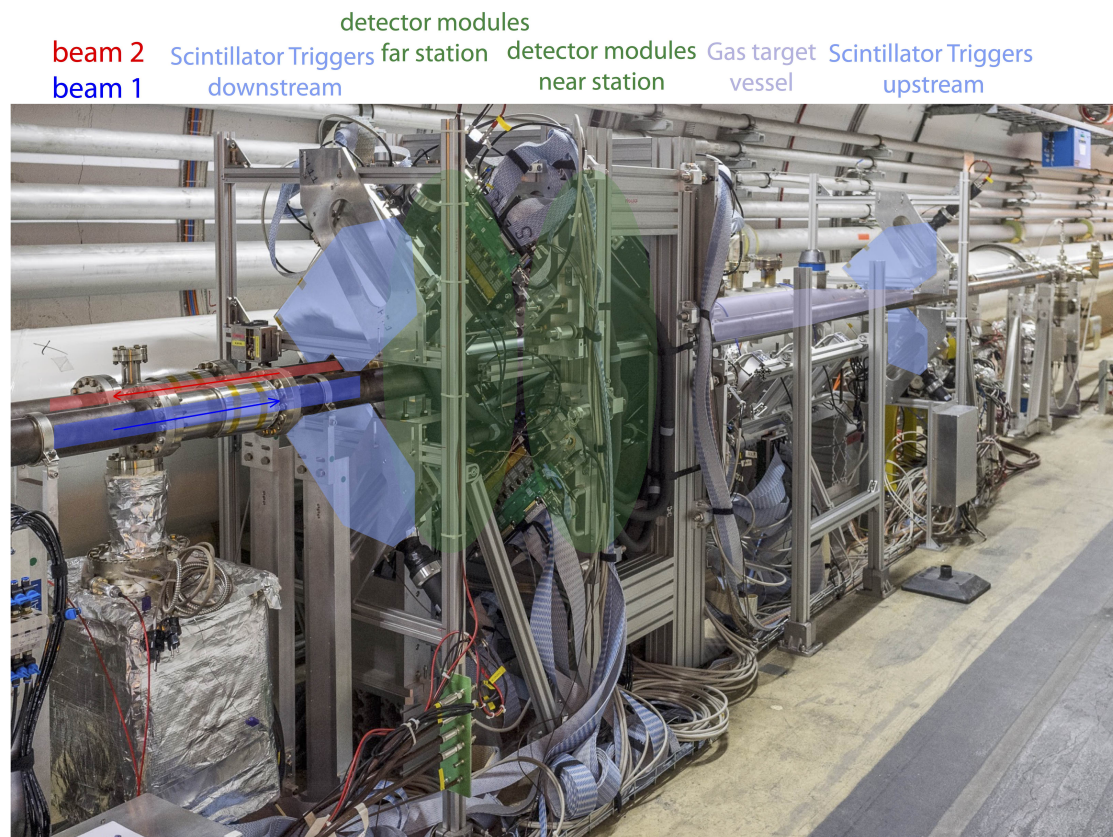

Figure 3.9.: Complete installed BGV. The position of the upstream and downstream scintillator triggers are indicated by the blue shapes, the tapered gas tank is indicated by the grey shape, and the two detector stations' positions are indicated by the two green elliptic shades.
The pipe closer to the corridor, partially shaded blue, is the pipe for beam 1 while the pipe closer to the wall, partially shaded in red, is the pipe for beam 2. The beam's directions are indicated by arrows. Photo by C. Barschel.

3.2.2. Scintillating fibres and SiPMs

The charged particles that pass through the SciFi mats deposit ionisation energy in the active core (the fibres are doped with dye). The dye is excited by only a few eV and releases a photon at relaxation. The light, which is emitted at such angles that it undergoes total internal reflection at the fibre boundaries, is guided inside the fibres to either end between the core, the cladding material and the material surrounding the fibres (e.g. glue) [25]. The fibre cores are clad with polymethyl methacrylate (PMMA) and a fluorinated polymer (FP) [28].

A highly reflective mirror is glued onto the end of the fibres that are close to the LHC pipes to increase the light yield. On the other fibre end, Hamamatsu S10943-3183(x) SiPMs are mounted to detect the photons created by the ionising charges.

These SiPMs consist of 128 channels each with 96 (4×24) pixels per channel. The channel height is 1.5 mm, while the channel width is 250 μm [29]. Figure 3.10 shows a drawing of how the fibres are connected to the SiPM channels.
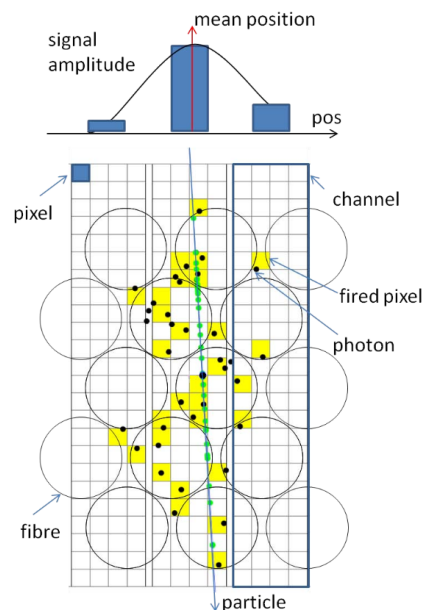

Figure 3.10.: Drawing of signal formation. The photons inside the fibre (green dots represent photons from a particle trajectory) propagate to the fibre end where they reach the SiPM. Each pixel inside a channel can detect one photon at a time. The signal per channel (which contains 96 pixels) is proportional to the amount of photons detected. The position of the particle's track is calculated from a weighted mean of the signal. The fibres are not aligned to the SiPM channels. Source: [25].

3.3. Readout

3.3.1. Readout system overview

The different readout (and control) components of the BGV are described in the following subsections. An overview of all the readout, control and detector system components is given in figure 3.11.
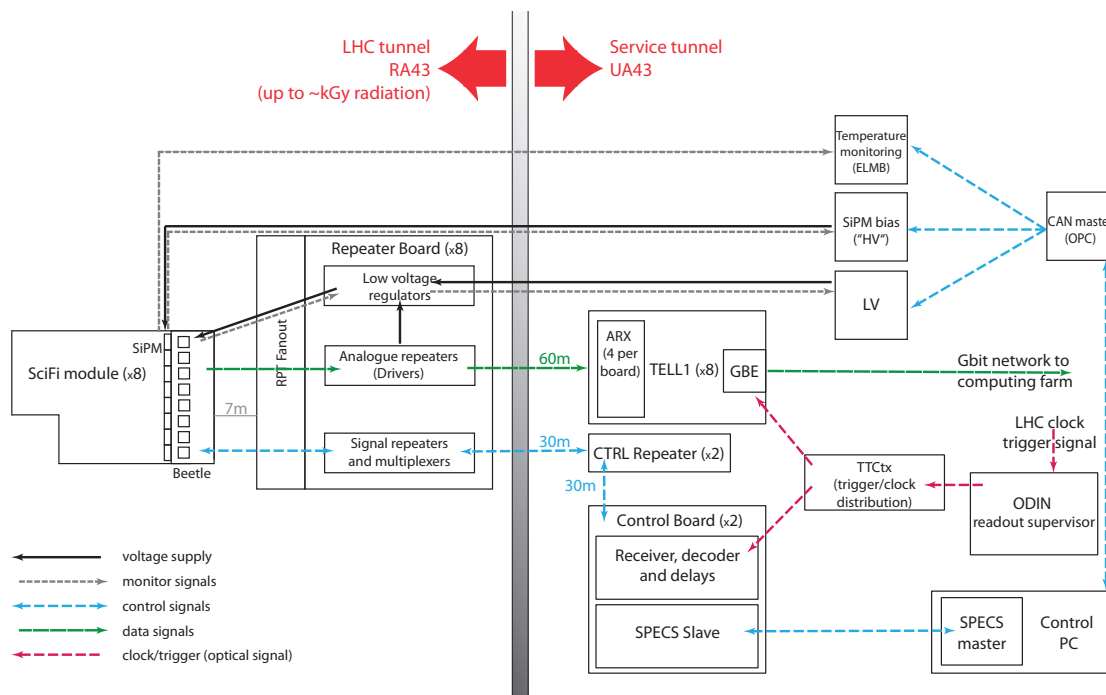

Figure 3.11.: Schematic of the different readout and control components and the trigger distribution. Based on drawings by M. Ferro-Luzzi [20] and L. Eklund [30].

The detector is configured through control computers (control PC and CAN master). The CAN master communicates with low level detector controls like the voltage supply for SiPMs and Beetle readout chips and reads back the temperature of the NTCs which are mounted on the back of the SiPMs (through an ELMB [33] system). The CAN master itself receives commands from and sends feedback about the status of its controls to the control PC .

The signals of the control PC are sent to and translated in the control boards (CTRL boards) and routed through the CTRL repeater boards, signal repeater boards (RPT boards), and RPT fanout before they configure the Beetles. The control PC also sends configuration signals to the TELL1 analogue digital converter board and the ODIN readout supervisor board, which serves as timing and fast control (TFC).

Particle interactions in the SciFi modules are read out by SiPMs (which are only controlled through the bias voltage). The Beetles then read out the signals from the SIPMs (one Beetle per SiPM) and send them through the RPT fanout and RPT boards to the TELL1 boards where the signal gets digitised. The digitised signal is then sent to the HLT computing farm for further processing.

The LHC clock and trigger (from the scintillator trigger L0) are received by and distributed through the readout supervisor board ODIN, transformed into laser signals in the TTCtx board and sent to the TELL1 and CTRL board. From the CTRL board, the clock and trigger are distributed through the control components and -cables to the Beetles. The clock, which is received by all readout components, serves as a metronome and facilitates the consolidation of the different signal travel times in the system. The timing considerations are explained in detail in section 3.5.

The radiation hard components are installed in the LHC tunnel, next to the detector while the radiation sensitive components are installed in the service tunnel that runs parallel to the LHC tunnel, 60 m from the actual detector.

3.3.2. Beetle readout chips

The SiPMs are read out with radiation hard Beetle front end chips, that were initially developed for silicon strip detectors at LHCb [19]. One Beetle transports 128 channels via four multiplexing ports called "analogue links" or a-links. Each a-link sends out 32 channels and adds 4 header bits for additional information (like data error detection and control).

One SiPM (128 channels) is connected to one Beetle through an attenuator circuit. The SiPM's signal has to be attenuated because the Beetles were designed to receive small input signals from the silicon strip detectors (about $22{\cdot}10^3$ electrons per MIP). However, the SiPM signal is about 10^7 electrons per MIP and thus needs to be attenuated by a factor of 200-500 to avoid saturation of the Beetles [31]. The Beetle front end board ("FE board" in figure 3.6) is thus equipped with an attenuator circuit, containing a 20 Ω resistor and a 3.3 pF capacitance for each channel. The attenuator circuit and black coated Beetles as well as the FE support card which receives the voltage to power the Beetles and SiPMs can be seen in figure 3.12.

Each SciFi module is connected to 2 FE boards (one for the "straight" fibre side, the other one for the "tilted fibre" side), which contain 8 SiPMs and 8 Beetles respectively. Thus, 16 SiPMs and 16 Beetles with 128 channels each lead to 2048 channels that have to be read out per module.

Figure 3.12.: Photo of the FE board of one side of the SciFi detector module. On the left
are the connectors for the flex cables from the SiPMs, right of the connectors
are the attenuation circuits. The black spots cover the Beetle chips. The
green board (marked "R-S") in the centre receives the voltage to power the
Beetles and SiPMs. In addition, it receives and transmits control signals
and trigger/clock signals from and to the Beetles. The flat cables on the
right side are 7 m long data cables which send data from the Beetles to the
RPT boards.

The Beetle's a-link signals are transmitted via 7 m cables to repeater boards (RPT board). There is one RPT board per detector module, so 8 RPT boards in total. The RPT boards serve two purposes [30]: First, they amplify the data signal from the Beetles to drive it over 60 m to the TELL1 readout boards [32]. Second, the RPT boards also transmit control signals from the control PC and control boards to the SiPMs and Beetles. The detector control system software is described in section 3.4.

3.3.3. Adaption of the Repeater boards

The BGV uses many electronic components that were developed for the VELO detector. Similar to the VELO, BGV data has to be driven over 60 m cables by the RPT boards.
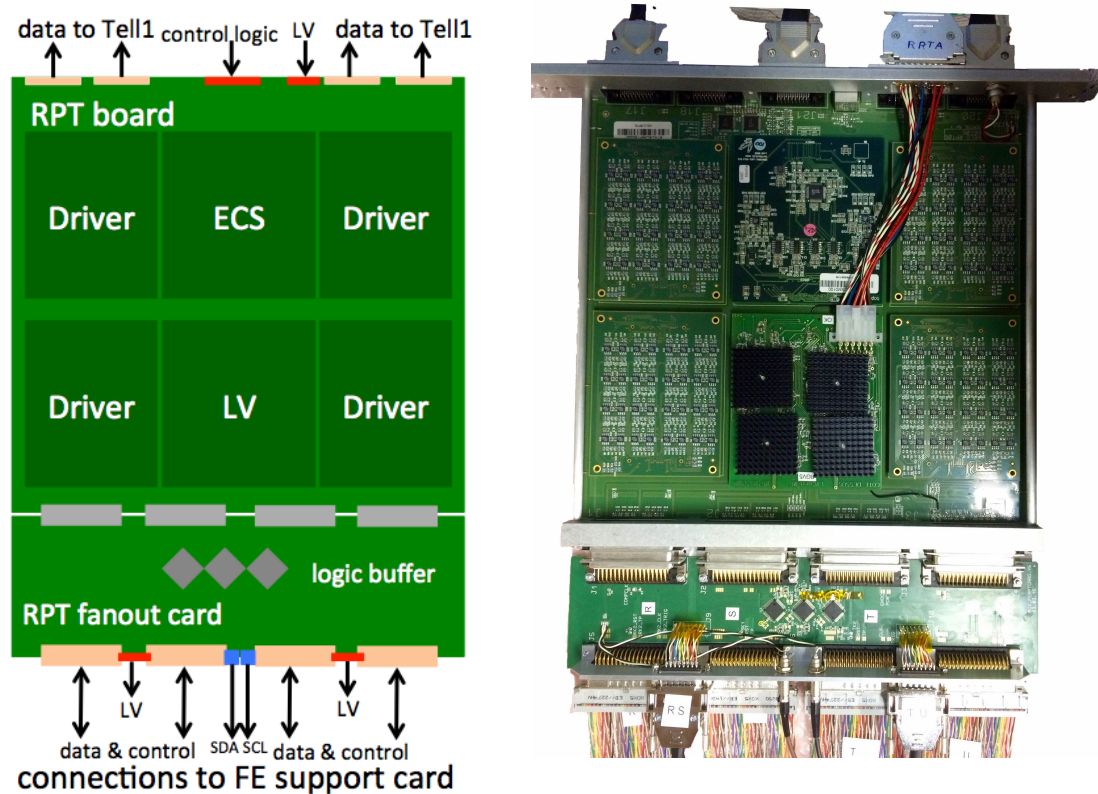
(a) Schematic drawing of the RPT board with the RPT fanout card connected in green. The FE support card and FE boards in the schematic are mounted on the SciFi module. Based on R. Frey [20].

(b) Photo of the RPT board with the RPT fanout card connected to it.

Figure 3.13.: Schematic drawing 3.13a and photo 3.13b of the BGV RPT board.

There are, however, two significant differences in the design of the BGV that call for adaptions of the RPT boards. VELO hybrid detectors are biased by a voltage line that goes through the RPT board. However, the BGV uses SiPMs that are directly biased from the voltage supply, so the voltage connections of the RPT board had to be disconnected.

VELO hybrids are also equipped with temperature sensors. While the BGV also has NTC temperature sensors mounted behind the SiPMs, their signals are not routed through the RPT board but are directly sent from the FE support card to and read out by an ELMB system (see ref. [33]).

Each RPT board is connected to a front end fanout card, which fans out the fast signals from the RPT board (like SCL, SDA) into four signals to match the 4 FE boards. A schematic and a photo of the RPT board and FE fanout card are shown in figure 3.13.

3.3.4. TELL1 readout boards

The analogue signals are transmitted over 60 m cables from the RPT board to the TELL1s. The TELL1s, as well as all other non radiation hard electronics, are located in the service tunnel that runs parallel to the LHC tunnel. A drawing of the location of the BGV in the LHC tunnel as well as the location of the racks in the service tunnel is shown in figure 3.14.
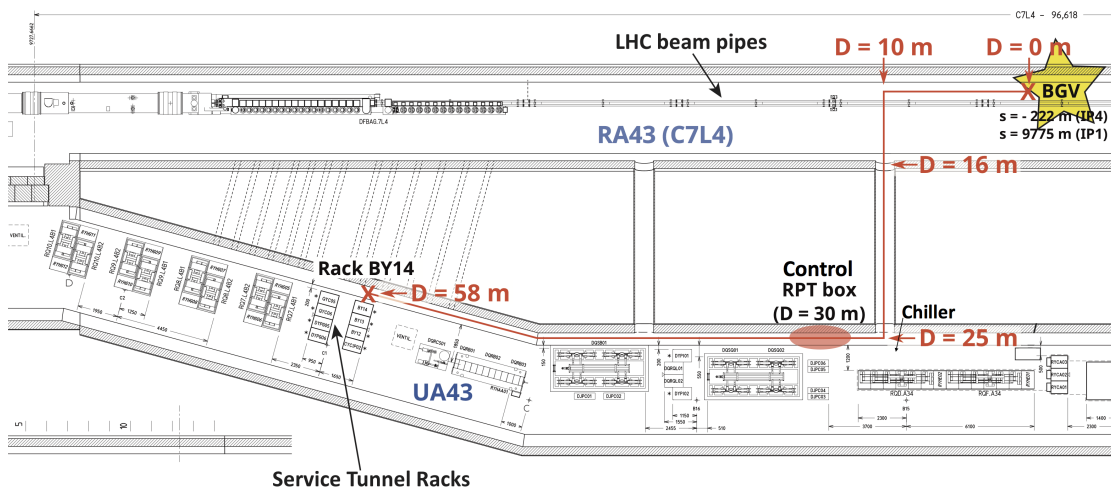

Figure 3.14.: Schematic of the LHC tunnel and service tunnel left of IP4. The BGV is situated approximately 60 m from the racks in the service tunnel which contain the non radiation-hard readout electronics. P. Hopchev [20].

There is one TELL1 per SciFi module (2048 channels) and each TELL1 serves as analogue-digital converter (ADC) and applies cuts and correction on the data. Each TELL1 is equipped with four analogue receiver cards (ARx) which perform the analogue-digital conversion. The data are then sent to a pre-processing FPGA (PP-FPGA), where corrections (e.g. for cross-talks), zero-suppression and clusterisation on the raw data are applied. An additional FPGA, the synchronisation and link FPGA, collects the PP-FPGA data, merges the packets into multi-event packets (MEP), and frames it to fit Ethernet and IP standards before being transferred to the computing farm via its Gbit card [32]. The different components of the TELL1 are shown in figure 3.15.

The TELL1s digitise the analogue data from the Beetle. The analogue zero is translated into a pedestal value of about 512 ADCs. Each a-link has its own pedestal value around 512 ADCs (e.g. between 510 and 518 ADCs). Values below the respective pedestal correspond to a negative signal, values above to a positive one.
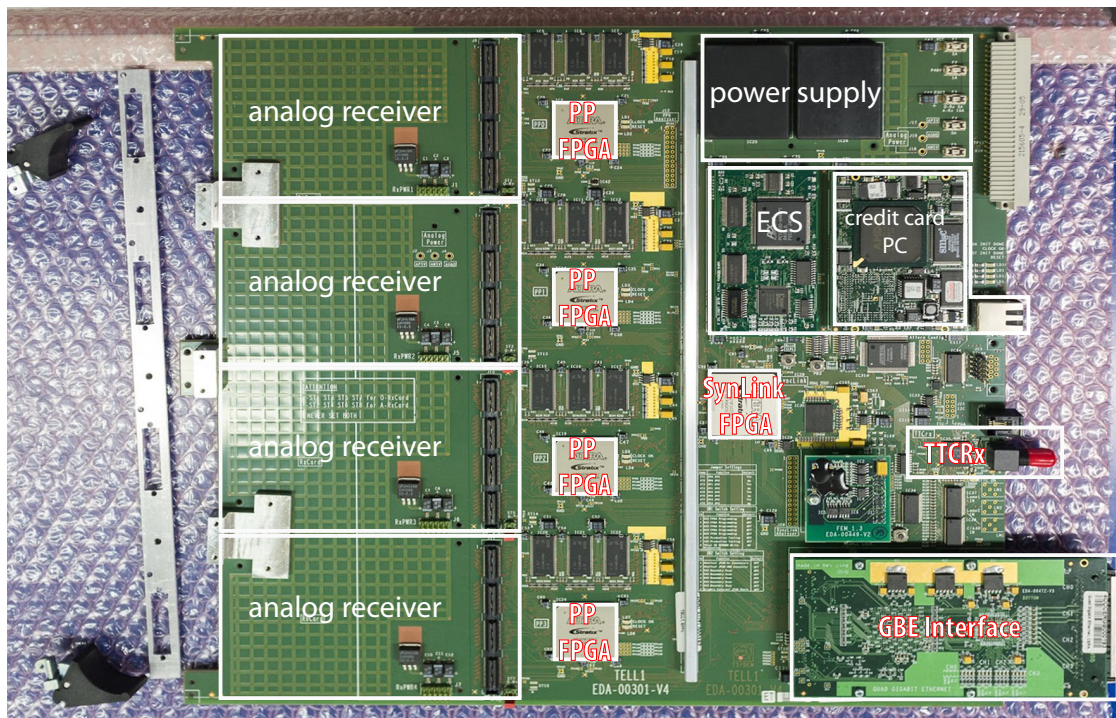

Figure 3.15.: Tell1 without the four ARx cards assembled (on the left). It contains 4 pre-processing FPGAs (one per ARx card), one synchronisation and link FPGA, and a gigabit interface card on the bottom right. The experiment control interface (ECS) is located on the right, controlled by the on-board credit card PC. The clock synchronisation signal is received via the optical link, called TTCRx.

The TELL1s also contain configurable delays to synchronise with the LHC-wide timing and trigger system, to compensate for different cable lengths between the readout components, and to ensure that all data get linked to the correct trigger. These delay settings are discussed in more detail in section 3.5.

3.3.5. BGV computing farm

Unlike the LHCb computing farm, which consists of a multitude of server racks, the BGV computing farm is made up of one blade server chassis, currently filled with four blade servers. The HPE 7000c blade enclosure uses 10 units in rack space and can be filled with up to 16 blade servers to process the data in real time. The blade servers purchased for the BGV project have 12 2.80 GHz processors and a disk space of 512 GB each ("HPE ProLiant WS460c Gen8 Graphics Server-Blade").
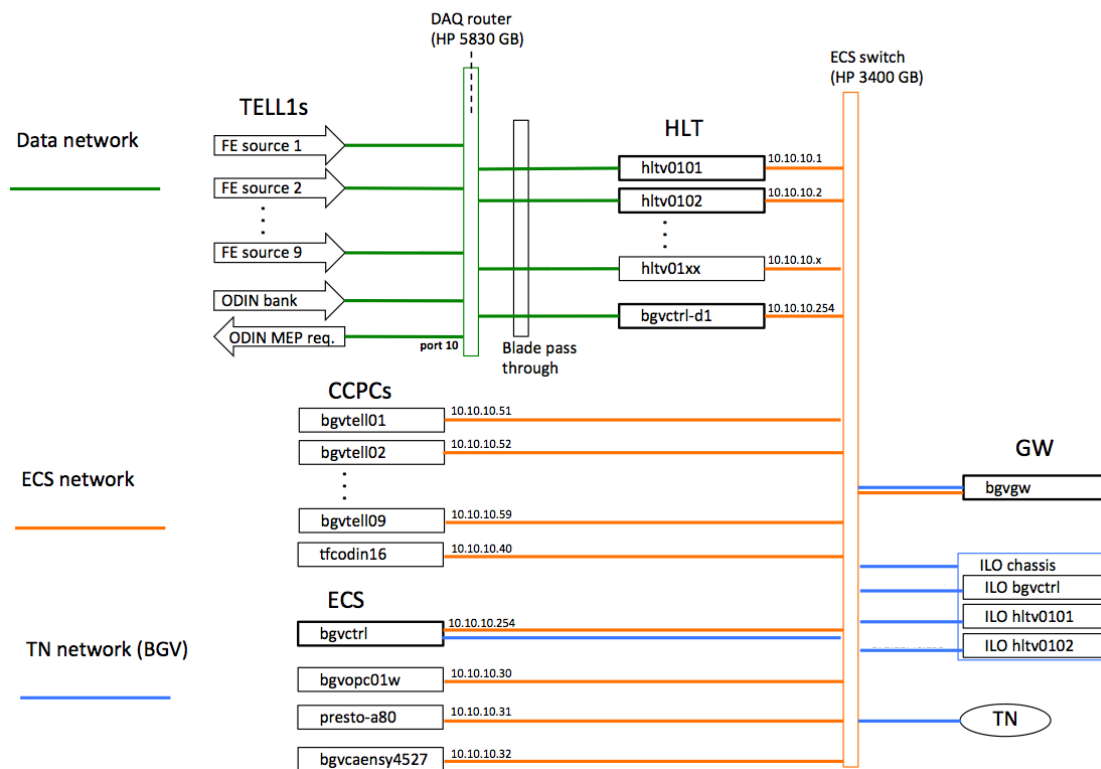
Figure 3.16.: BGV networks with the data network, including TELL1s, DAQ router and HLT nodes, the experiment control (ECS) network, including the credit card PCs of the TELL1s and ODIN as well as the technical network (TN), including the control machine, the voltage supplies and the chiller. C. Barschel [35].

Apart from the control machine, which uses one blade server, the other blades are only used for processing the detector data during acquisition and are referred to as "HLT computing farm". The processed final data of each DAQ process is stored in CERN's long-term storage system EOS [34].

To ensure a smooth data transmission and avoid potential bottlenecks, a gbit/s switch transmits the data output of the TELL1s directly to the HLT computing farm ("HP 5830AF-48G").

During commissioning of the BGV system, data are analysed off-line; after commissioning, the track and vertex reconstruction will be performed on the fly in the BGV CPU farm with the aim to produce a real-time image of the LHC beam and of individual bunches. Figure 3.16 gives an overview of the different networks of the BGV.

3.4. Detector Control System

3.4.1. Detector Control Hardware

The detector is controlled via several components that are situated in the service tunnel racks. First of all, one of the blade servers that were described earlier, is used as a control PC. This control machine runs on Linux and is the centre piece of the BGV control. It contains all the control software which is described in the next subsection. An additional PC is installed in the tunnel, which is used for communication with components that use the OPC protocol. This protocol is only reliably available on the Microsoft Windows operating system and thus needs a separate machine. A LHCb specific SPECS master card (Serial Protocol for the Experiment Control System, see ref. [36]) is installed on the main control machine, enabling communication with the BGV control (CTRL) board's SPECS slave.

The CTRL board receives the clock and trigger signal through an optical link (TTCrx) and distributes it through the RPT board to all 16 Beetles of a SciFi module. The control signals have to travel through two times 30 m long copper cables to reach the RPT boards, where they are further distributed. To avoid loss of the fast signals, a control signal repeater was designed and built to amplify those signals at 30 m. The CTRL board also controls the low voltage power supply of the Beetles. There are six output ports per CTRL board and each port controls all Beetles from one entire module. Two CTRL boards are used in total for the BGV with four modules connected to a board respectively.

The Beetles and the SiPMs are biased with voltage supply cards from CAEN. A CAEN SY4527 power supply crate is equipped with four A2518 low voltage boards to supply the voltage for the Beetles and one A1539 power supply board to bias the SiPMs. In order to reduce cost and the amount of cables and connectors, four SiPMs with similar break down voltages are grouped together and biased with one channel.

3.4.2. Detector Control Software

To control the whole detector system with its many different subcomponents and manage data acquisition, the experiment control software for LHCb was copied in large parts and modified to the BGV's specific attributes. The BGV is controlled with the WinCC OA SCADA (Supervisory Control and Data Acquisition) software (here referred to as WinCC). The control software uses WinCC as a base layer and was expanded with a CERN-wide framework (the joint controls project, JCOP) which integrates finite state machines (FSM) [37]. These FSMs are a well-defined set of commands, that make the

control system run smoothly by distributing the state of each sub component to the parent component. The WinCC system communicates with the different hardware components through dedicated drivers and can control all controllable components of the detector [38].
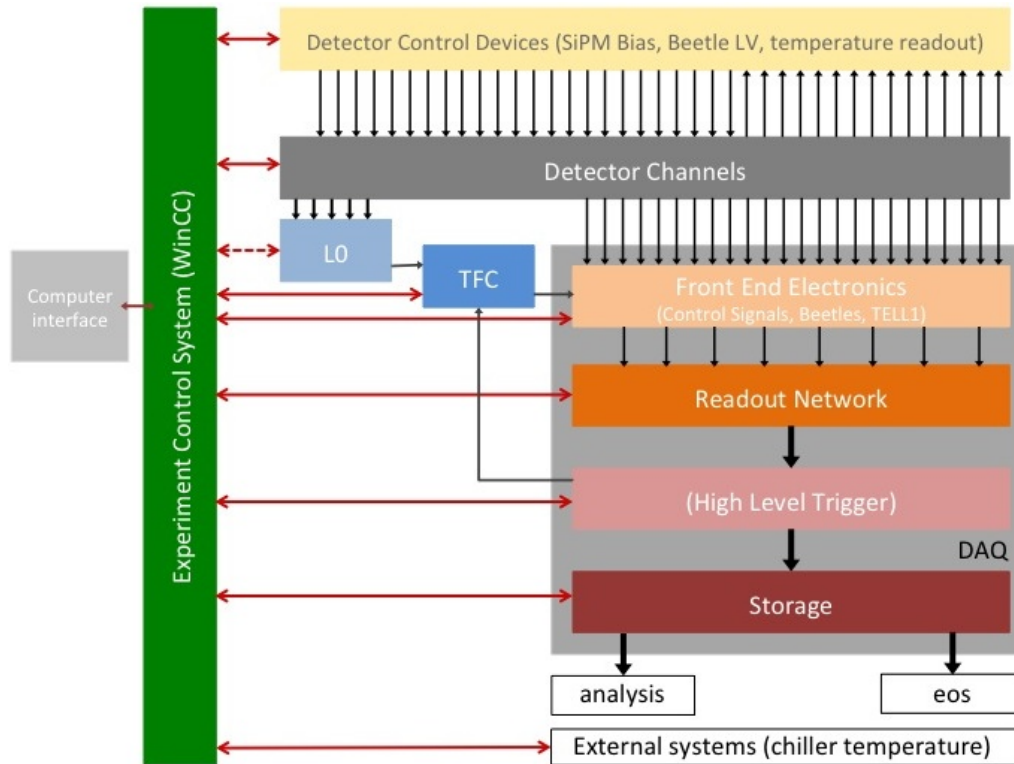

Figure 3.17.: Sketch of the communication between the experiment control system (ECS) on the left in green and the different detector (control) components. The signal propagation (also in terms of the FSM) is indicated by the arrows. The "Hight Level Trigger" (HLT) component is put in parentheses because it currently serves as data throughput and doesn't apply any trigger selections. Based on C. Gaspar [39].

These components include the power supplies, the Beetles, the cooling of the SiPMs, gas injection, temperature read out, timing parameters of the data acquisition, TELL1s, and the computing farm. In addition, it is possible to remote control the power supply of the 9U Wiener crates in the service tunnel that contain DAQ boards like TELL1s, Control boards and TFC. They can thus be turned off and on if needed (e.g. after a power outage). The control of the trigger scintillators (e.g. bias and threshold) is currently not included. The different hardware components are reflected as datapoints in WinCC. A schematic drawing of the communication between the experiment control system and the different data points is displayed in figure 3.17.
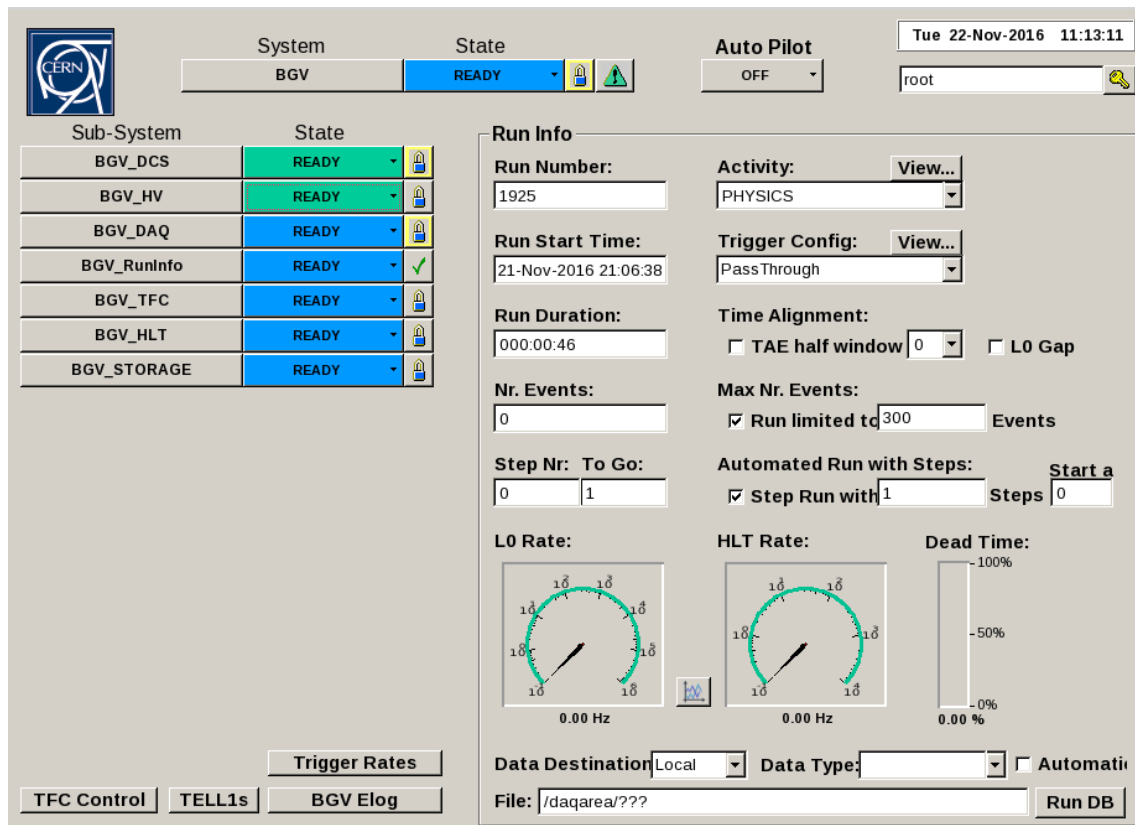
Figure 3.18.: Example of the current BGV top panel. It allows for taking data with clicking only one button after setting the parameters in the Run Info overview.

Figure 3.18 shows an example of the top control and DAQ panel of the BGV. As shown in figure 3.17, the BGV_DCS datapoint on the left side of the panel contains the low voltage supply for the Beetles as well as a panel for temperature readout. BGV_HV represents the control panel for the SiPM bias. The BGV_DAQ datapoint collects the control panels of the 8 TELL1s, the 2 CTRL boards each containing and 4 modules with 16 Beetles respectively. The TELL1s and Beetles are configured through these respective sub-panels. BGV_TFC represents the TFC ODIN board and controls the trigger distribution over the front-end components like the Beetles as well as the TELL1s and the HLT. BGV_HLT and BGV_Storage are the digital representation of the computing farm and the final data storage drive and currently contain 3 sub nodes each. The BGV_RunInfo control panel allows for different control settings for the data acquisition and storage as well as trigger configuration, while the Run Info overview on the right side of the top panel allows to change the activity (PHYSICS being the standard activity), the acquired event number, and the number of steps for commissioning runs.

3.5. DAQ timing and delays

3.5.1. Motivation for timing settings

The SiPM signal, which is read out by the Beetle, is about 100 ns long [40]. The signal has a high overshoot, which is nearly as high as the signal (as is shown in figure 3.27). Since the Beetle samples data once per 25 ns, it is important to precisely set the timing of the DAQ components. If the detector samples consecutive triggers and the timing is off by about 12.5 ns or more, the system might sample an adjacent bunch crossing, so it is important to set the correct "coarse delay" timing.

In addition, to ensure high quality of the data, it is also important to achieve a good signal-to-noise ratio. Sampling on the (correct) peak (or just before the peak to avoid a so-called spillover effect) of the pulse shape is necessary with a precision of a few nanoseconds. These nanosecond delays are set in the "fine delay" registers of the relevant hardware.

3.5.2. Hardware components for delay compensation

To compensate for the signal delays, different mechanisms are installed. The first component that is necessary to enable sampling at different time slots is the Beetle pipeline: As mentioned earlier, the Beetle buffers data for up to 4 μs or 160 bunch crossing events. The data are stored in an internal buffer regardless of an external trigger signal [19]. This means that the data arriving at a TELL1 were acquired up to 4 μs before the external trigger (L0 accept) arrived at the Beetle. The buffered data in the Beetles are only transmitted to the TELL1s after receiving a L0 accept signal from the TFC, otherwise they are discarded.

As described in the previous section, the difference between the clock in the TELL1 and the clock of the Beetle has to be accounted for by setting the appropriate delay values. The TFC, CTRL board and TELL1 each have a coarse delay register, which allows for setting delay step sizes of 25 ns. In addition, those boards have a fine delay register (the CTRL board has 6 such registers, one for each module that can be connected to one CTRL board), which allows for delay steps between 0.5 ns and about 1.5 ns. While the coarse delays give an information about which buffer row (or pipeline column number, PCN) of the Beetle to access (this corresponds to the bunch crossing), the fine delay defines where the FE signal is sampled, thus enabling the Beetle to sample at the optimal signal height.

The coarse delay for the TELL1s and the CTRL board can be combined and complement each other. This means that adding delay in the TELL1 register and removing it in the CTRL board register would result in a zero change of the overall delay. The CTRL coarse delay value thus only needs to be touched, if the value that needs to be written into the TELL1 register exceeds the register size (the coarse delay for the TELL1 can be up to 31 clock cycles).

For the BGV the TELL1s' coarse delay registers (also referred to as "cable delay") were mainly used, however, the coarse delay in the CTRL boards had to be manipulated too. The CTRL board coarse delay register is set with two-digit hex values ranging from 0x11 to 0xFF. The delay has to be increased in steps of 17 (e.g. 0x11, 0x22, 0x33, etc.) and each step corresponds to one clock cycle (or 25 ns). It is important to note that the coarse delay setting of the CTRL board concerns 4 BGV modules at once (up to 6 modules could be connected to one CTRL board), while the coarse delay for each TELL1 only concerns one detector module respectively.

The coarse delay (or L0 latency) of the TFC needs to be set when using the TFC in "external mode", so when the clock is received from the LHC wide clock system and not generated inside the TFC. The determination of this L0 latency is described in section 3.5.5.

3.5.3. Coarse delay determination

One of the goals during the pre-installation tests of the BGV was to find the correct sampling point through timing delay settings in the relevant hardware registers. To achieve a correct timing, the LHC clock signal is used as a reference. This clock is distributed by the readout supervisor (TFC) through optical links to the TELL1s and the CTRL boards. From the CTRL boards, the signal is distributed to the Beetles through copper cables. The trigger signal is also distributed by the TFC through the same channels.

The Beetles take data every 25 ns regardless of an external trigger and store the data into a buffer. There are 160 buffer slots in each Beetle. It is determined which of the Beetle's buffer is read by the TELL1 when it receives a trigger signal from the TFC by setting the coarse and fine delay values in the TELL1. The correct delay values are derived by comparing the difference between when the TELL1 and the Beetle receive each LHC clock signal. While the TELL1 receives the clock signal quasi immediately from the TFC, the Beetle receives the same signal with a certain delay due to conversion in the CTRL board and distribution through copper cables.

The coarse delay between the clock signal arriving at the TELL, and the clock signal arriving at the Beetles can be determined by estimating signal propagation time between
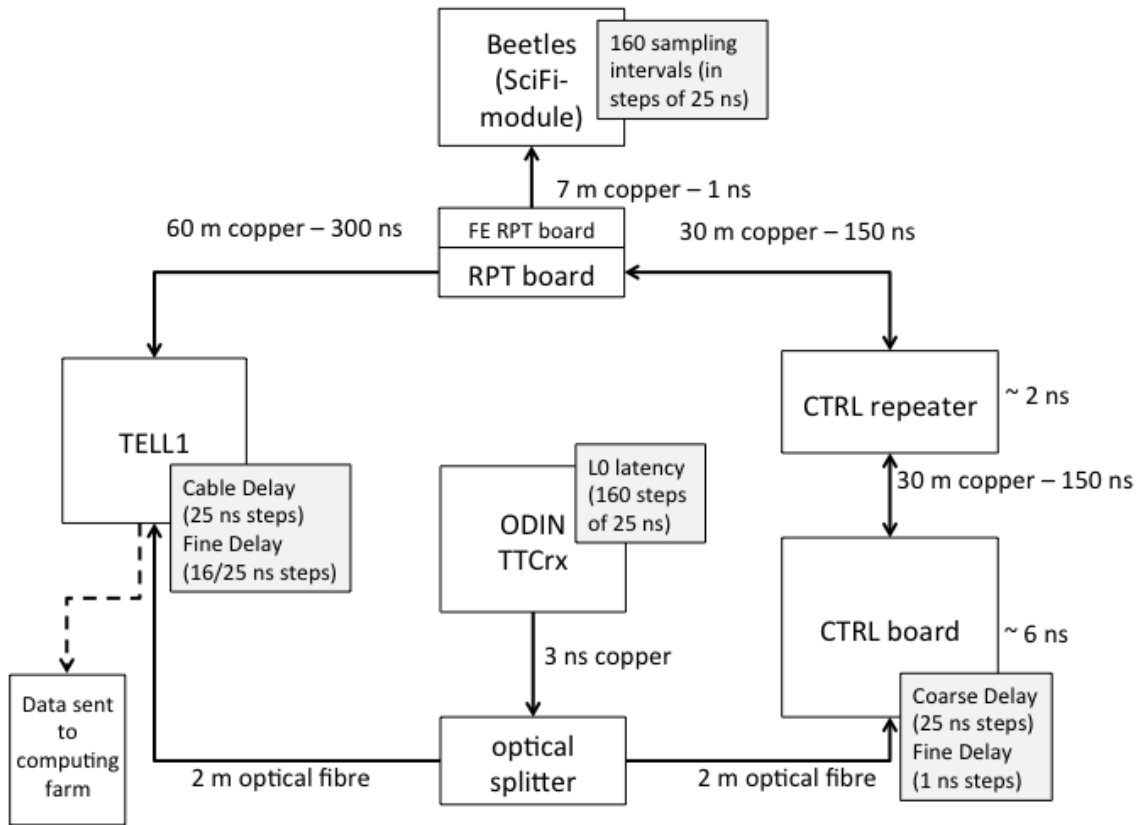
Figure 3.19.: Sketch of the different delays in the BGV readout.

the CTRL board and the Beetle. As mentioned above, the CTRL board receives clock and trigger signal from an optical fibre through an optical transceiver at the same time as the TELL1. The Beetle, however, receives the timing signals through copper cables, after they passed through the CTRL board, the CTRL repeater board, and the repeater board. The propagation of these timing signals takes several clock cycles in these boards. The travel time of the signals through the copper cables is determined by their length. The control cables between CTRL board and Beetles are about 60 m long and the estimated propagation speed of the signal in copper cables is about 70% c, which results in an estimated (cable) coarse delay of 300 ns or 12 clock cycles.

Since the precise coarse delay values for the different boards were not known, the coarse delay values from the VELO were taken as an indicator. This indicated value had to be increased by a few clock cycles due to the fact that the BGV's control cables are about twice as long as the VELO's and that they are connected through the CTRL repeater board. The approximate signal delays per cable and DAQ component are displayed in figure 3.19.

3.5.4. Test pulses - Internal delays

As mentioned above, the coarse and fine delay settings between TELL1 and Beetles (CTRL board) have to be investigated properly to sample (and thus digitise) on the correct bunch crossing and on the ideal signal height of the Beetle pulse.
Again, the coarse delay is estimated by taking the cable length and translating it into the time that a signal takes to travel through the cable. Then, test pulses (TP) are used to find the correct fine delays to sample on a good Beetle signal height. The correct cable and fine delay values between Beetles and TELL1 can be found before connecting the system to the (external) LHC clock. These delay values are relevant for the speed of signal transmission between the TELL1 and the Beetles only. The procedure was performed first with the internal clock of the TFC before installation of the detectors in the LHC tunnel.
Test pulses (TPs), which are used to derive the fine delays in the digitisation of the analog Beetle data in the TELL1s, are a feature of the Beetles. When TPs are enabled, two specific channels per a-link (one a-link contains 32 channels, as specified in section 3.3) are triggered to send a signal with a certain pulse height which alternates in polarity (to avoid saturation). Hence, the delay times for the optimal fine delay sampling only corresponds to the raw Beetle signal but not to the convoluted signal of the Beetle and the SiPM.
To find the ideal delay values with TPs, several steps are followed: First, a run with e.g. 1000 events is taken with TPs enabled. The data containing TPs are plotted against the channel number. The plotted data can have different properties. For example, if the data are good, the TPs show up in the expected channels and all 2048 channels are filled with data. This case is the ideal case and represents the goal and result of correctly applying all delays.

However, a more likely outcome is that the timing is shifted, resulting in header bits showing up in the first channels, TPs showing up in different channels than expected or in two neighbouring channels. The shift can also result in missing data in the last of the 32 channels in each a-link. Missing data on either end of the whole channel spectrum are caused by wrong coarse delay (or cable delay) settings and have to be corrected for in the register of the respective TELL1 in which the missing data occur. Examples of data with improper settings (or issues with the TELL1) are shown in figures 3.20a and 3.20b.
Other examples are given in figure 3.21. The top histogram, figure 3.21a, shows missing data in several channels around channel number 1300 and headers showing up in channels where there should be no headers. The bottom histogram, fig. 3.21b shows a pedestal run with good quality data where TPs were enabled and are inducing an alternating signal in channel 4 and 23 for each of the 64 a-links.
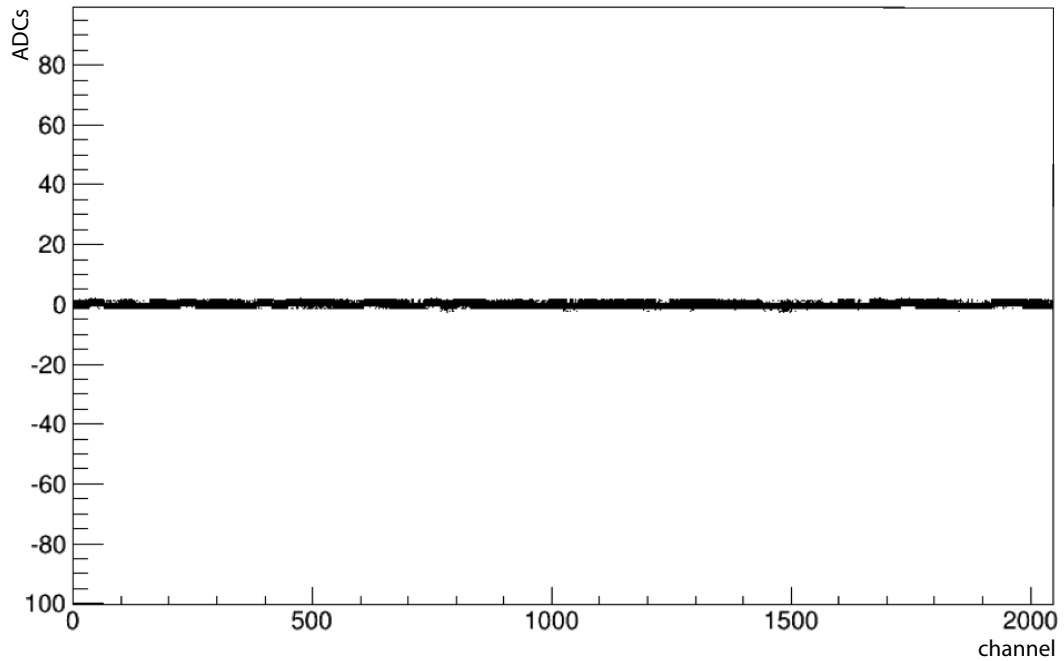
(a) Example of a DAQ run resulting in pedestals only. Since there are no fluctuations around the pedestal subtracted values, the conclusion is that either the power supply of the TELL1 was interrupted during that run (e.g. a broken fuse) or that no front end components were connected.
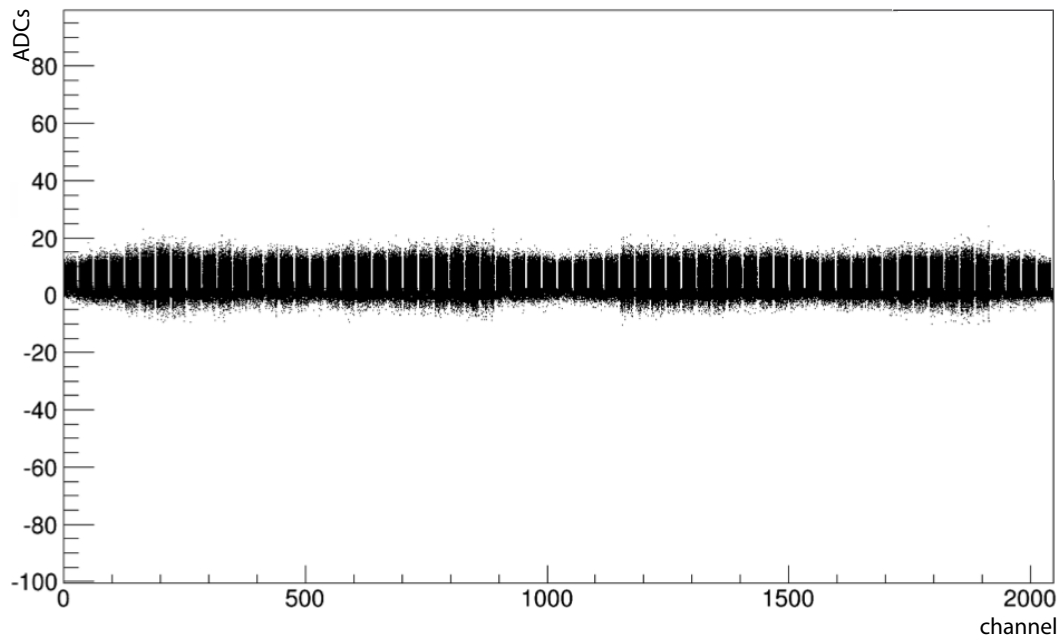
(b) Example of a DAQ run with bad fine delay setting. Here, the last channels of each of the 64 links are missing due to a bad setting in the fine (or "phase") delay.
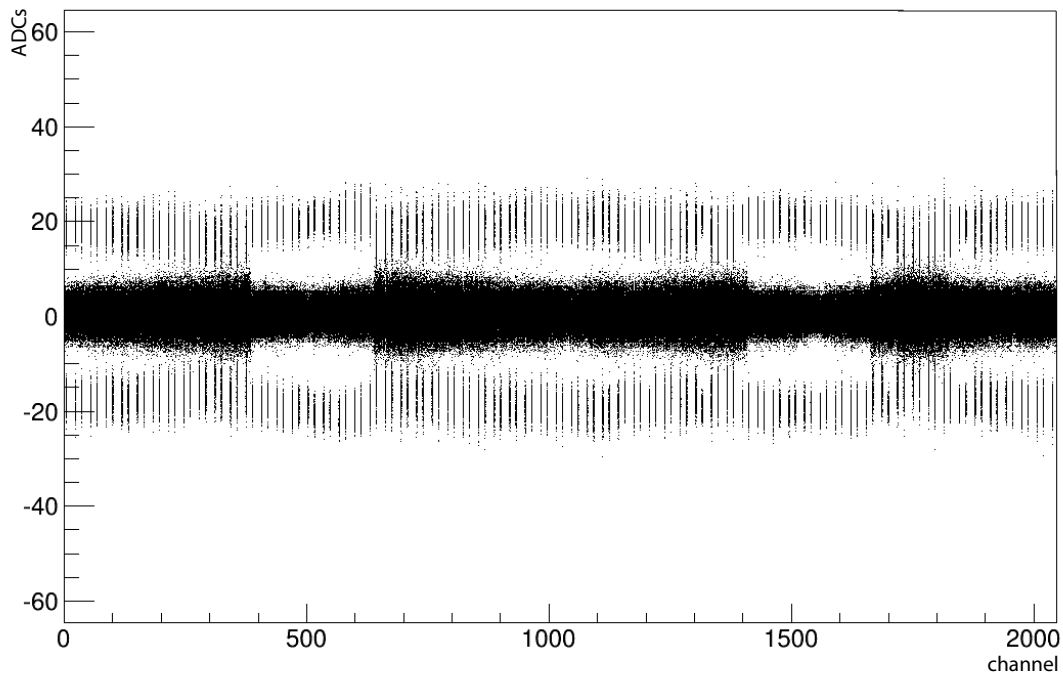
Figure 3.20.: Examples of issues with the DAQ setup and timing.
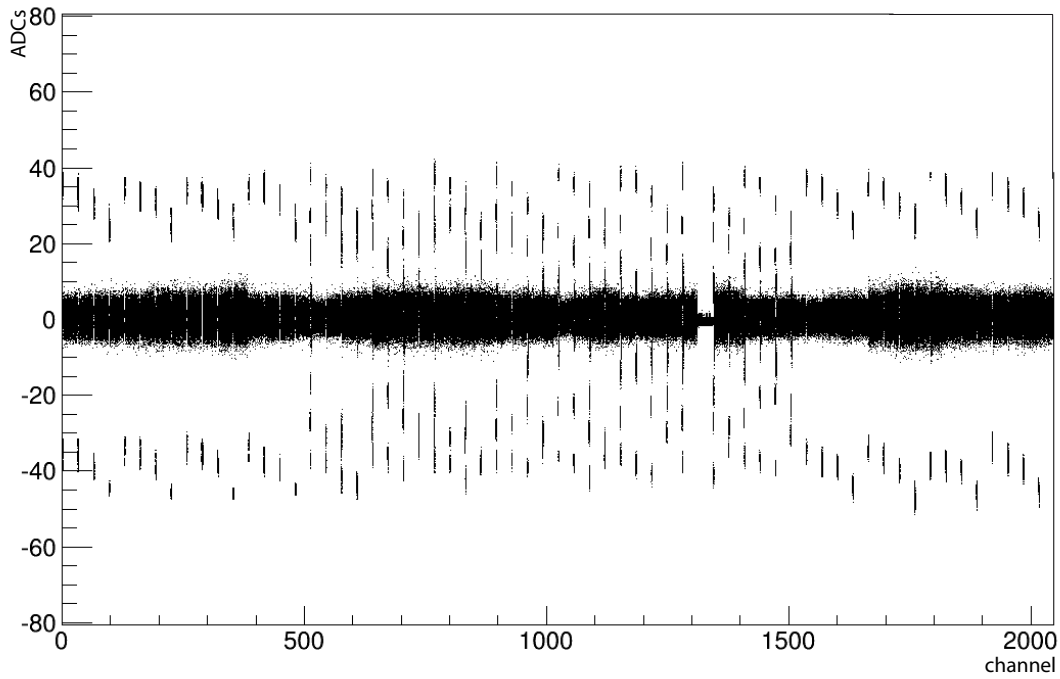
(a) Histogram of pedestal subtracted data. Headers are visible due to bad timing, some data are missing due to a bad cable connection.

(b) Histogram of pedestal subtracted data. Pedestals and test pulses are well visible, headers are not shifted into the data sample.

Figure 3.21.: Examples of two pedestal subtracted histograms with different timing settings.

SamplingPhaseScanEven for Link 17
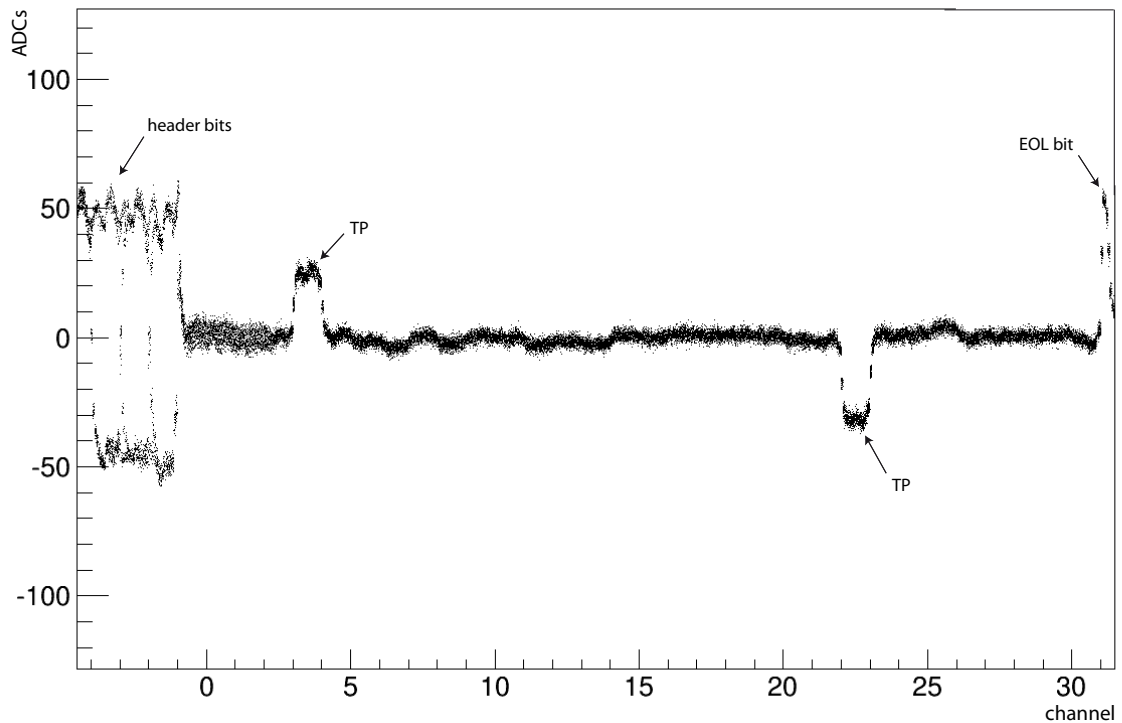
Figure 3.22.: Example of TELL1 data plotted against channel number. On the left, the large signals are the four header-bits, around channel 4 there is the first TP and around channel 23 the second TP. The signal after channel 31 corresponds to the end-of-line signal.

Once the data look complete (e.g. ADC values plotted against the channels with no channel missing any value), a so-called "ADC Delay Scan" can be performed. Hereby, the TELL1's fine delay register is changed from a delay of 0 ns to a delay of 25 ns in incremental steps of about 1.56 ns (25 ns divided by 16 steps). To perform this scan, a specific activity in the BGV's top panel is chosen which takes 100 events per fine delay step with TPs enabled. The data are then analysed with a script provided by the VELO (commissioning) group [41] to find the optimal fine delay per link. Figure 3.22 shows one of the plots produced by the analysis script, where data are plotted against the channel number for one a-link. In total, 128 plots per TELL1 are created (two for each a-link, showing the alternating TPs). The headers can be seen in the first 4 channels preceding channel 0, the TPs occur in channels 4 and 23 respectively. An "end-of-line" signal after channel 31 completes the data "package" for this link.

The optimal delay values are derived with a macro and can be retrieved from a text file and saved into the respective TELL1 configuration file. Figures 3.23 and 3.24 are

Figure 3.23.: Example of the resulting delay values of the TELL1 delay scan. The values are saved in a text file and are transferred into the corresponding TELL1 configuration file.

Figure 3.24.: Example of the result of the TELL1 delay scan. The values are saved into the corresponding TELL1 configuration file to achieve an optimal digitisation delay.

examples of such delay values for one TELL1. There are 64 links per TELL1 and thus 64 fine delay registers to be set in each of the and 8 TELL1s. The procedure is described in detail in ref. [41].

The tables for the delay values are given in appendix A.1.

Another application of TPs is quality control of the TELL1 boards. While specific ARx card tests were performed, the amplitude of the signal per link can be a good indicator of

problems with a specific link. In addition, lower signal heights in TPs indicate problems with the power supply of the Beetles or the TELL1 and the need of fuse replacement. Figure 3.25 shows such problems with the power supply of the Beetles. While the TPs in figure 3.22 show a signal height of around 30 ADC counts, the TPs of figure 3.25 show only about 10 ADCs.
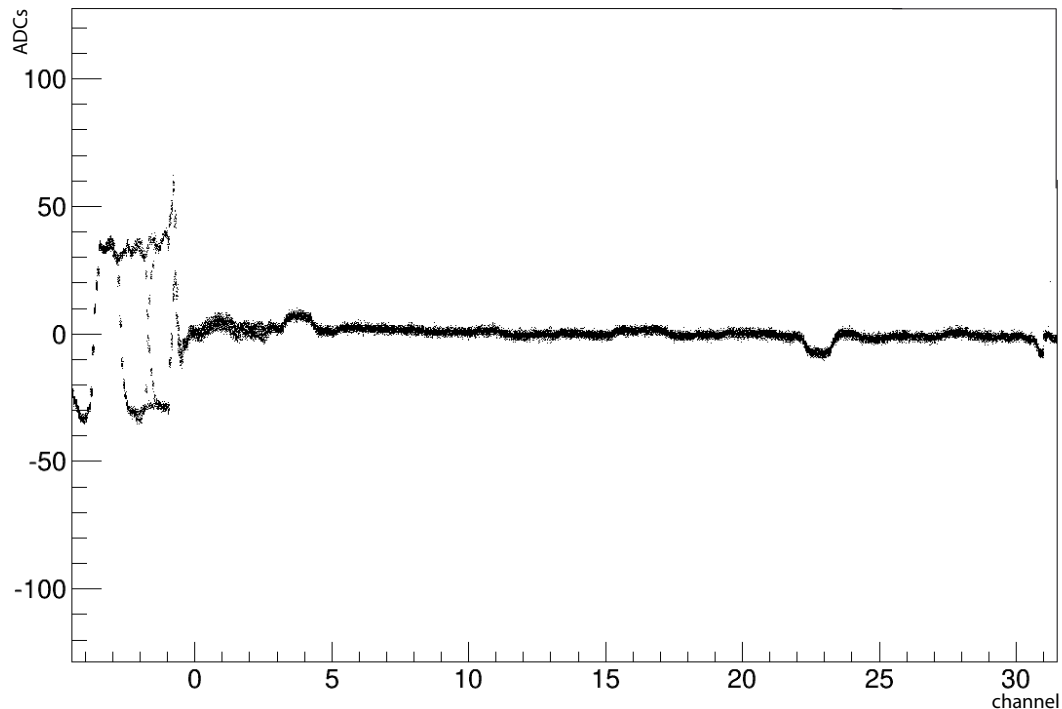
Figure 3.25.: Example of a link with small TP signals due to a low current in the Beetles.

3.5.5. Trigger propagation - L0 latency determination

After the installation of the detector in the LHC tunnel, the TFC was connected to the "external" LHC-wide clock and to the scintillator trigger. To compensate for the delay between the arrival of the scintillator trigger signal and the data acquisition of the detector, the TFC can implement delays similar to the TELL1 or the CTRL board. The delays are written into the "L0 latency" register, which can take values between 0 and 160, corresponding to the 160 buffers of the Beetles. Again, one step corresponds to one bunch crossing (25 ns).

To find the optimal L0 latency and thus trigger on the correct bunch crossing, the TFC was configured to take up to eight consecutive events per scintillator trigger command.

The pulse height (represented in ADC counts) was then plotted against the consecutive time slots of 25 ns. The data taken are non zero-suppressed and no corrections are performed on the TELL1. The expected signal has a negative polarity at first and a positive overshoot after the signal. The optimal bunch crossing delay thus has to be the one where the pulse shape is at its minimum.
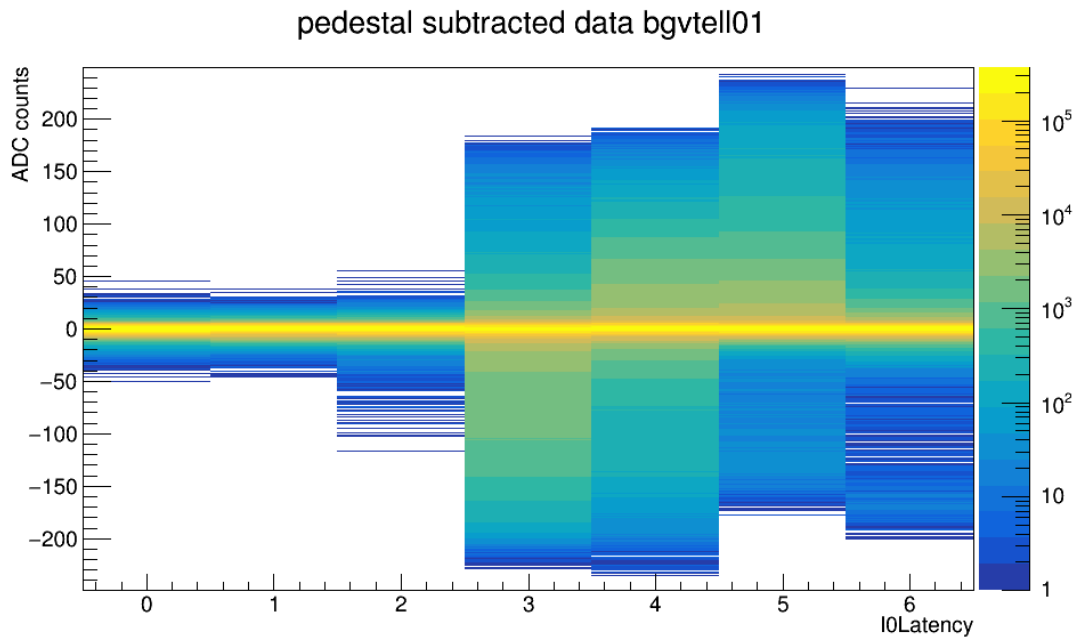
Figure 3.26.: Pulse heights at different TFC L0 latencies. The L0 latencies are displayed on the x-axis with 0 equalling 111 clock cycles, increasing by one clock cycle at a time and the y-axis displaying the pedestal subtracted ADC counts.

The plot from one of these L0 latency runs is shown in figure 3.26. Slot 0 equals a L0 latency of 111 clock cycles and the optimal latency is 114, which equals slot 3. While it can be argued that the ADC counts of slot 4 are even bigger than for slot 3, the intensity of the pulse is higher in slot 3. Slot 3 has many highly negative ADC values, which represent the expected negative pulse shape of the SiPMs. Slot 4 has a higher intensity of ADC values in the positive range, which represents the overshoot of the signal. The signal intensity is indicated by the colours, as shown by the legend to the right of the plot.

3.5.6. Optimal sampling of SiPM-Beetle pulse

Finally, the sampling of the front-end SiPM-Beetle pulse has to be calibrated to allow for data acquisition at an optimal signal height. While the TELL1 fine delay scan optimises the sampling point of the Beetle's TP and thus the digitisation timing, the pulse shape

scan optimises the clock delay settings for the front-end of the detector and thus the sampling time of the actual pulse shape. It is set in the respective delay25 chip registers in the CTRL board.
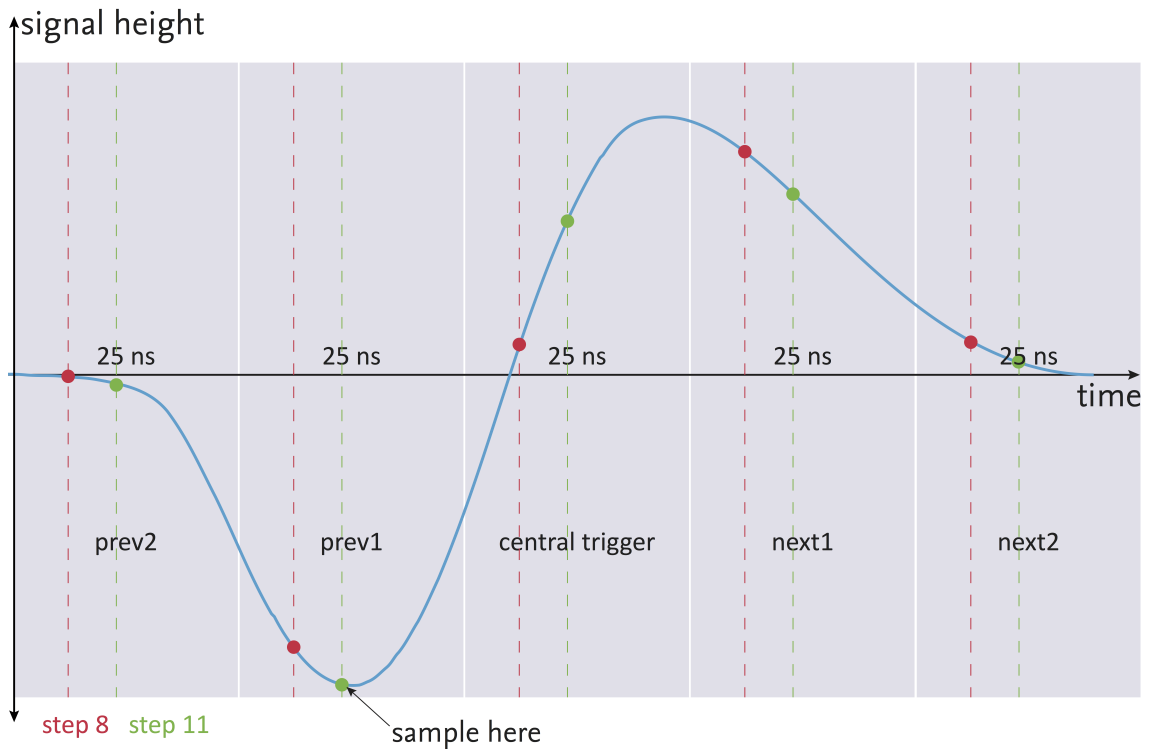
Figure 3.27.: Example of a BGV pulse shape. The pulse has a negative polarity and a large overshoot before attenuating back to zero. The grey blocks represent the consecutive 25 ns slots. The red and green dashed lines represent 2 of the 25 steps within the 25 ns blocks, in which data were taken. The set of complete data with all steps in the five consecutive blocks results in the pulse shape.

To perform the pulse shape scan, data are again taken with consecutive triggers; similar to the L0 latency scan. The consecutive trigger mode for this data acquisition is called time alignment events (TAE). Hereby, each trigger signal received from the scintillator trigger causes the TFC to send 5 consecutive L0 triggers to the detector; to sample 2 events before, one at, and 2 events after the trigger command. In addition, the fine delay is also shifted every 1000 events in 25 steps of 1 ns each. Thus the acquired signal is 125 ns long and the signal height can be plotted against the time. Figure 3.27 shows the different consecutive trigger blocks in purple and two of the 25 steps in red and green dashed lines.

To analyse and plot a pulse shape from the data, the events have to be sorted properly.
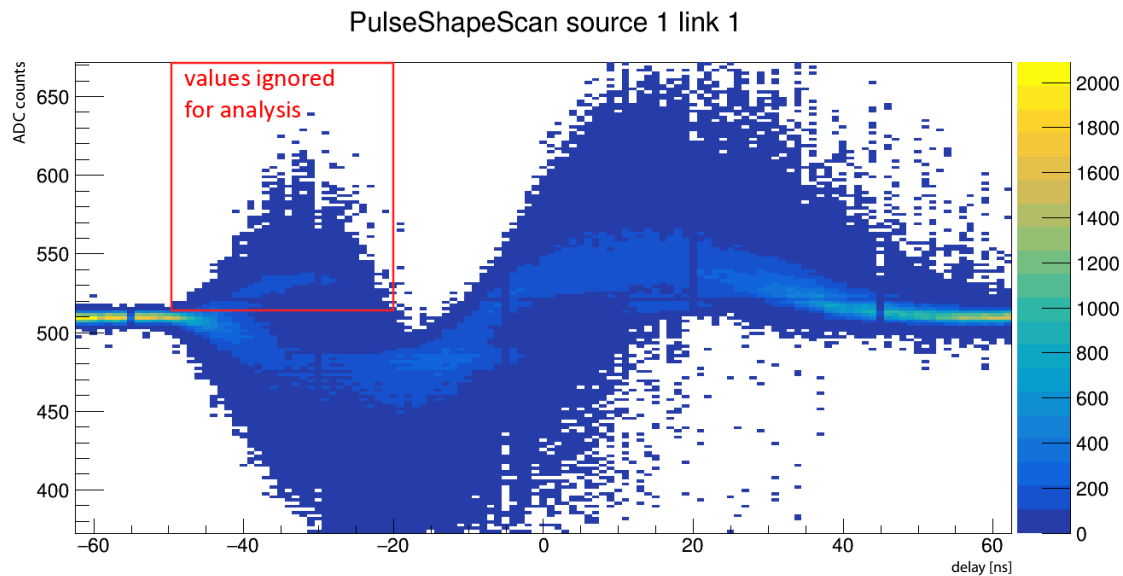
Figure 3.28.: Example of a pulse shape resulting from data taken with consecutive triggers. The signal inside the red box is assumed to be cross talk, caused by the attenuator circuits. In order to keep a good pulse shape for the average of each link and consecutively for each module, this area is excluded in further analysis.

The raw (non zero-suppressed, no corrections applied) data are taken step by step, with the five consecutive trigger blocks. The order of the events has to be sorted to find the correct time information and split the different delay times (steps) into the correct trigger blocks. In addition, a small amount of data was discarded for each link, see figure 3.28. The data inside the red box are assumed to be cross talk, caused by the attenuator circuits [31]. While the excluded data would not have an impact on the minimum of the pulse shape and thus the optimal fine delay setting, they would have an impact on the shape of the pulse.

The average signal height per delay is calculated from a histogram like in figure 3.28. The pulse shapes of the 64 links per module were collected in one histogram (e.g. figure 3.29). To find the actual fine delay value per module, an average of the signal height for the 64 links was calculated and is presented in figures 3.30 to 3.44. A fit around the minimum was added to the average pulse shapes, using a simple second degree polynomial function. The front-end delay value per module is derived by relating the minimum of the pulse shape to the step number it was acquired with. Since the pulse shape was taken with steps of 1 ns, the step number directly relates to the delay in nanoseconds, and can be written into the respective registers (clock delay) in the control board. The assumed ideal L0 delay for this scan was 115, which explains why the pulse minimum is not in the central 25 ns slot but in the one before (prev1) that.

While it is in principle possible to calculate the optimal delay value per SiPM/Beetle, it doesn't provide any useful information, since the DAQ system allows for only one fine delay value per detector module. This means that all 16 Beetles of a module will use the same value, so only the average pulse shapes per SciFi module/TELL1 are relevant. The delay value (which corresponds to a certain step number during the pulse shape scan) for the minimum of the pulse shape is used to evaluate the optimal fine delay value.

The delay value for each module and the corresponding step number, is given in table 3.1 for the average minimum of the pulse shape and for the minimum of the fit.

	module	Tell1	minimum [ns]	step number	fit minimum [ns]	step number
upstream	Top QRL 10-4L	bgvtell09	-27.5	10	-26.83	10.67
	Bottom Path 08-4L	bgvtell06	-30.5	7	-28.54	8.96
	Bottom QRL 07-4L	bgvtell05	-27.5	10	-26.46	11.04
	Top Path 09-4L	bgvtell04	-30.5	7	-28.51	8.99
downstream	Top QRL 01-5L	bgvtell01	-27.5	10	-25.73	11.7
	Bottom Path 02-5L	bgvtell07	-23.5	14	-24.81	12.69
	Bottom QRL 03-5L	bgvtell08	-27.5	10	-25.59	11.91
	Top Path 05-5L	bgvtell02	-27.5	10	-25.66	11.84

Table 3.1.: Front end delays derived from the pulse shape scan. The step number equals the clock delay in ns, that has to be set in the delay25 chip of each control board.

While the fit values are a better match to find the actual minimum of the pulse shape, and clock delay can be set with a precision of 0.5 ns, it is recommended to sample the signal just before the minimum, where it is more stable. This means that the values from the pulse shape average can be used. One exception should be considered for module Bottom Path 02-5L (bgvtell07), where the smaller delay of fit minimum seems to be a better match.

The Delay25 chip has 3 additional registers. To ensure good data quality, the registers L0A and L0FE need to have delay values that are 5 ns greater than the clock delay value.
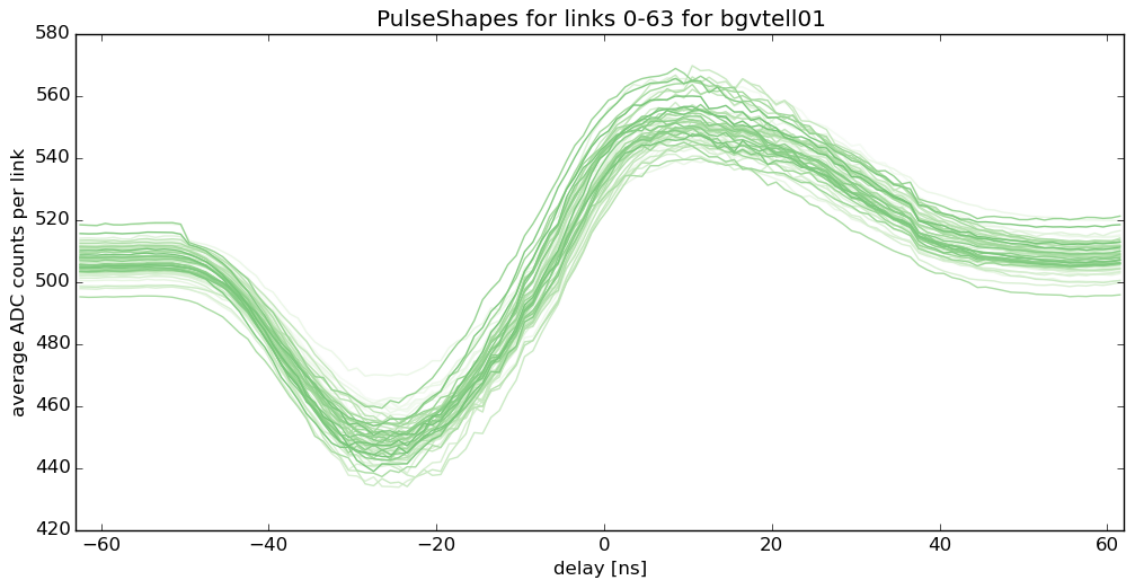
Figure 3.29.: Result of the PulseShapeScan analysis for all 64 links of bgvtell01, downstream module Top-QRL (5L).
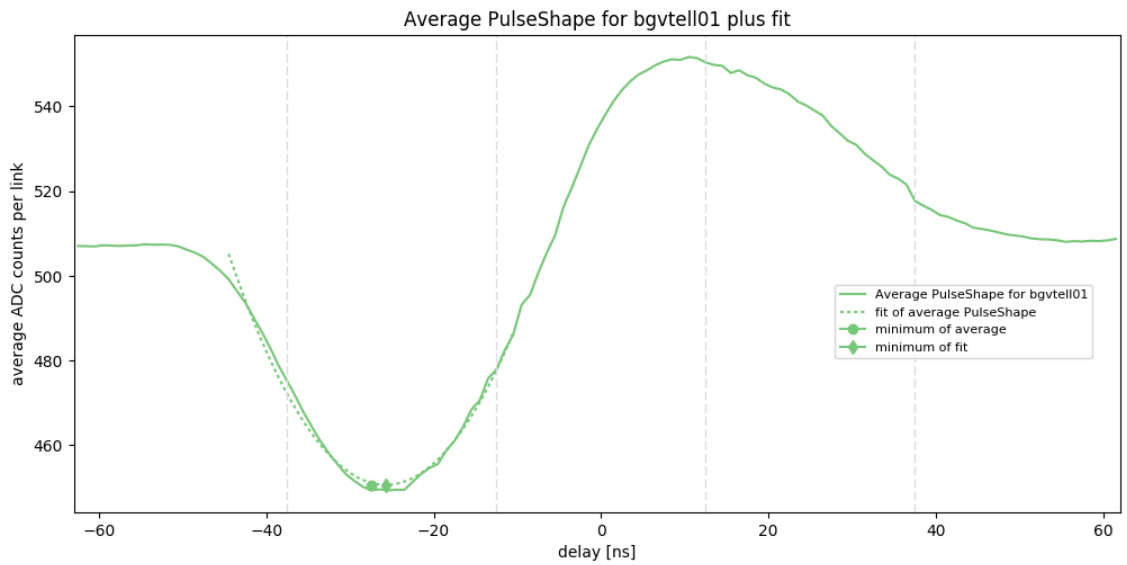
Figure 3.30.: Result of the PulseShapeScan analysis shown as average of all links of bgvtell01, downstream module Top-QRL (5L).
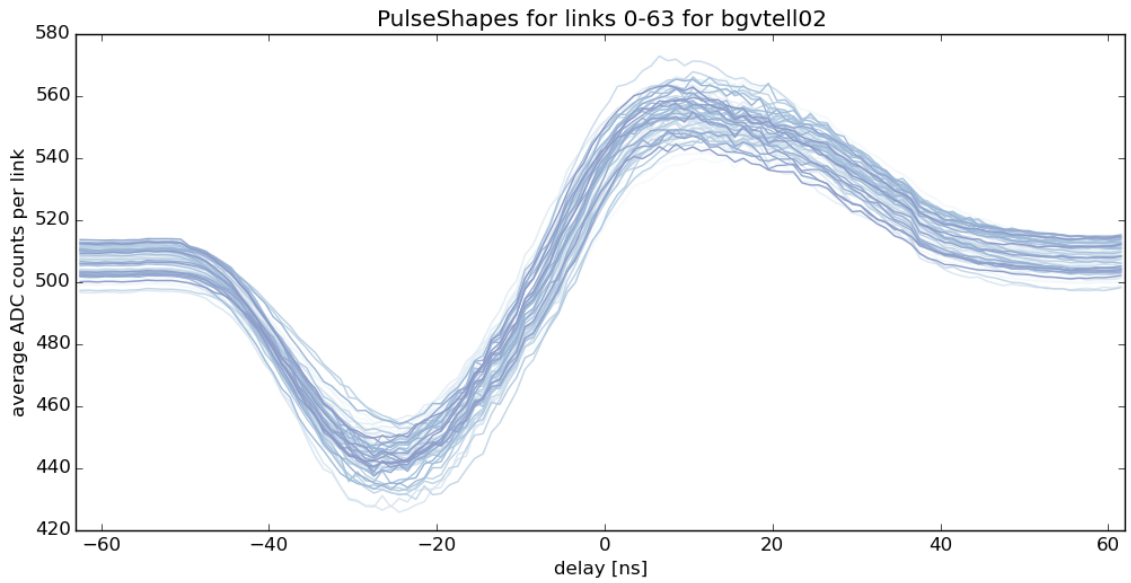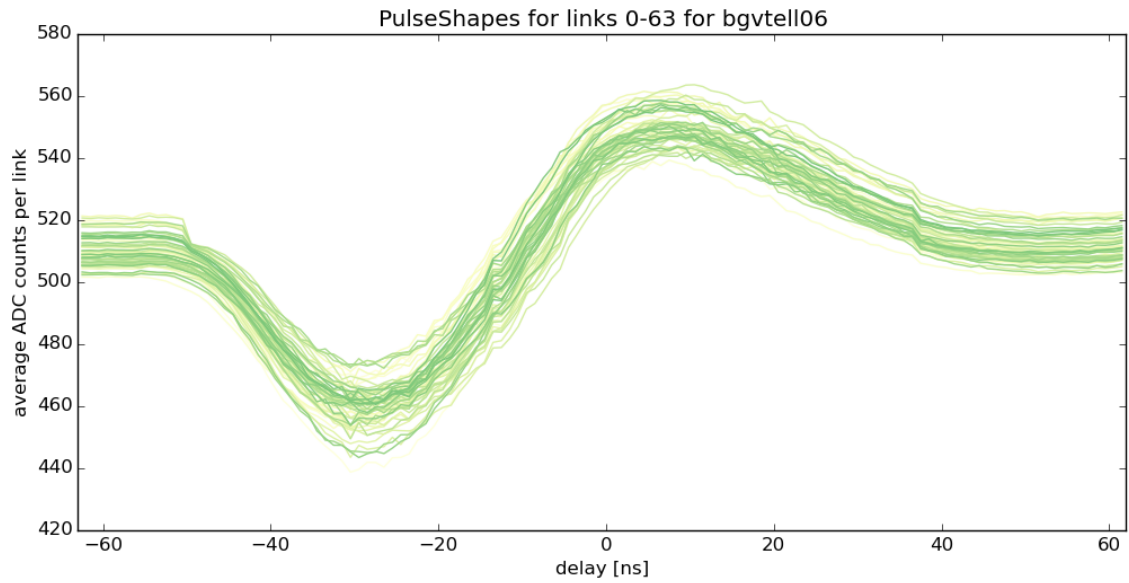
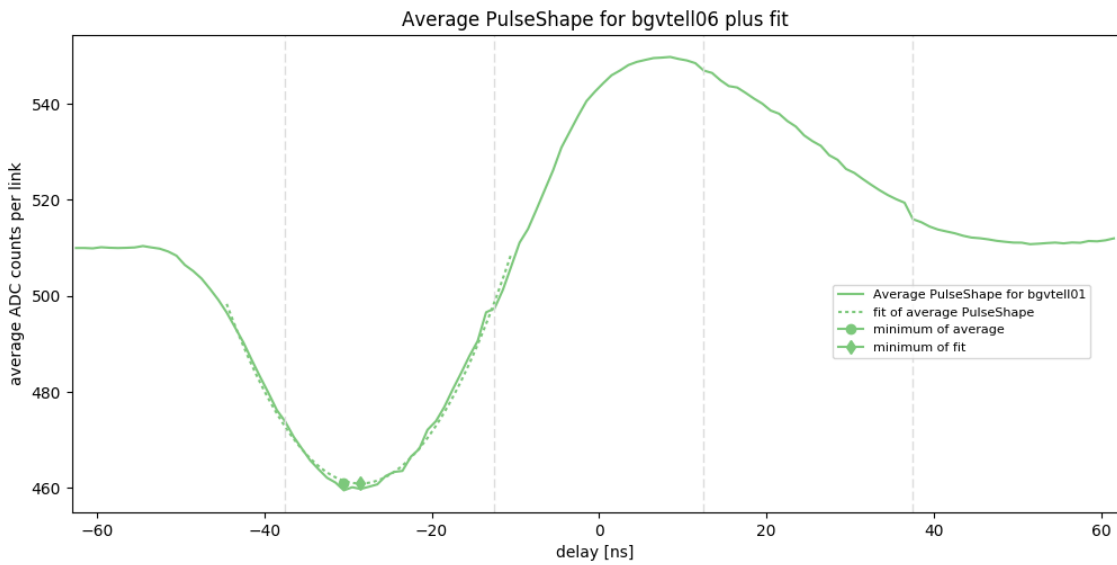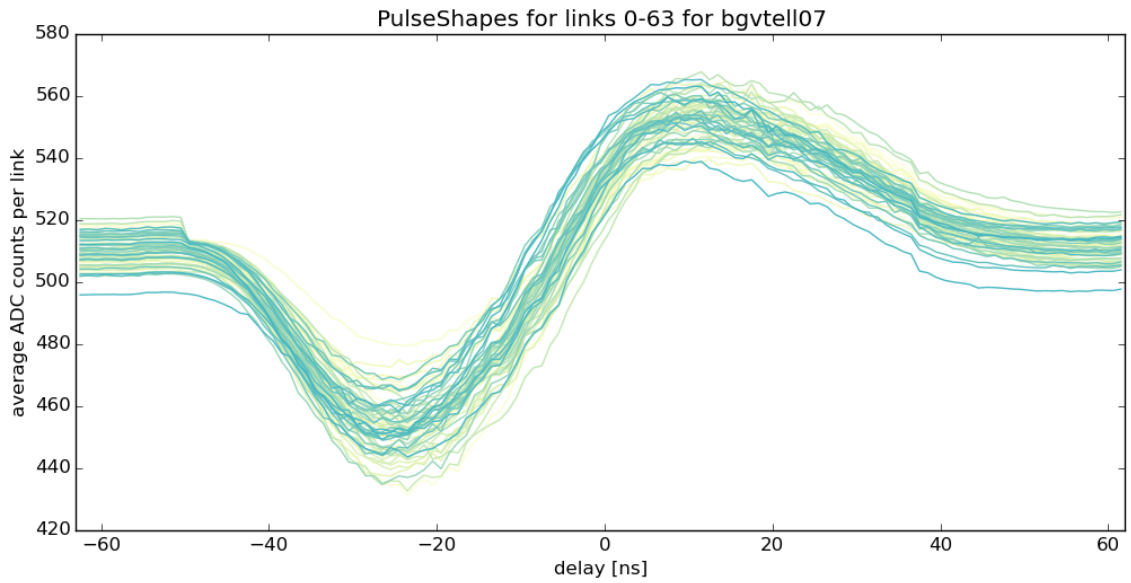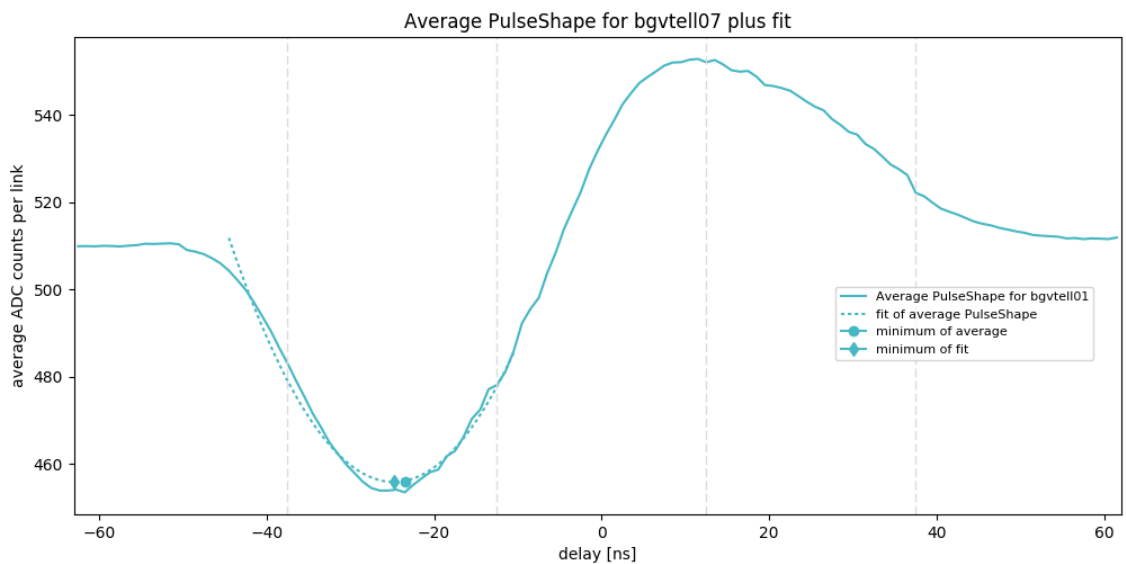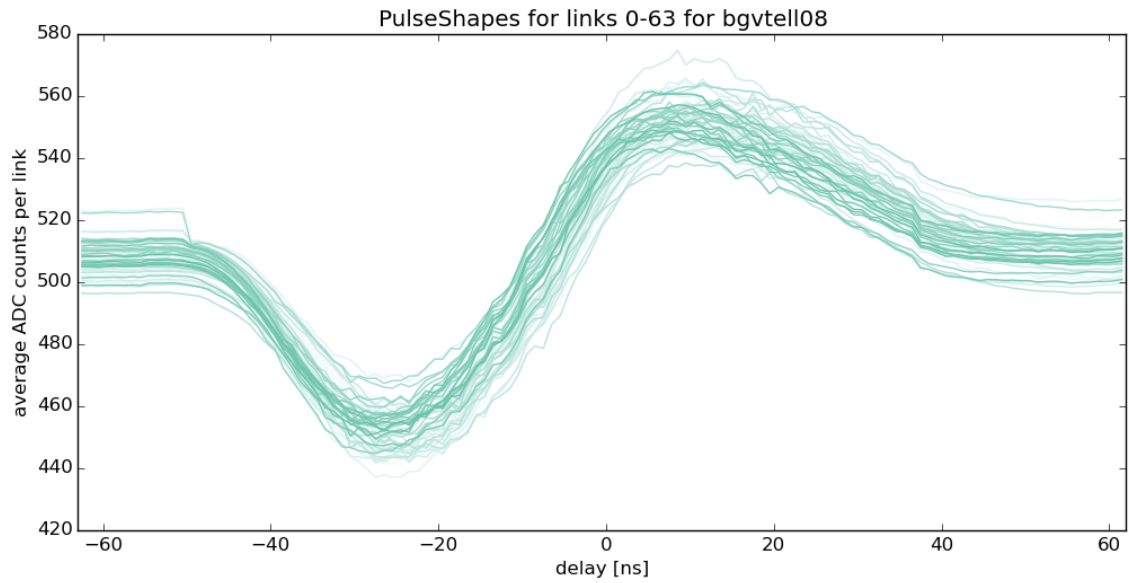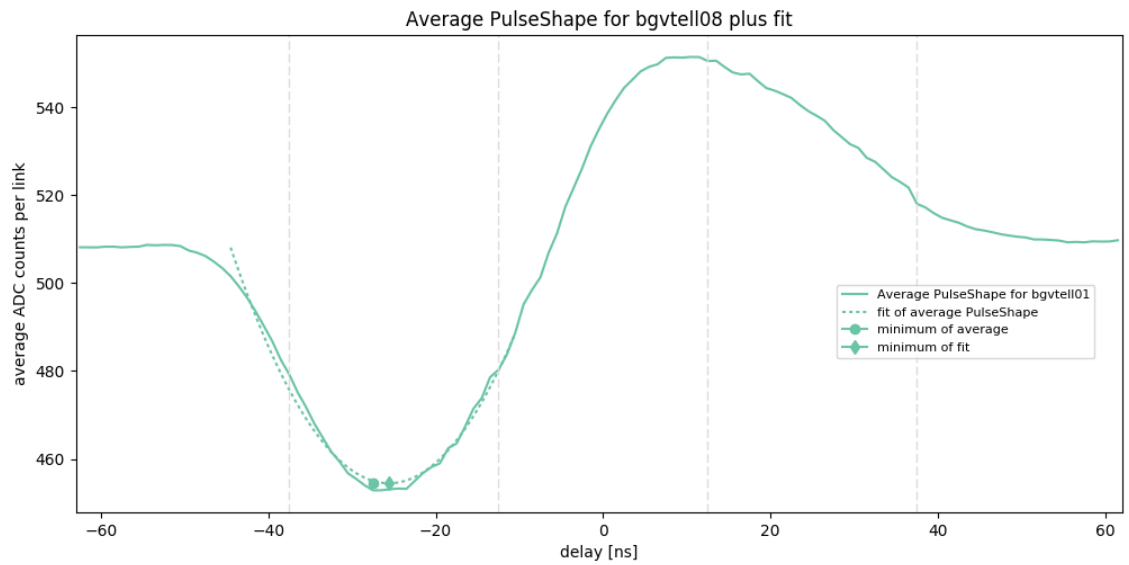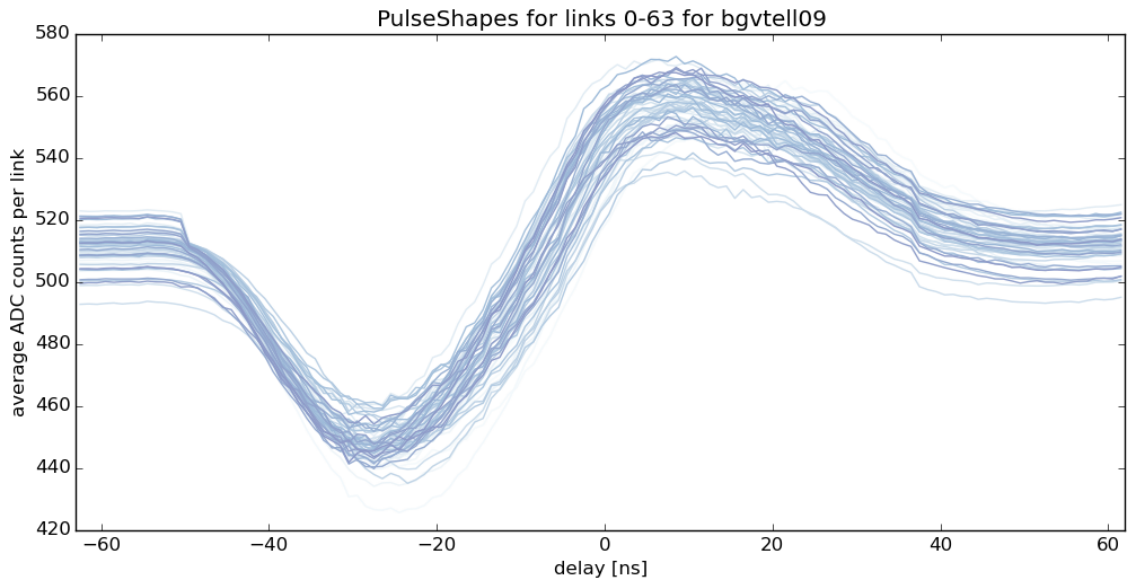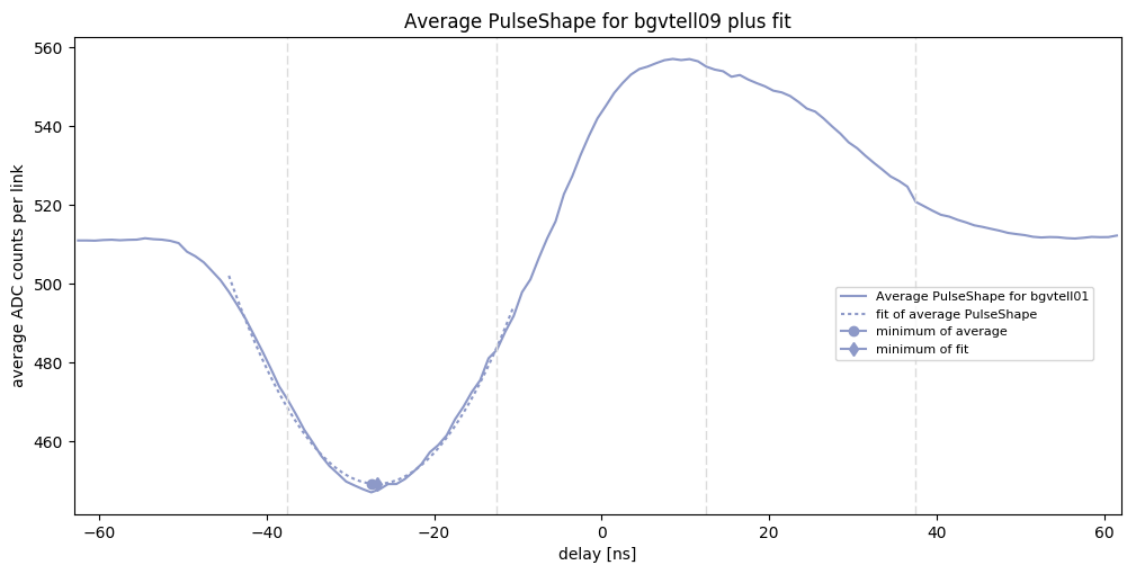Figure 3.31.: Result of the PulseShapeScan analysis for all 64 links of bgvtell02, downstream module Top-Passage (5L).
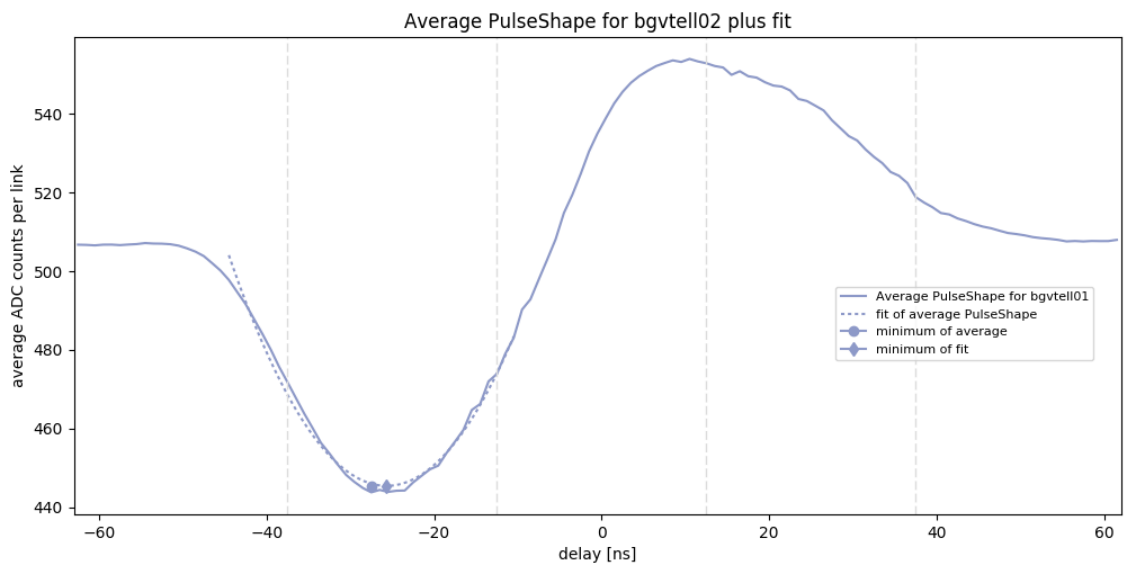
Figure 3.32.: Result of the PulseShapeScan analysis shown as average of all links of bgvtell02, downstream module Top-Passage (5L).
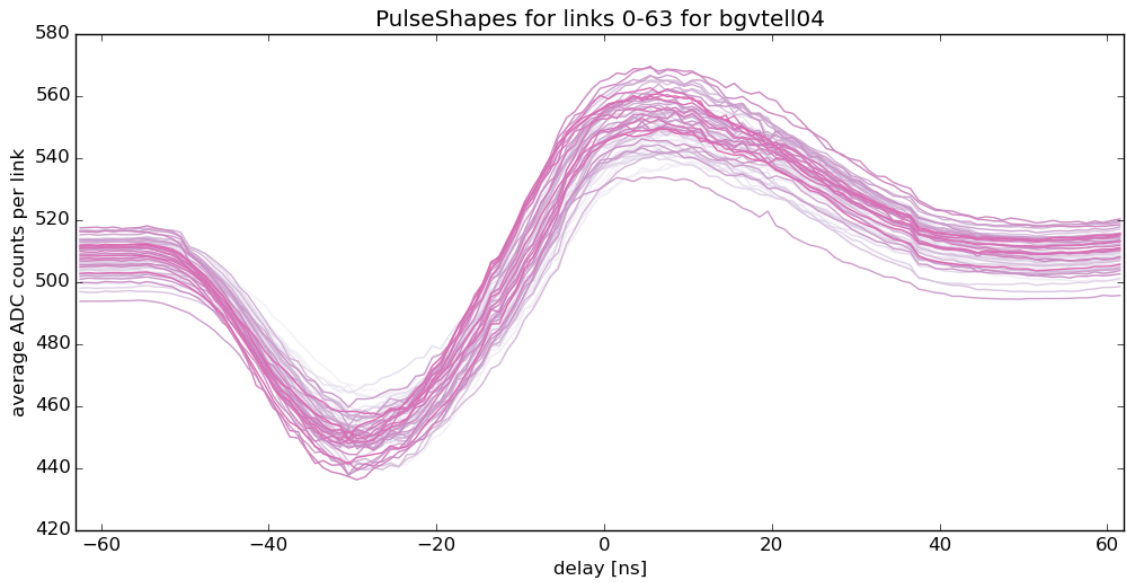
Figure 3.33.: Result of the PulseShapeScan analysis for all 64 links of bgvtell04, upstream module Top-Passage (4L).
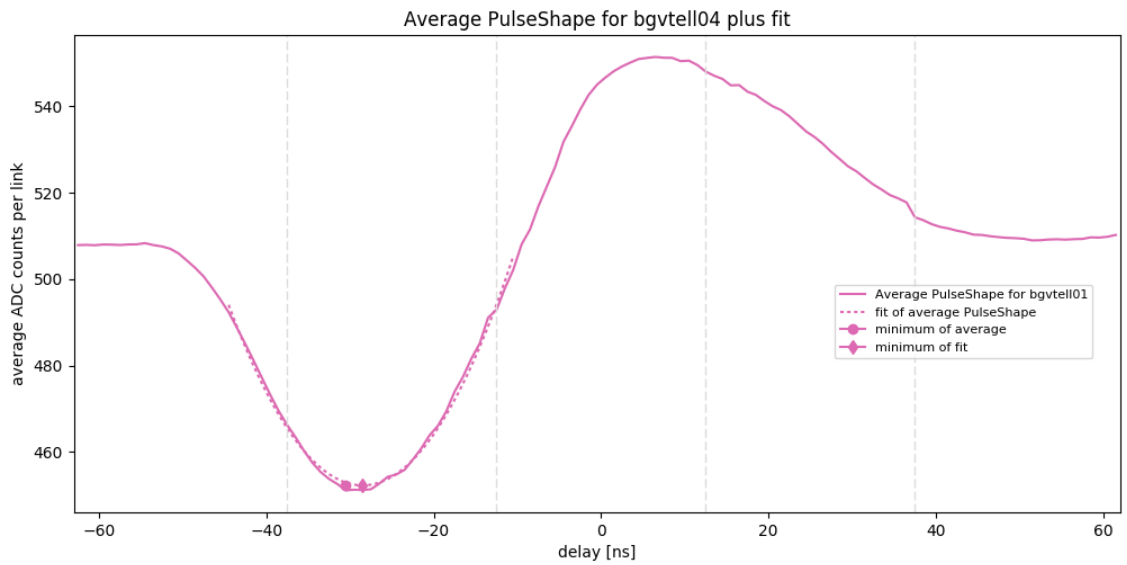
Figure 3.34.: Result of the PulseShapeScan analysis shown as average of all links of bgvtell04, upstream module Top-Passage (4L).
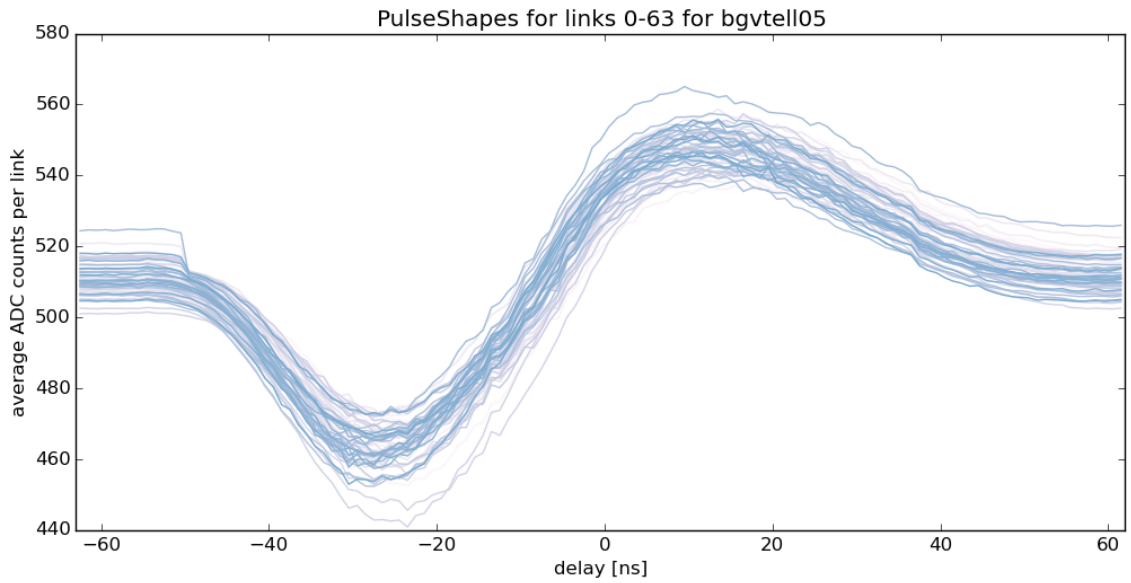
Figure 3.35.: Result of the PulseShapeScan analysis for all 64 links of bgvtell05, upstream module Bottom-QRL (4L).
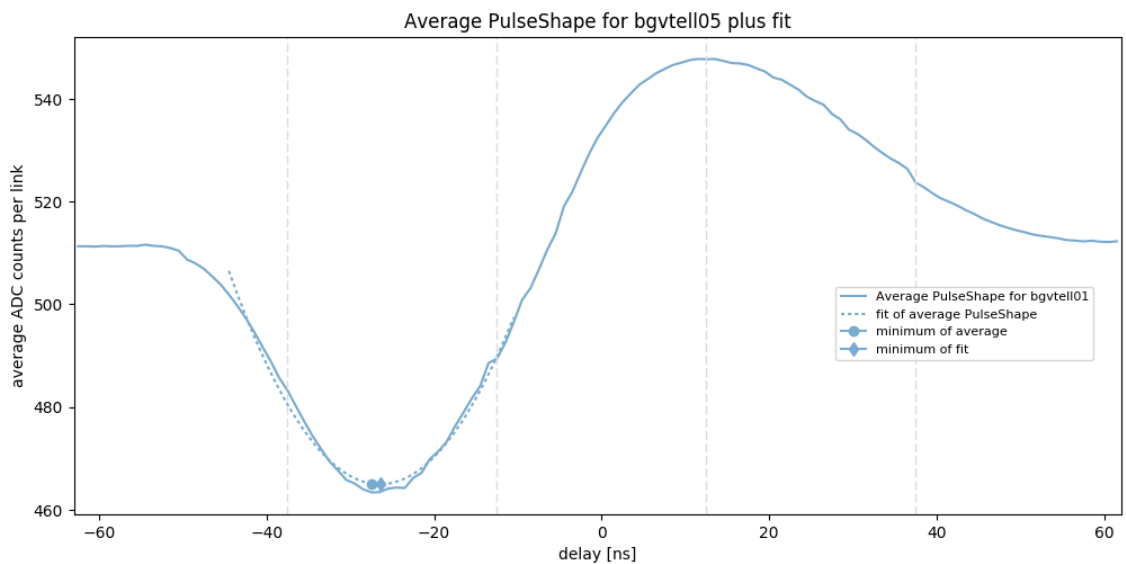
Figure 3.36.: Result of the PulseShapeScan analysis shown as average of all links of bgvtell05, upstream module Bottom-QRL (4L).

Figure 3.37.: Result of the PulseShapeScan analysis for all 64 links of bgvtell06, upstream module Bottom-Passage (4L).

Figure 3.38.: Result of the PulseShapeScan analysis shown as average of all links of bgvtell06, upstream module Bottom-Passage (4L).

Figure 3.39.: Result of the PulseShapeScan analysis for all 64 links of bgvtell07, downstream module Bottom-Passage (5L).

Figure 3.40.: Result of the PulseShapeScan analysis shown as average of all links of bgvtell07, downstream module Bottom-Passage (5L).

Figure 3.41.: Result of the PulseShapeScan analysis for all 64 links of bgvtell08, downstream module Bottom-QRL (5L).

Figure 3.42.: Result of the PulseShapeScan analysis shown as average of all links of bgvtell08, downstream module Bottom-QRL (5L).

Figure 3.43.: Result of the PulseShapeScan analysis for all 64 links of bgvtell09, upstream module Top-QRL (4L).

Figure 3.44.: Result of the PulseShapeScan analysis shown as average of all links of bgvtell09, upstream module Top-QRL (4L).

3.6. Calibration of the TFC bunch counter

The BGV is designed to measure the transverse beam width for beam 2 for the whole beam as well as bunch-by-bunch. To assign the correct bunch ID to the data from the BGV, the LHC system information and BGV information have to be aligned. As described in subsection 3.3.1, the timing and fast control (TFC) receives the LHC clock and the trigger signal to propagate it to the DAQ system. In addition, the TFC readout supervisor ODIN provides the bunch crossing ID (BCID) information, which gets written into the raw data bank. This BCID information was originally calibrated to the location of LHCb's VELO on the LHC. Due to the distance between Point 8 (LHCb) and Point 4 (BGV) of about 13.5 km, there is a certain offset between the original TFC BCID information and the actual LHC bucket number passing through the BGV.

In order to find the offset, data were taken during times when the LHC was filled with only a few bunches. Fewer filled slots (of the 3564 possible slots) facilitate the correct identification of the respective bunches. The LHC provides the information of filled buckets, and one bunch slot contains 10 buckets. The information which LHC buckets are filled, is retrieved from the LHC logging database which contains detailed information about each fill. The bunch information (BCID) from the TFC is taken directly from the raw data bank of the acquired data.
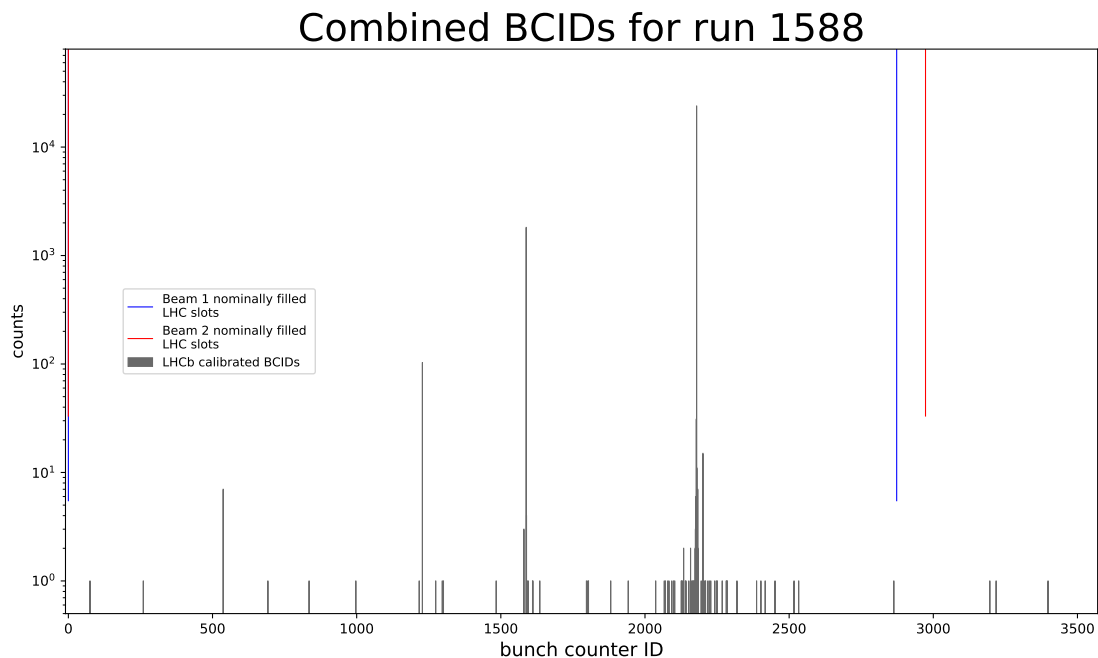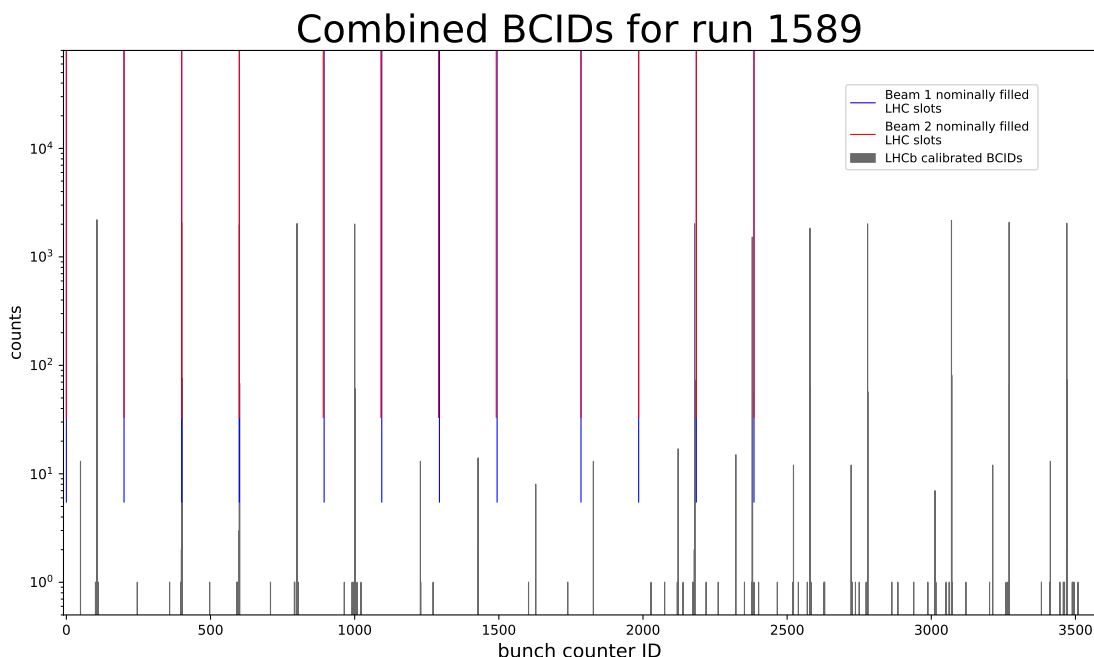

Figure 3.45.: BGV data taken with BCID calibrated to LHCb location in grey, combined with LHC nominally filled slots for beam 1 in blue and beam 2 in red.

To compare the BCID information provided by the TFC (which is the BCID calibrated to the VELO location) to the information of the nominally filled LHC buckets, the BCID numbers (ranging from 0 to 3563) are plotted against the number of events and superimposed with the LHC bucket information.

Figure 3.45 shows such a plot where the BCID events are plotted in grey and the nominally filled LHC buckets are plotted in blue for beam 1 and red for beam 2.

The histogram of figure 3.45 contains 4 BCIDs with a significant amount of entries. The corresponding fill contained two bunches per beam in total, one pilot bunch and a nominal bunch. In that fill, slots 0 and 2873 were filled for beam 1 and slots 0 and 2973 were filled for beam 2.

The offset per beam can be determined by comparing the distance between the 4 relevant BCIDs with the expected distance between the filled bunches of beam 1 and beam 2.

To test the offset, the data set is plotted with the respective shifts for beams 1 and 2 as shown in figure 3.46. The grey lines originating from the top indicate the position of the filled slots in the LHC, the blue and red lines in the top and bottom half of the plot originate from BGV data with different thresholds applied and shifted by the assumed offset.
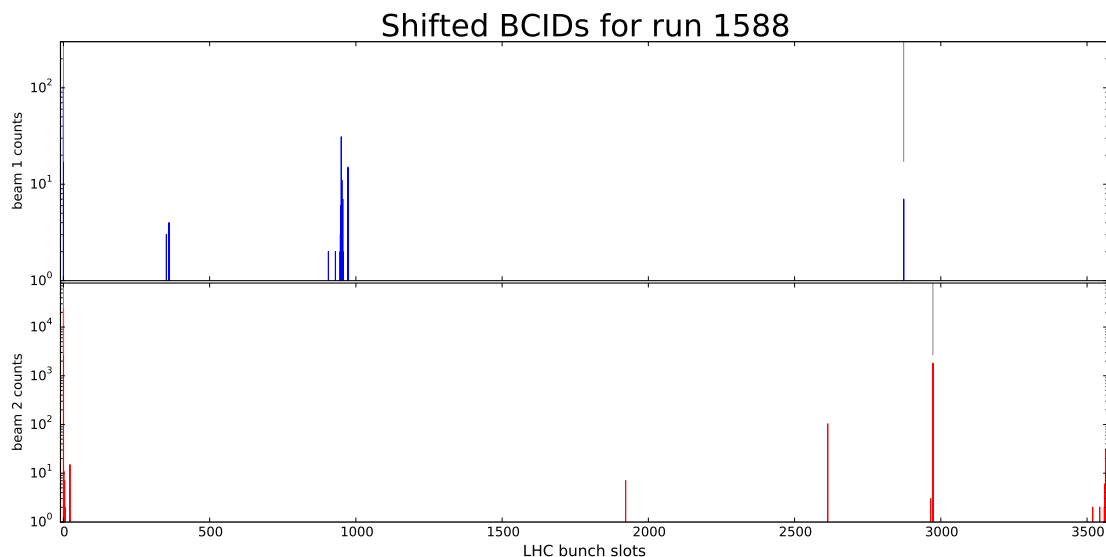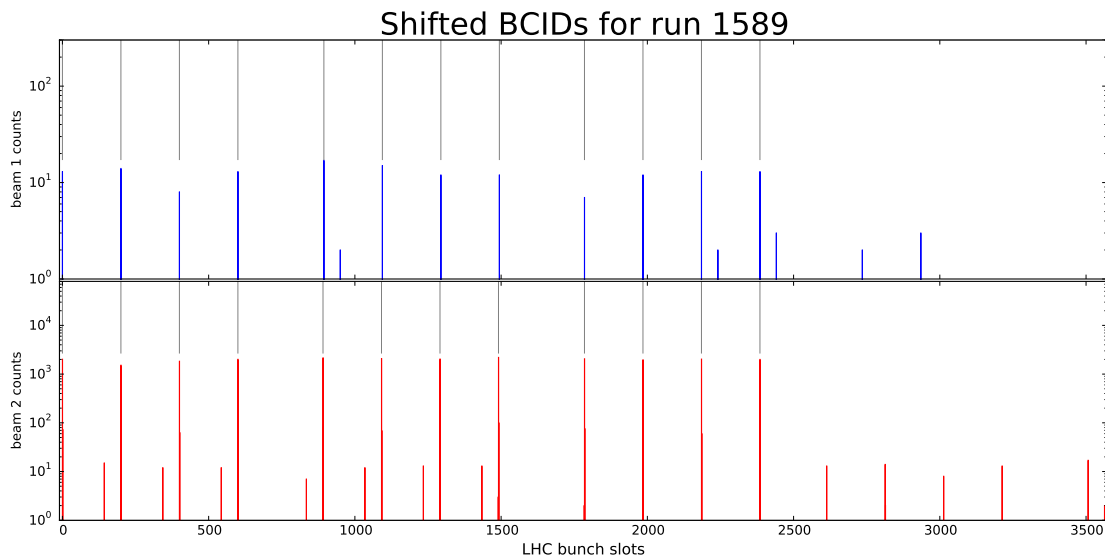

Figure 3.46.: Data sample shifted in respect to the LHC filled slots (indicated by the grey lines). The histogram on top shows the BGV data shifted to fit the LHC filled slots of beam 1 while the lower histogram shows the BGV data shifted to fit the LHC filled slots of beam 2. The BGV data set plotted for beam 1 has a threshold applied to exclude entries with counts greater than 100.

The offset looks correct for the case where only two bunches per beam are circulating in the LHC.

The offset between LHC filled buckets and LHCb BCID per beam is

$$\text{offset}_{beam1} = 2346$$
$$\text{offset}_{beam2} = 1395$$

and thus has to be implemented in the TFC ODIN firmware.

To verify that the determined offset is correct, it was applied to other fills that contain more bunches. The data from Run 1589 is an example of a dataset with 12 filled slots, where the determined offsets were applied. Figures 3.47 and 3.48 show the filled slots for Run 1589 before and after the shifts were applied.

Figure 3.47.: BGV data taken with BCID calibrated to LHCb location in grey, combined with LHC nominally filled slots for beam 1 in blue and beam 2 in red.

The analysis of the filled buckets shows that the BGV does not only measure beam 2-gas interactions, but also interactions from beam 1 with some residual gas. This is due to beam 1 protons, which collide with residual gas (the vacuum of 10^{-11} mbar still contains some atoms) inside the beam 1 beam pipe and a large trigger window of the scintillator trigger.
Figures 3.46 and 3.48 show that the amount of beam 1 events is at least one order of magnitude lower than for beam 2. Since the BGV is designed to measure the transverse beam profile of beam 2, data from beam 1 are not desired and need to be suppressed. The knowledge of the precise bucket number passing through (or next to) the detector allows

Figure 3.48.: Data sample shifted in respect to the LHC filled slots (indicated by the grey
lines). The histogram on top shows the BGV data shifted to fit the LHC
filled slots of beam 1 while the lower histogram shows the BGV data shifted
to fit the LHC filled slots of beam 2. The BGV data set plotted for beam 1
has a threshold applied to exclude entries with counts greater than 100.

for writing a mask in the TFC firmware which inhibits triggers and data acquisition from
beam 1 interactions.

Another feature that is indicated by the data is that it could be possible for the BGV to
not only measure the transverse beam profile, but also get information on charges that
drift outside the nominally filled buckets. These charges are called "ghost charges" in
the vocabulary of the LHC experiments' luminosity groups and are defined in detail in
section 4.1.

Figure 3.45 can be used as example of possible ghost charges. The four buckets that are
nominally filled are represented by the four BCIDs that contain higher count rates, of the
order of 10 to 10^4. In addition, there are several BCID bins that contain charge, with
counts between one and ten. These "filled" BCIDs can either be noise from the detector
or actual ghost charges, and should be verified in future tests when the different tools to
take ghost charge data are used at the same time.

3.7. Photoelectron peak measurement with the complete detector setup

3.7.1. SiPM photoelectron peaks

In order to understand the gain in the detector and how many photons are measured for a minimal ionising particle, data were taken with random triggers at temperatures between 15 °C and −20 °C. The gain can be estimated by taking the charge of one pixel divided by the electron charge e.

One way of acquiring the charge of one pixel is to make a pulse height diagram. Hereby, the pulse height is plotted against how often a specific pulse height is measured.

As shown in section 3.3, the SiPMs not only consist of channels, but of 96 pixels per channel. Since the pulse height is the same for every pixel, the total output signal of a SiPM is given by the amount of pixels that were fired during a trigger window [42]. This means that the signal height of a SiPM is discrete and the distance between the pulse heights is constant. Figure 3.49 shows an example of a pulse height spectrum.
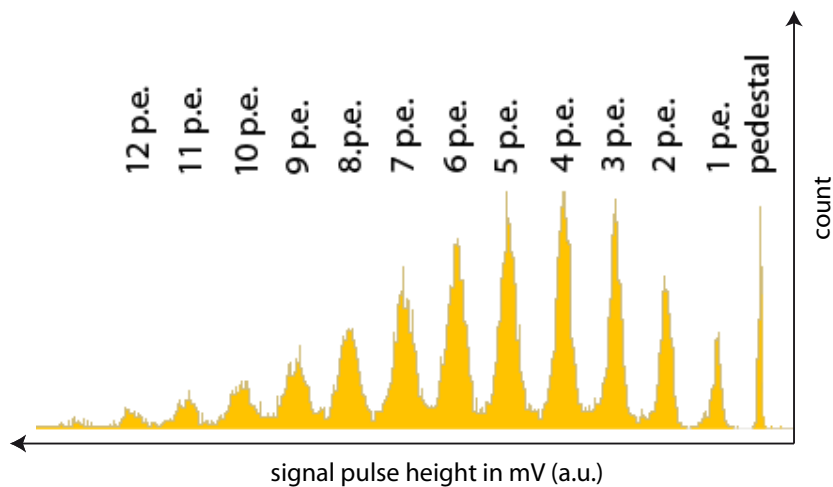
Figure 3.49.: Example of a pulse height spectrum taken from a Hamamatsu 10931 SiPM with an oscilloscope. [43]

The peaks of this spectrum are called "photoelectron peaks" (p.e. peaks) since they relate to the number of fired pixels from photon interaction. However, there is an intrinsic noise in SiPMs which causes the pixels to fire without photon interaction. This noise is called "dark counts" and is caused by thermal excitation. It increases with temperature and applied voltage. As a result, since the signal per pixel is constant, the signal generated from a dark count cannot be distinguished from a signal generated by a photon [44].

The indistinguishability between the origin of a SiPM signal is used to acquire the pulse height spectrum for the BGV's SiPM. The data for the pulse height diagram were taken by using dark counts. To acquire dark count data, the SiPMs were biased and data were taken with random triggers while no beam was circulating in the LHC.

3.7.2. Data acquisition parameters

The goal of taking dark counts in this section is to make a pulse height diagram to measure the average distance between the photon peaks. Hereby data were taken at different overvoltages and at different temperatures between about 15 °C and about −20 °C. Since dark counts are the SiPM's intrinsic noise and occur randomly, the trigger can also be timed randomly. This means, however, that the signal will not only be sampled at its maximum, but anywhere on the pulse shape as can be seen in the relevant figures.

The temperature was set for all SiPMs of all 8 modules to about 15 °C (Run 1848, used to explain corrections applied to the data), 10 °C, 0 °C, −10 °C and −20 °C. The 16 SiPMs per module are biased by four different voltages, as mentioned in section 3.4. While the detector's SiPMs are normally biased with an overvoltage (OV) of 3.5 V, data for the photon peak measurement was taken with OVs of 2.5 V, 3.5 V, 4.5 V and 5.5 V respectively. The idea behind setting different OVs is that the photon peak distances are dependent on the overvoltage, hence a higher OV results in a greater photon peak distance. Setting the different OVs at once instead of taking four files with different OVs reduces DAQ time and analysis time.

Table 3.2 shows the parameters for the data presented in this chapter. The OV was not properly set for the downstream modules for run 2052 at 10 °C. All SiPMs are biased with a 3.5 V OV. This means that for further data analysis the data from Run 2052 is only used for 3.5 V OV data points and excluded for others.

			Overvoltage			
Run number	Temperature	Module	SiPM 0-3	SiPM 4-7	SiPM 8-11	SiPM 12-15
1848	15 °C	all modules	3.5 V	3.5 V	3.5 V	3.5 V
2052	10 °C	all upstream modules	5.5 V	4.5 V	3.5 V	2.5 V
2052	10 °C	all downstream modules	3.5 V	3.5 V	3.5 V	3.5 V
2053	0 °C	all modules	5.5 V	4.5 V	3.5 V	2.5 V
2054	−10 °C	all modules	5.5 V	4.5 V	3.5 V	2.5 V
2055	−20 °C	all modules	5.5 V	4.5 V	3.5 V	2.5 V

Table 3.2.: Parameters for the photoelectron peak data acquisition.

Figure 3.50 shows the temperatures, measured at each SiPM, over the applied bias per SIPM for the upstream top passage module. The four different voltages per temperature represent the 4 different OVs. Since the breakdown voltage and thus the OV is dependent

on the temperature, the bias decreases with the temperature. The bias per SiPM at a temperature T is given by the expression

$$V_{bias}(T) = V_{BD}(25\ ^\circ C) + 0.0537\frac{V}{K} \cdot (T - 25\ ^\circ C) + OV, \tag{3.1}$$

with $V_{BD}(25\ ^\circ C)$ being the breakdown voltage that was measured at 25 °C [31] and 0.0537 being the temperature coefficient (53.7 mV/K) [29].

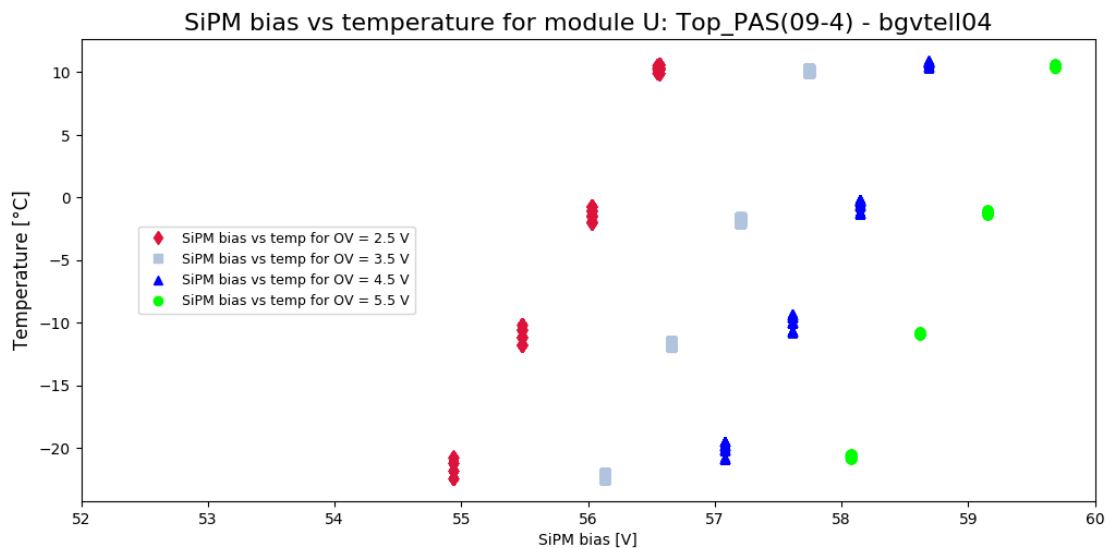Figure 3.50.: Temperatures and SiPM bias for upstream top passage module (09-4, bgvtell04).

The current of each SiPM was measured as well and is shown in figure 3.51. While the SiPM bias scales linearly with the temperature (and is set in the detector settings), the current changes exponentially with the temperature and is a result of bias and temperature.

The temperature fluctuates for the SiPMs in each OV group since the cold fluid enters each module half through a small pipe on one side (e.g. SiPM/Beetle 0 and SiPM/Beetle 8) and exits on the opposite side (SiPM/Beetle 7 and SiPM/Beetle 15) [45]. There resulting temperature gradient can be observed in both figures by a temperature spread of a few degrees.

While the overvoltages were applied for the SiPMs, Beetles are used for the "by-channel" readout. This is why several of the following plots show the expression "Beetle" instead of SiPM. They are, in this section, used interchangeably.
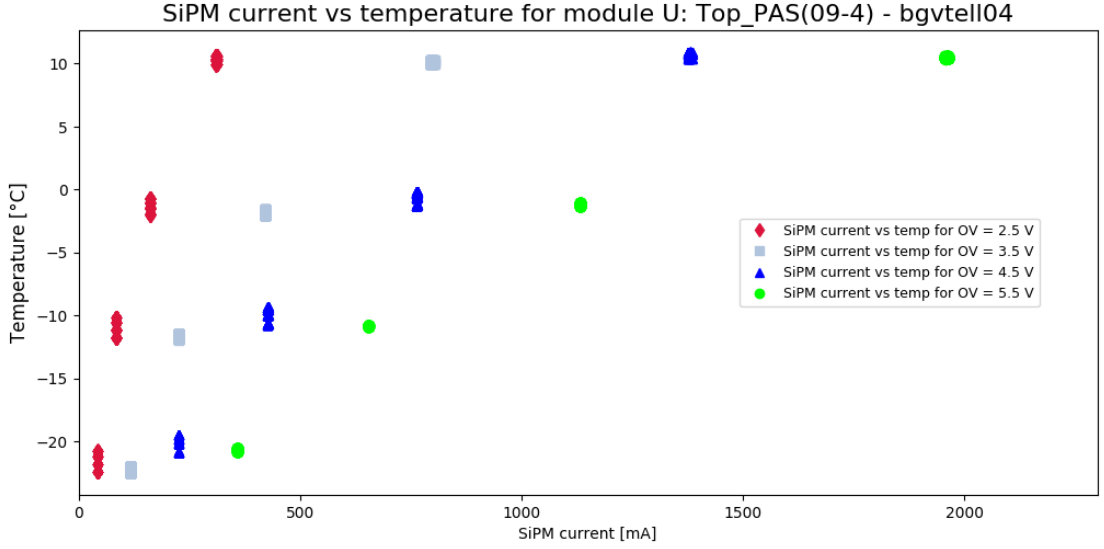
Figure 3.51.: Temperatures and SiPM current for upstream top passage module (09-4, bgvtell04).

3.7.3. Data corrections

The data acquired with the BGV are subject to a number of correctable effects. The corrections are implemented in the analysis and will be implemented in the TELL1s as well. To explain these corrections, data from an acquisition at 15 °C and an OV of 3.5 V for all SiPMs is used.

The corrections, which are applied to all data sets in this section, are summarised in expression 3.2 and include pedestal subtraction (pedSub), common mode subtraction (CMS) and channel correlation correction (CORR). They are described in more detail in the following paragraphs.

$$
\begin{aligned}
ADC_{raw_i} - pedestal_i &\longrightarrow ADC_{pedSub_i} \\
ADC_{pedSub_i} - CM &\longrightarrow ADC_{CMS_i} \\
ADC_{CMS_i} - x \cdot ADC_{CMS_{aggr}} &\longrightarrow ADC_{CORR_i}
\end{aligned}
\tag{3.2}
$$

Pedestals represent the analog zero value. Each analog link has one pedestal value at around 512 ADCs. They are explained in more detail in section 3.3.4.

Pedestal subtraction is performed to ensure that data from all links are on the same ADC level and the noise is around zero. The pedestal for each channel is derived by scanning for values around 512 ADCs and taking the average of these values. The pedestal per link is then subtracted from the raw ADC value of each channel (inside the link). Figures 3.52a and 3.52b are examples of a data set before and after pedestal subtraction.
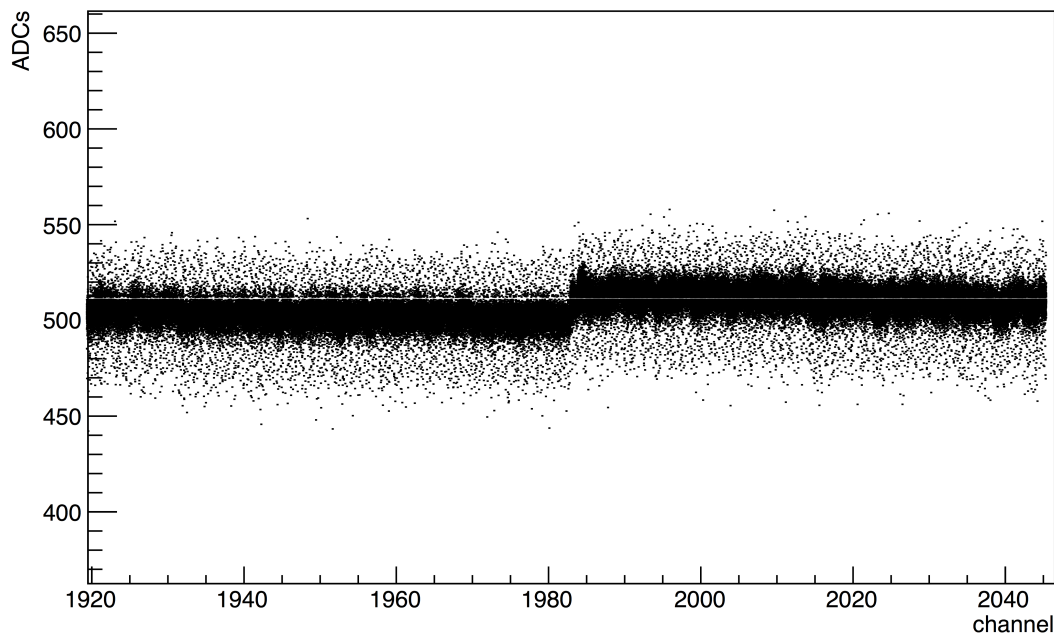
(a) Scatter plot of SiPM raw data ADCs plotted against the 128 channels of Beetle 0 (channel range 1920-2047) at 15 °C.
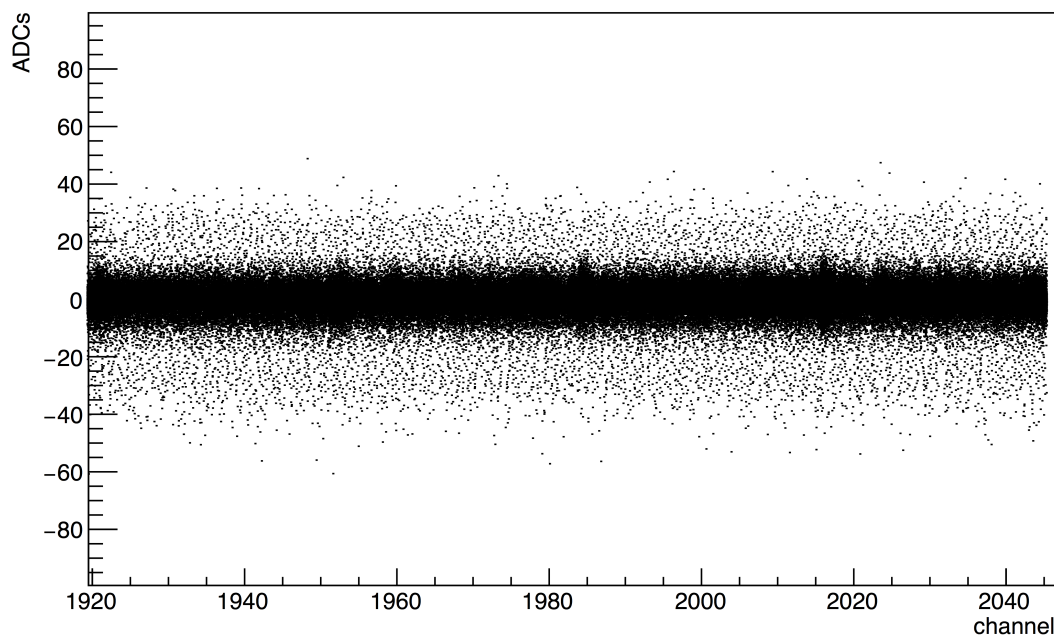
(b) Scatter plot of pedestal subtracted ADCs plotted against the 128 channels of Beetle 0 (channel range 1920-2047) at 15 °C.

Figure 3.52.: Raw data per channel of one SiPM (Beetle 0) before and after pedestal correction.

In order to see potential photon peaks, data from figure 3.52b have to be displayed differently. The thick line containing entries between about -10 and +10 ADCs represents the pedestal of the data, while the entries further from the pedestal are due to actual dark counts from the SiPMs. The dark counts contain a structure with lower ADC counts occurring more often than higher ADC counts.

To make this structure visible, the data per Beetle (128 channels) are projected onto the ADC-axis (this projection is referred to as "y-projection" in this section). The count of data entries per ADC value is shown on a logarithmic scale, resulting in a cone-shaped histogram with the pedestal being the tip of the cone and the dark counts being the two sides of the cone.

Figure 3.53 shows such a projection of the pedestal subtracted data plotted as ADCs versus counts on a logarithmic scale. The cone shaped projection in figure 3.53 (and all following similar cones) is asymmetric because of the small difference between signal and overshoot (in the positive ADC range) as was shown in section 3.5.6.

The second correction is applied by deriving the common mode per link and subtracting it from the pedestal subtracted data. To calculate the (linear) common mode per link (which contains 32 channels each), the pedestal subtracted ADC values per link are summed up and divided by 32. The common mode is subtracted from each pedSub ADC value to receive the CMS ADC value. Figure 3.54 is an example of data of one SiPM with pedestal subtraction and common mode subtraction applied. The CMS correction reveals a constant structure in the negative ADC range that was not visible after the pedSub correction.

The last correction applied to the data is the channel correlation correction (CORR). As described in section 3.3, an attenuator circuit between the SiPMs and the Beetles attenuates the SiPM signal to accommodate for the Beetle's designed input of about $22 \cdot 10^3$ electrons per MIP (compared to the SiPM output of about 10^7 electrons per MIP). However, as described in detail in [31], some connectors of this circuit are coupled to each other, which results in some cross-talk between the channels.

To correct for these channel correlations, the CMS value of each "victim" channel gets subtracted by the CMS value of an "aggressor" channel, multiplied by the respective correlation factor x, as shown in the last line of expression 3.2.

Figure 3.55 is an example of the data from one SiPM after the channel correlation correction. The correction reduces the pronouncement of the structure but doesn't remove it. It is currently not understood why that correction has such an impact on the data; however, as can be seen in other data samples, the impact is small enough to be ignored in the present analysis.
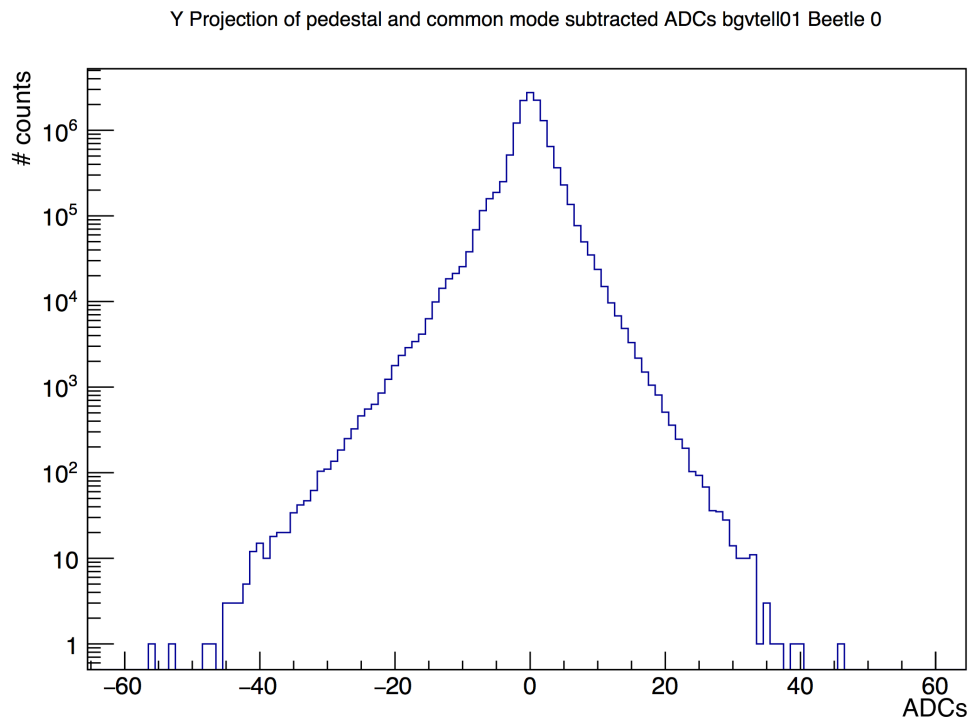
Y Projection of pedestal subtracted ADCs bgvtell01 Beetle 0
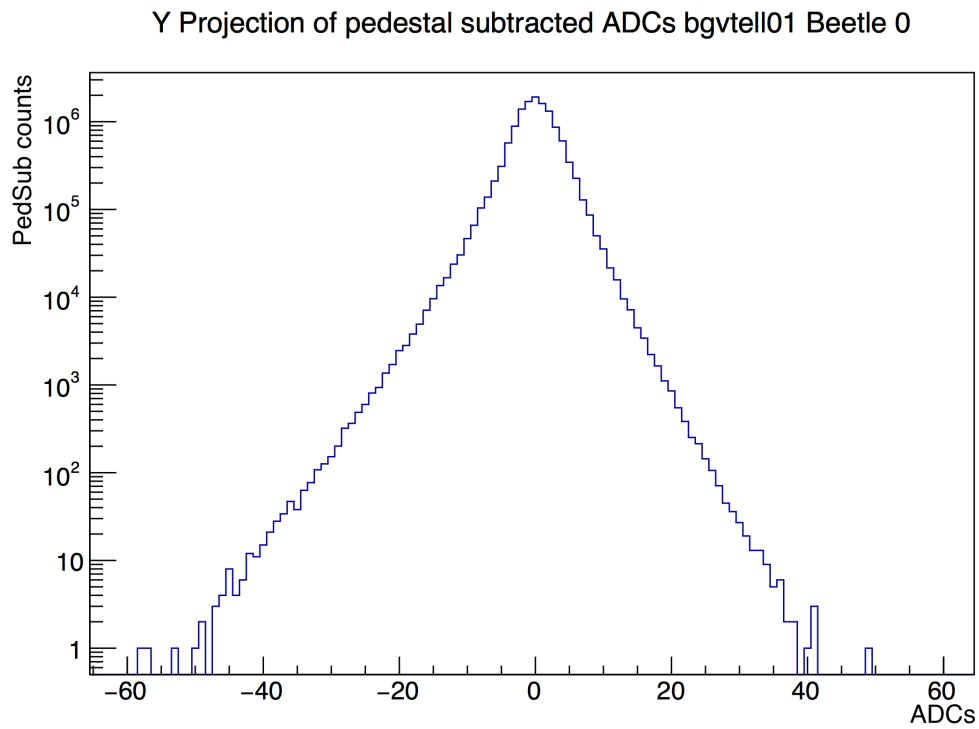
Figure 3.53.: Y-projection (ADC counts) of pedestal subtracted data of SiPM 0 at 15 °C.

Y Projection of pedestal and common mode subtracted ADCs bgvtell01 Beetle 0

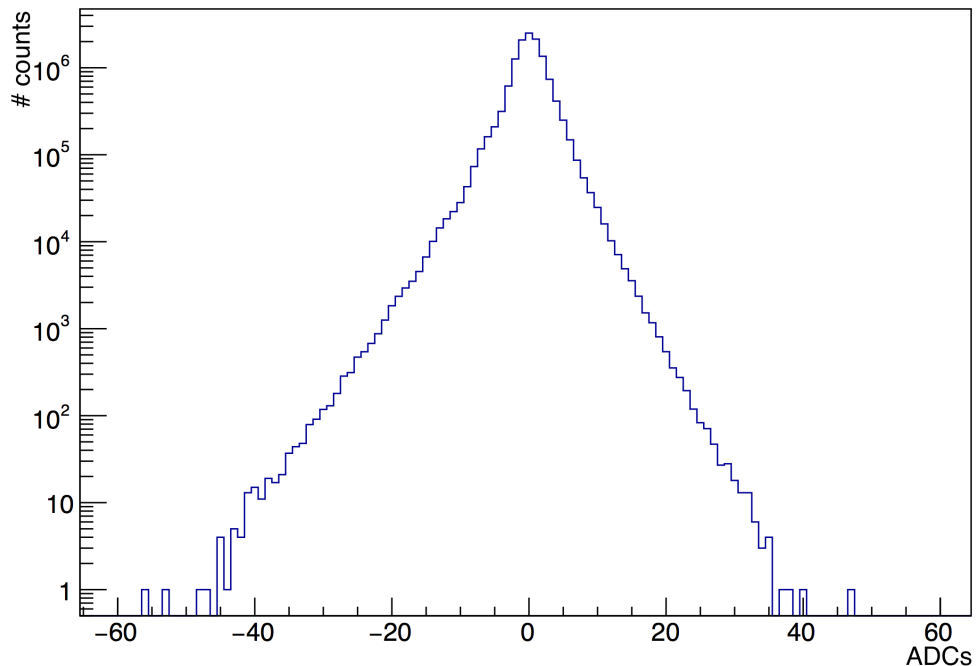Figure 3.54.: Y-projection (ADC counts) of pedestal subtracted and common mode subtracted data of SiPM 0 at 15 °C.

Figure 3.55.: Histogram after application of the three corrections of SiPM 0 at 15 °C.

3.7.4. Derivation of photoelectron peaks and distances

The structure that is visible in figures 3.54 and 3.55 can be interpreted as "photon peaks" and could already be used to derive the distance between the photon peaks in ADC counts.

To facilitate finding the exact position of each photon peak, the resulting histogram after all corrections were applied (fig. 3.55) and the histogram resulting after pedestal subtraction (fig. 3.53) are normalised to 1. This normalisation is done by scaling each bin with the normalisation parameter, which is 1 divided by the integral of the (pedSub or all-corrections-applied) histogram. The normalised, all-corrections-applied histogram is then divided by the normalised pedestal subtracted histogram, resulting in a histogram like shown in fig. 3.56. Normalisation and division were performed on the histograms themselves inside a ROOT-macro (using ROOT version 5.34/36 [46]).

The photon peaks are well pronounced and the distance between them can be determined by comparing the ADC values for the first three photon peaks in the negative ADC range. While photon peaks do also exist in the positive ADC range, they are not as well pronounced (as the ones in the negative ADC range) and have a smaller distance between them. The reason for photon peaks in the positive ADC range is that the data were acquired with random triggers, so the raw ADC value can come from anywhere on the

Run 1848 bgvtell01 Beelte0 after corrections and division
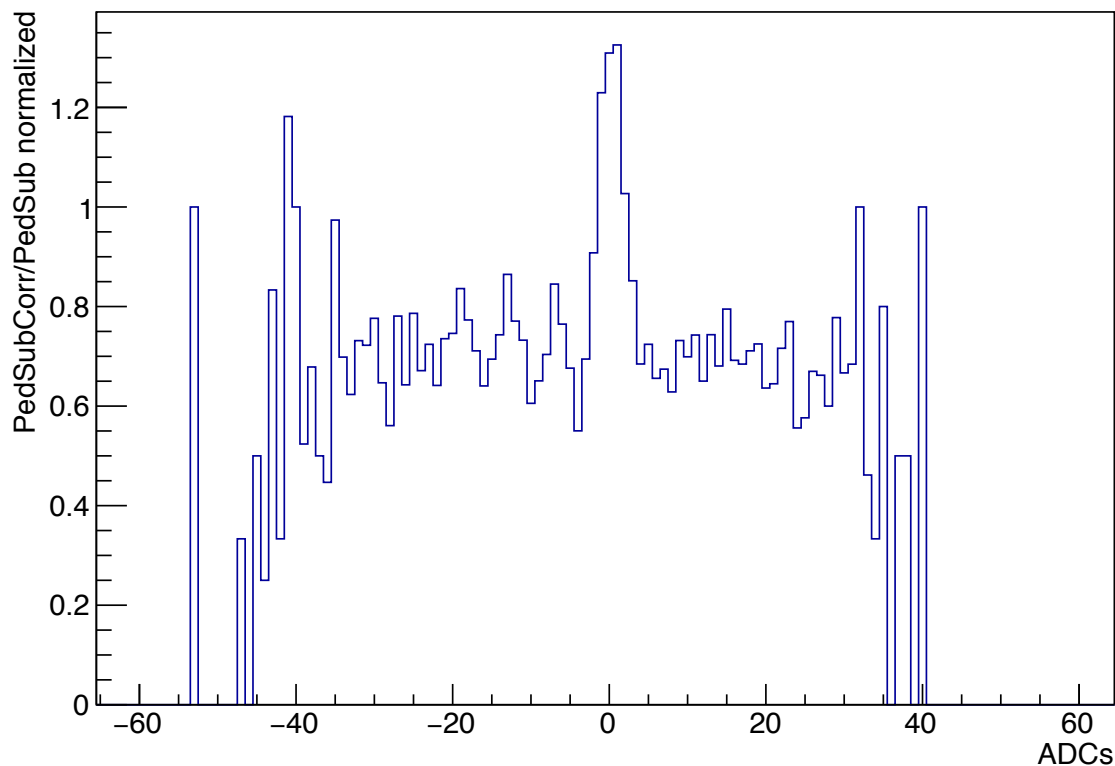
Figure 3.56.: Histogram after normalisation and division for SiPM 0 at 15 °C.

pulse shape, which has a large overshoot (see e.g. figure 3.44).

For further analysis, the photoelectron peaks in the negative ADC range are relevant, since data will be acquired with the optimal timing settings, which only sample the negative part of the pulse shape.

Figures 3.57 and 3.58 show example spectra of four different SiPMs with four different OVs applied at −20 °C. They are sorted in descending order with 5.5 V on the top, 4.5 V on the bottom and 3.5 V on the top and 2.5 V on the bottom.

By comparing the number of entries in the first photoelectron peak at 15 °C (figure 3.55) and at −20 °C (figure 3.58a), it can be derived that the dark count rate (DCR) decreases with temperature (10^5 versus 10^4 counted events).

To derive the position of the photoelectron peaks, the ROOT class TSpectrum and ROOT function SearchHighRes [47] were used. Examples for the normalised and divided spectra with the applied peak-finding algorithm are shown in figures 3.59 - 3.60. The examples show data from the same four SiPMs/Beetles at −20 °C as were shown for figures 3.57a to 3.58b. The peaks, identified with the SearchHighRes function, are saved into a list for

further use.

Figures 3.58b and 3.60b are examples of data acquired with 2.5 V overvoltage. The photoelectron (PE) peak distances cannot be derived reliably, since some peaks are missing. Data for 2.5 V overvoltage are hence discarded from the analysis.

As was pointed out earlier in this chapter, the SiPM's bias was adjusted to match the temperature. The effect of the constant overvoltage at any given temperature is that the photoelectron peak distances can also be assumed constant over the different temperatures. Figure 3.61a-c shows the derived position of the photoelectron peaks in ADC counts at different temperatures for the different overvoltages.

Since the photon peak distances are constant for the different temperatures, they are averaged by SiPM. The three plots of figure 3.61a-c are merged into figure 3.62 with the PE peaks per temperature averaged for each SiPM. Note that the average PE peaks in the positive ADC range do not make much sense. One reason for this is that the peak identification algorithm did not work as well for this part of the data, resulting in a larger spread. In addition, the first PE peak in 3.61a is missing, which makes it harder to derive a correct average distance between the PE peaks.

To get an average photoelectron peak distance per overvoltage, the average PE peaks per SiPM are also summed up and averaged, as is shown in figure 3.63. The average values per photoelectron peak (and OV) are calculated by adding up the ADC values for the 4 SiPMs per OV at each temperature ($T = [10, 0, -10, -20]$ °C) and dividing the sum by the amount of summands n, as shown by equation

$$\overline{\text{PE}(OV)} = \frac{1}{n} \cdot \sum_{T,\text{SiPM}=0}^{\text{SiPM}=3} \text{ADCs}. \tag{3.3}$$

The summand in equation 3.3 is $n = 16$ for the upstream modules and for the downstream modules SiPMs with an OV = 3.5 V (4 SiPMs times 4 temperatures). The summand reduces to $n = 12$ for the downstream modules for all OVs different to 3.5 V (4 SiPMs times 3 temperatures). This is due to the bias not being properly set for the downstream modules during data acquisition at 10 °C (run 2052). The values from this data set are excluded for the average and standard deviation calculation of OVs 4.5 V and 5.5 V for the respective modules.

The errors are derived through a standard deviation of the values used to calculated the average.
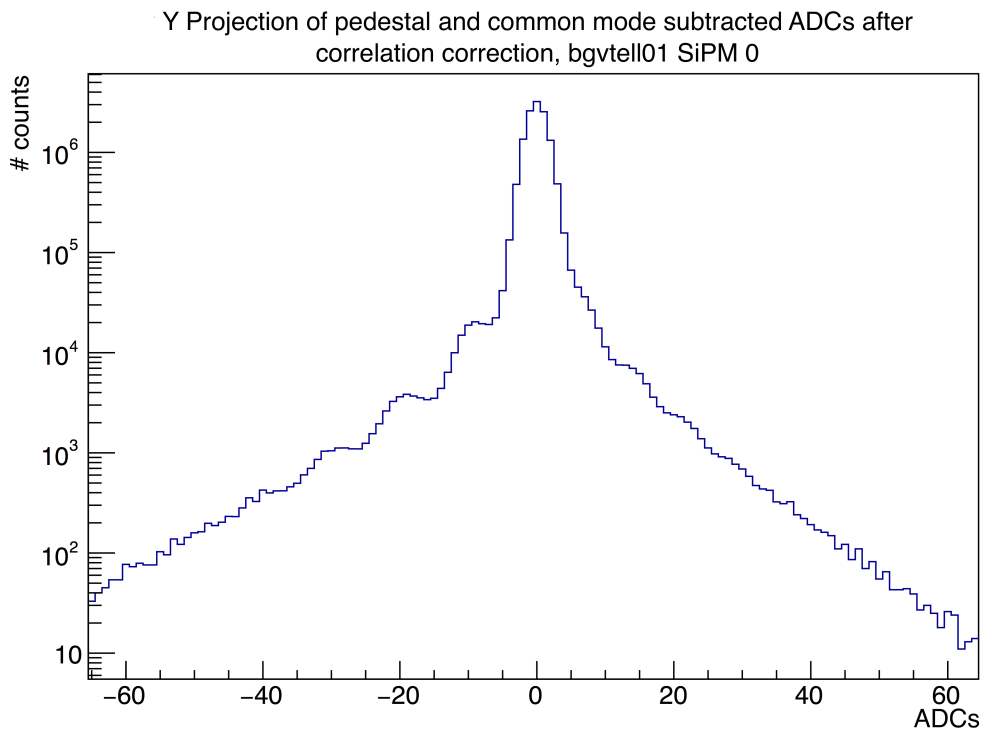
(a) 5.5 V overvoltage spectrum with all corrections applied.
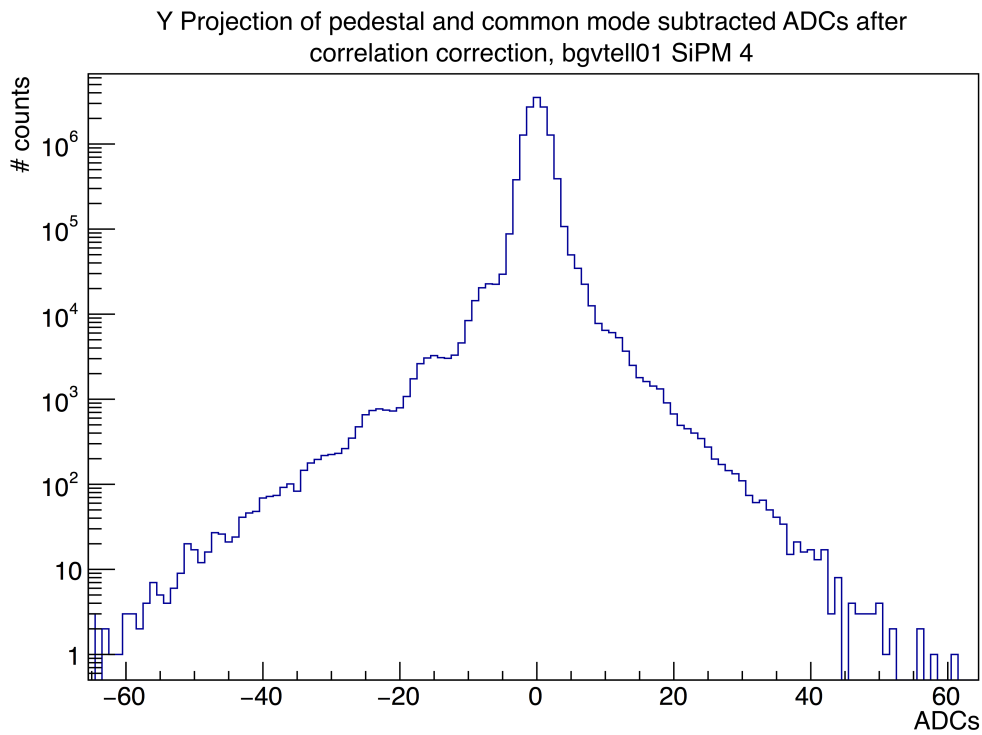
(b) 4.5 V overvoltage spectrum with all corrections applied.

Figure 3.57.: Spectra of the SiPM noise with 5.5 V and 4.5 V overvoltages applied.
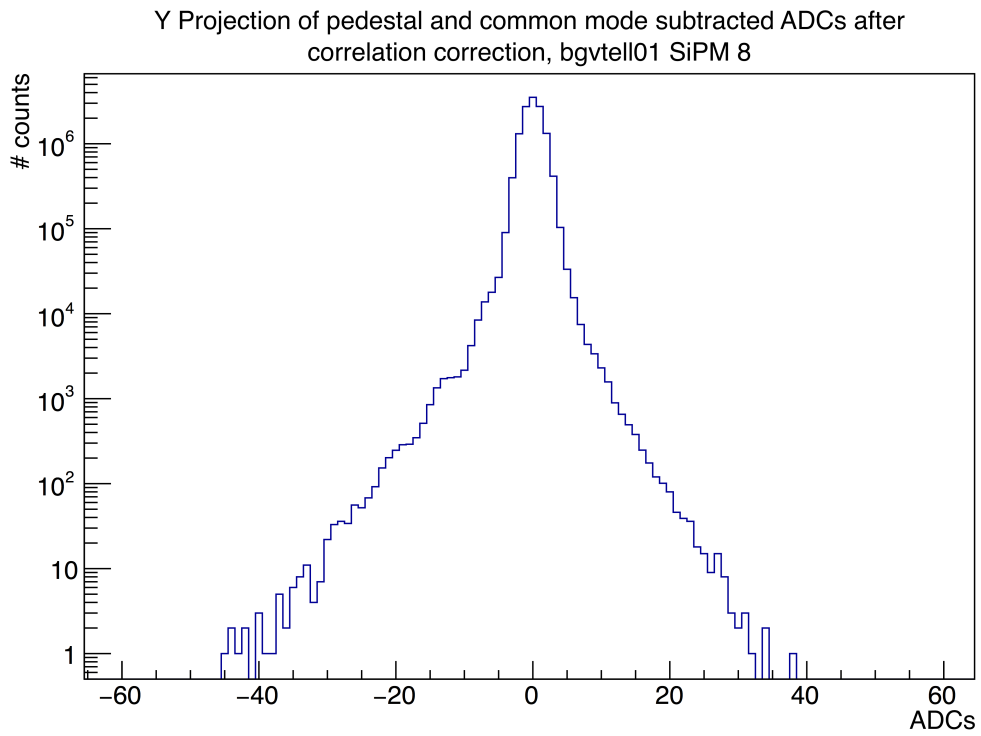
(a) 3.5 V overvoltage spectrum with all corrections applied.
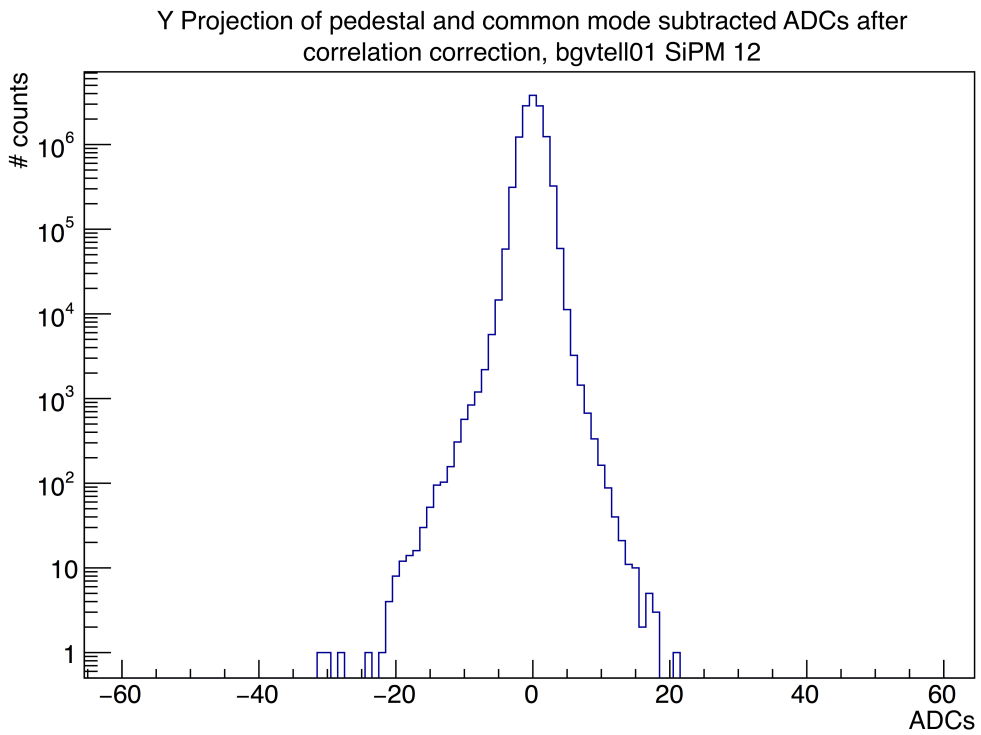
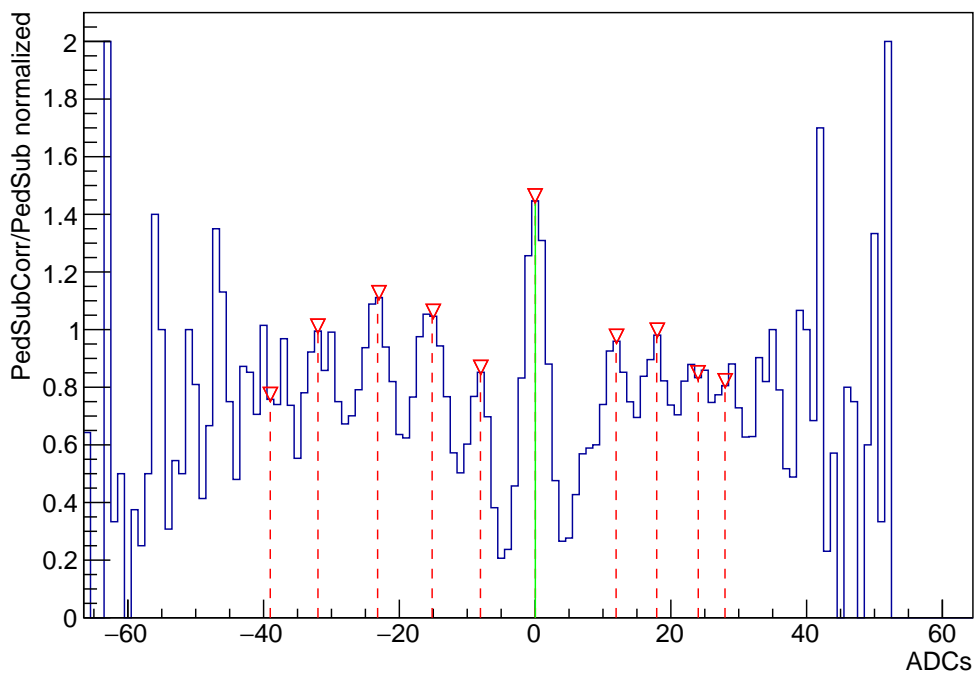(b) 2.5 V overvoltage spectrum with all corrections applied.

Figure 3.58.: Spectra of the SiPM noise with different overvoltages applied.
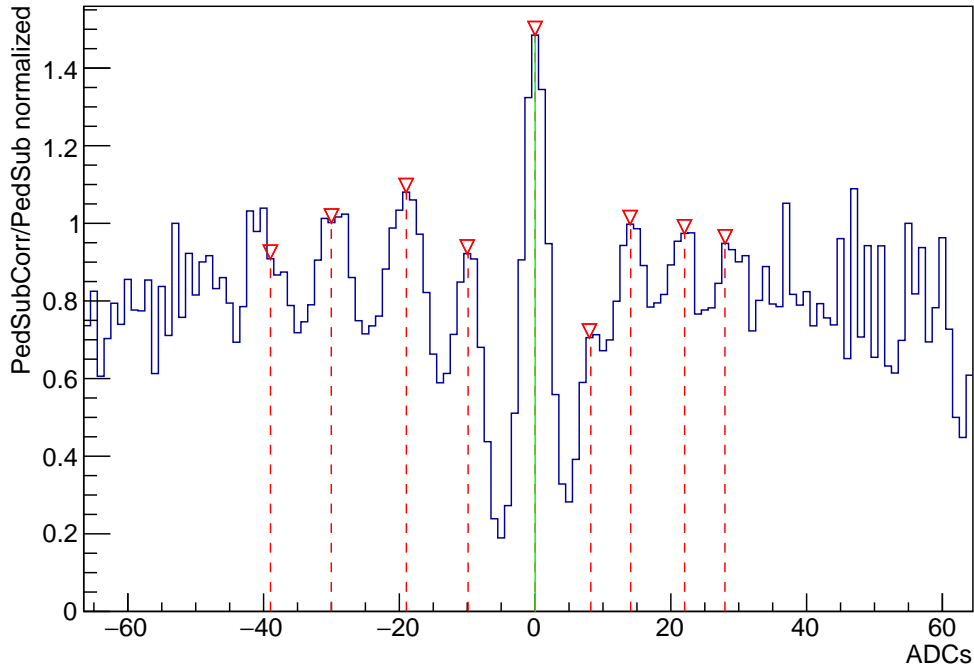
(a) Photoelectron peak spectrum after normalisation and division for 5.5 V OV.

(b) Photoelectron peak spectrum after normalisation and division for 4.5 V OV.

Figure 3.59.: Photoelectron peaks with 5.5 V and 4.5 V overvoltages applied.
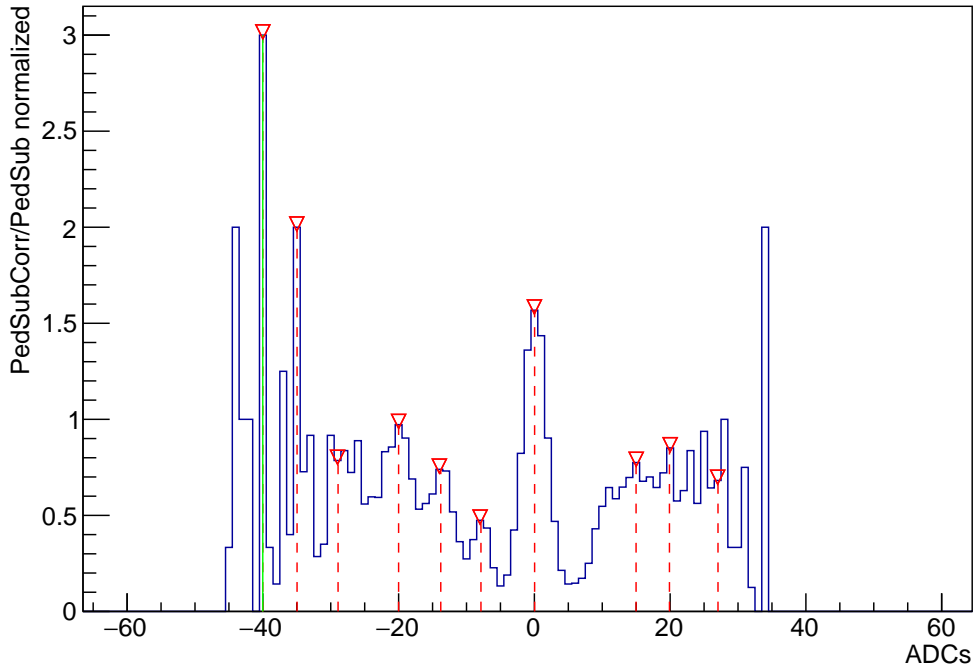
(a) Photoelectron peak spectrum after normalisation and division for 3.5 V OV.
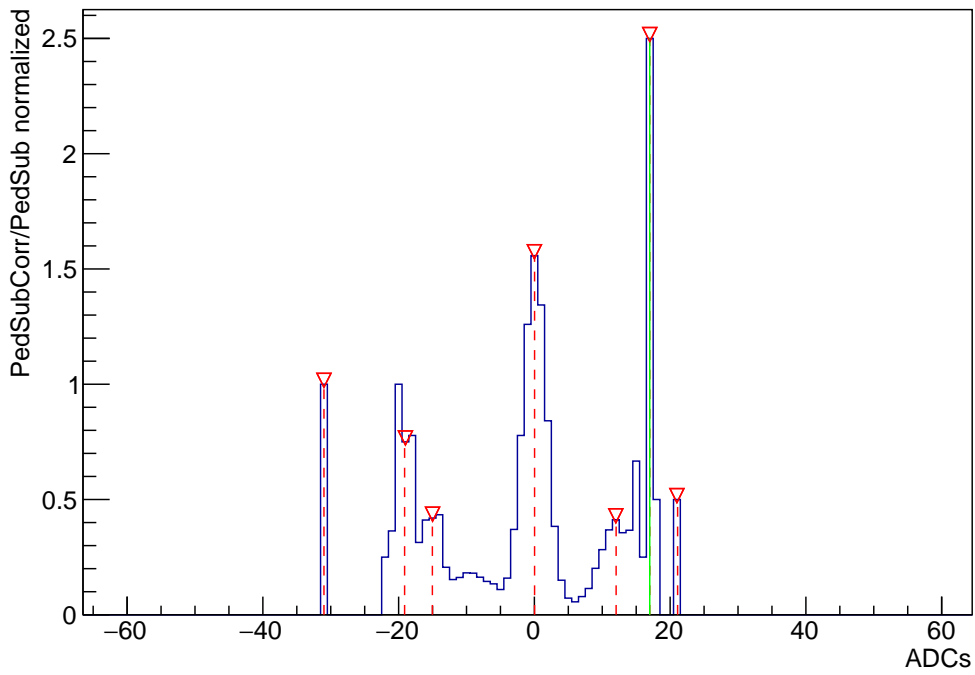
(b) Photoelectron peak spectrum after normalisation and division for 2.5 V OV.

Figure 3.60.: Photoelectron peaks with different overvoltages applied.
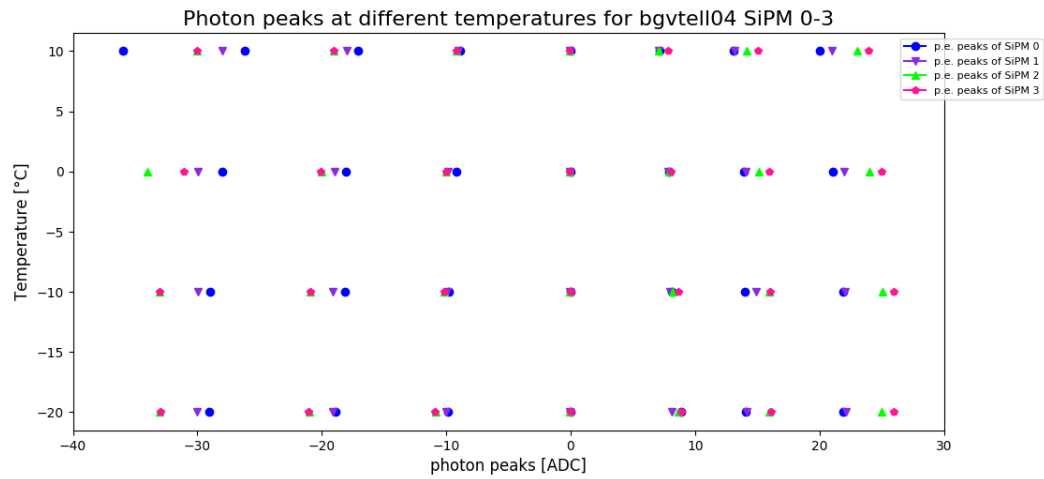
(a) Photoelectron peak distances at 5.5 V OV for the different temperatures.
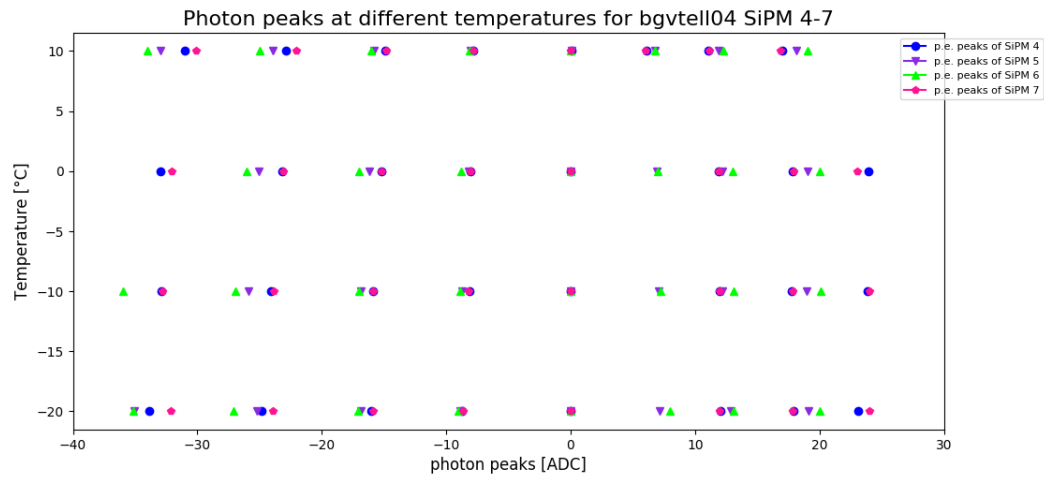
(b) Photoelectron peak distances at 4.5 V OV for the different temperatures.
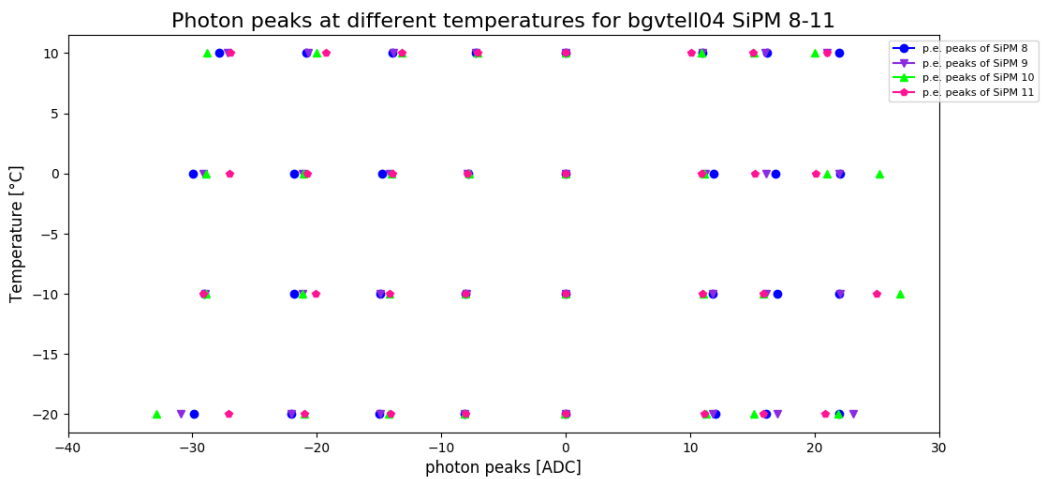
(c) Photoelectron peak distances at 3.5 V OV for the different temperatures.

Figure 3.61.: Photoelectron peak distances at different temperatures for OVs 5.5 V, 4.5 V, and 3.5 V.
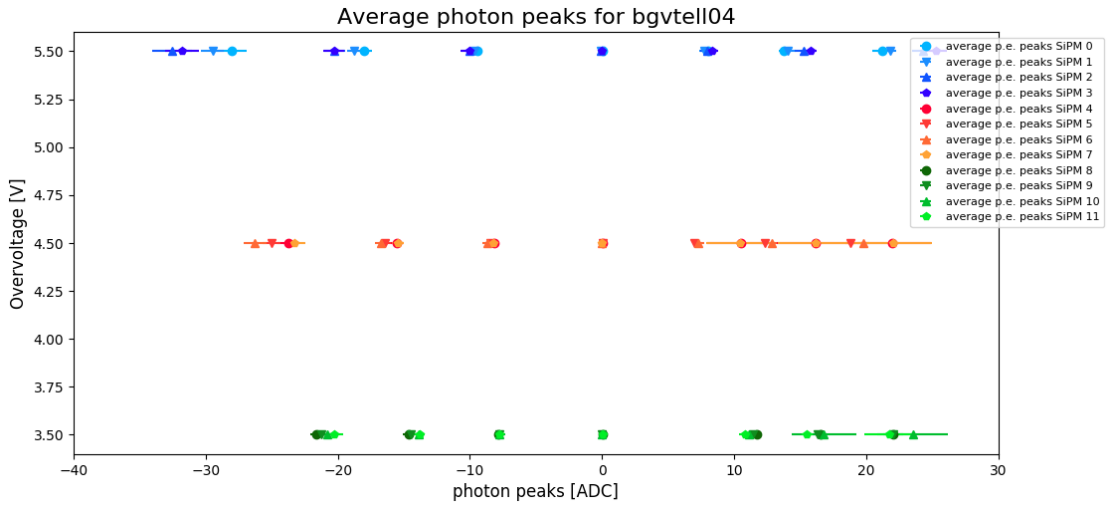
Figure 3.62.: Temperature-averaged photoelectron peak distances at OVs 5.5 V, 4.5 V, and 3.5 V.
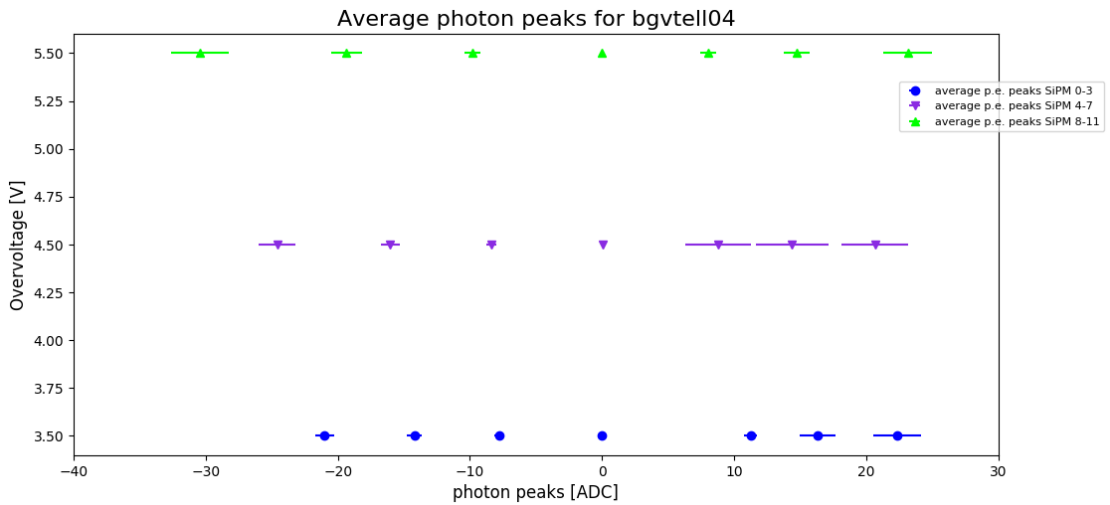
Figure 3.63.: Average PE peaks for all SiPMs at all temperatures in ADC counts at OVs of 5.5 V, 4.5 V, and 3.5 V.

It can be seen that while the distances between the first and second, and second and third photon peak are about the same, there is a larger distance between the pedestal and the first photon peak. This behaviour can be seen in all 3.61 subfigures and is the same for all SiPMs.

One reason for this behaviour could be the analysis approach. Since one histogram was divided by another histogram with a different width around the centre peak, the first photon peak can be smeared and distorted, depending on the noise in the original histograms. Future research could investigate better analysis methods, statistical models or Monte Carlo simulations to verify the given results.

The average distance between the PE peaks is calculated by averaging the differences between 3rd and 2nd, 2nd and 1st, and 1st PE peak and pedestal:

$$\overline{\text{Distance}(OV)} = \sum_{i=0}^{i=2} \left(\overline{\text{PE}_{i+1}(OV)} - \overline{\text{PE}_i(OV)} \right) \cdot \frac{1}{3}. \tag{3.4}$$

The relative errors of the average distances are calculated by summing up the squares of the fractional errors:

$$\sigma^2_{\overline{\text{Distance}(OV)}} = \sum_{i=0}^{i=2} \left(\frac{\sigma_{\text{PE}_i}}{\overline{\text{PE}_i}} \right)^2 + \sigma^2_{\text{pedestal}}. \tag{3.5}$$

The result of this procedure for the upstream top passage module (09-4, bgvtell04) is shown in figure 3.64.

Table 3.3 shows the average photoelectron peak distances per overvoltage and module.

The change of PE distances with overvoltage is not as linear as expected, however, statements about the non-linearity of the PE distances are difficult to make due to the large statistical errors.

The photoelectron distances are linear within the error bars. In addition to the statistical errors, a systematic error can be estimated due to the fact that the binning of the histograms only respects integer numbers and no floats and because the function to find peaks is not perfect either. Thus, an additional systematic error of 1 ADC can be assumed. Since the statistical and systematic error are partially correlated (e.g. the function assumes the peak with an error, causing a larger spread in the statistics), the errors can be added linearly.

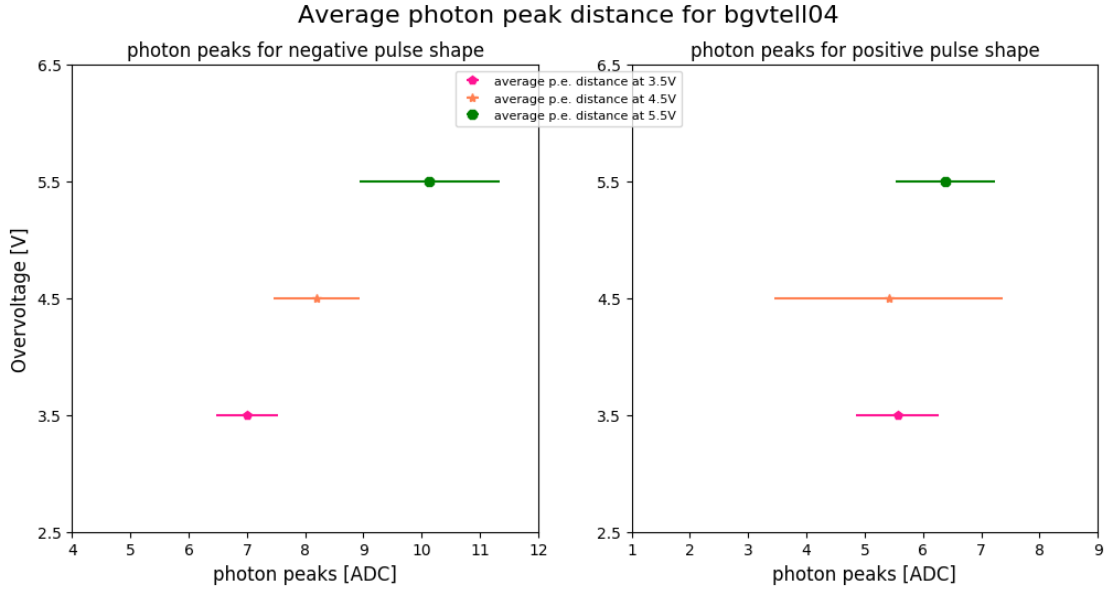The photoelectron peak histograms for all modules are given in appendix A.2.

Figure 3.64.: Average PE distance at OVs of 5.5 V, 4.5 V, and 3.5 V for upstream top passage module (09-4, bgvtell04).

Overvoltage	bgvtell #	average peak distance [ADCs]	standard deviation [ADCs]
5.5 V	bgvtell01	10.132	0.544
	bgvtell02	11.129	0.908
	bgvtell04	10.136	1.208
	bgvtell05	9.643	2.224
	bgvtell06	10.077	0.899
	bgvtell07	10.185	0.705
	bgvtell08	10.111	0.583
	bgvtell09	9.619	1.483
4.5 V	bgvtell01	7.645	0.365
	bgvtell02	8.254	0.887
	bgvtell04	8.196	0.740
	bgvtell05	6.879	1.262
	bgvtell06	8.017	0.985
	bgvtell07	7.685	0.309
	bgvtell08	7.383	0.674
	bgvtell09	8.888	1.730
3.5 V	bgvtell01	6.769	1.400
	bgvtell02	7.052	0.668
	bgvtell04	7.002	0.523
	bgvtell05	6.376	2.282
	bgvtell06	6.842	1.665
	bgvtell07	6.826	1.867
	bgvtell08	7.090	0.656
	bgvtell09	7.301	0.801

Table 3.3.: Parameters for the photoelectron peak data acquisition.

4. Ghost Charges

4.1. Concept and Theory of Ghost Charges

As described in chapter 2, the beams inside the LHC are bunched, and during physics fills, the bunches are spaced by at least 25 ns. The particle bunches in the LHC are accelerated by radio frequency (RF) fields with a base frequency of 400 MHz [3]. One such wave unit is called a "bucket" and is about 2.5 ns or 0.748 m long. In LHC terminology a "bunch slot" refers to 10 RF buckets. There are 35640 RF buckets or 3564 available bunch slots in the LHC.
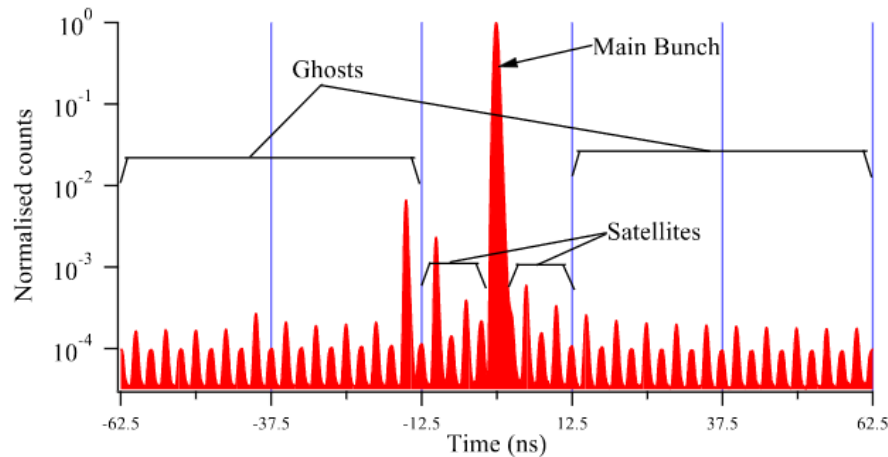
Figure 4.1.: Nominal filled bucket in the centre with satellite charges in neighbouring buckets and ghost charges in neighbouring bunch slots outside the ± 12.5 ns time frame. Source: A. Jeff [48].

In theory, the particles of a nominally filled bunch slot are all in one RF bucket and 9 out of 10 RF buckets are nominally empty. The filled RF bucket is in the centre of the train. However, since the particles inside each bunch don't all have exactly the same energy, position and velocity, some of them diffuse into the neighbouring buckets. In addition, ghost charges and satellites can already be introduced in the LHC from earlier stages of

the injector chain like the PS or SPS.

Other reasons for particles flowing outside the nominal bucket are intra-beam scattering, beam-beam interactions, beam-gas interactions, RF-noise, and others [49].

Charges that are outside the nominal filled bucket but still within the nominal bunch slot are referred to as "satellite charges" or satellites. These charges can still contribute to triggered particle collisions and to the total luminosity that is described in chapter 2.2, however, due to the crossing angles of the beams in the interaction points less of these satellites contribute to the beam-beam interactions.

The diffusing charges can drift even further away from the nominal bucket and outside of the nominal bunch. These charges, located outside the nominally filled bunch slot are called "*ghost charges*". Since they occur in bunch slots that are nominally empty, they cannot contribute to the triggered particle collisions and thus cannot contribute to the total luminosity.

The importance of the ghost charge measurement is motivated by the measurement of the absolute luminosity. As shown in chapter 2.2, equation 2.3, the absolute luminosity measurement is defined by the amount of particles per bunch and the measured beam width.

The total amount of charge in the LHC is measured with the direct charge current transformer. However, since not all particles are in the nominally filled buckets, the amount of charges per bunch N_1, N_2 has to be corrected by the amount of ghost charges measured in the fill. For protons, this correction was about 2.5 % [50] in the fills of 2011-2013.

4.2. Ghost charge measurement

There are currently three methods used at the LHC to measure the charge population of the bunch slots. One method includes the fast bunch current transformer (FBCT), which acquires a pulse proportional to the charge in each bunch slot. There is one FBCT per ring that takes one signal per 25 ns bunch slot. The FBCT measurement is dependent on a threshold and cannot measure charges below the given threshold.

In order to acquire the absolute charge per bunch slot, the FBCT values need to be normalised to the data from the direct charge current transformer, or DCCT. There are 2 DCCTs per ring, which measure the total charge of the respective beam in the LHC. However, they are not time sensitive, which means that there is no bunch-by-bunch charge information from the DCCT.

The sum of all FBCT values per ring multiplied by a norm-factor matches the DCCT

value per ring. This norm-factor allows for the transformation of the relative charge from the FBCT to the absolute charge in the LHC. However, since the FBCT provides the information on the relative bunch charge population, the measured ghost charge cannot be absolute. The DCCT and FBCT are described in detail in [51] and [52].

Another method takes data from the longitudinal density monitor (LDM), which uses synchrotron light to measure the precise longitudinal distribution of the beam charge. There is one LDM per beam installed at the LHC. Data are taken with a time resolution of about 90 ps. This time resolution allows to distinguish between the nominally filled RF bucket and satellites. The measurement of satellites as well as ghost charges represents an advantage to the other methods.

The third method to measure ghost charges is beam gas interaction counting (LHCb BG), which is described in detail in [53]. Unlike the other two methods that are presented above, BGI doesn't measure the charges but uses LHCb's VELO (see section 2.4.2) to acquire interaction vertices between particles from the beams and neon gas that is injected into VELO's vacuum during dedicated fills.
This method makes use of the given injection scheme for each fill and the respective beam crossing types that can occur in an interaction point. There are four distinguished bunch crossing types as shown in table 4.1:

beam1 slot nominally	beam2 slot nominally	bunch crossing (bx) type	bunch crossing name (bx) name
empty	empty	0	ee
filled	empty	1	be
empty	filled	2	eb
filled	filled	3	bb

Table 4.1.: Bunch crossing types in an interaction point.

The first bunch crossing type at an interaction point is defined as one where neither bunch slot for beams $j = 1, 2$ contains particles. The nomenclature for this bunch crossing type is ee.
In the second crossing type either beam 1 ($j = 1$) or beam 2 ($j = 2$) has a nominally filled bunch slot, while the other beam's bunch slot is nominally empty. This is referred to as be or eb.
The last bunch crossing type is relevant for physics experiments where the particles of both beams have to collide in an interaction point. This bunch crossing type is called bb. The ee beam crossing is most common for luminosity calibration fills, since only a few tens of the bunch slots are nominally filled. The counted vertices from ee crossings as well as be/eb crossings are used to derive the relative amount of ghost charges, as described in the next section.

4.3. Luminosity run conditions for 2015

The fills discussed in this thesis are listed in table 4.2. Data were taken during dedicated luminosity calibration fills while the beams where scanned across each other (van der Meer scan (VDM) [54]) in either of the four interaction points at the LHC. The nominal net half crossing angle ϕ_x between the two beams is given for the horizontal plane.

LHCb's RICH system (RICH1 and RICH2) was included during certain fills. As a result, data for these fills were taken without consecutive triggers. The systematic error for ghost charge fractions is calculated differently for fills with consecutive triggers than for fills with non-consecutive triggers, as shown in section 4.4.1.

Fill	month	beam type	energy [TeV]	ϕ_x [μmrad]	β^* IP8[m]	# bunches b1/b2	# collisions in IP8	RICH	VDM in experiment
3850	June	pp	6.5	465	24.09	39/39	15	excl.	LHCb BG
4266	August	pp	6.5	465	24.09	44/44	6	excl.	ATLAS, CMS
4269	August	pp	6.5	465	24.09	51/51	16	excl.	LHCb
4634	November	pp	2.5	564	7.02	44/44	22	incl.	ATLAS, CMS, LHCb
4689	December	PbPb	6.37 Z	400	3.0	426/424	24	incl.	ATLAS, CMS
4690	December	PbPb	6.37 Z	400	3.0	426/424	24	incl.	ALICE
4691	December	PbPb	6.37 Z	400	3.0	474/474	24	incl.	LHCb

Table 4.2.: Luminosity calibration runs in 2015.

4.4. Analysis Procedure

4.4.1. Ghost charge calculation

Data used to derive ghost charge fractions f_{ghost} are taken during dedicated luminosity calibration fills. Beam-gas interaction events were taken as mentioned in section 4.2.

The ghost charge, to first order, is the number of beam1-gas (beam2-gas) interaction vertices from ee crossings (N_{ee}) divided by the number of vertices in be (or eb) crossings in the respective fill.

While this first order approach provides good results, it would be more precise to count for beam1 the interactions $(N_{\mathsf{ee}} + N_{\mathsf{eb}})_{beam1-gas}$. However, since there is only a very small fraction of bunch slots filled during the luminosity calibration fills and the fraction of $(N_{\mathsf{eb}})_{beam1-gas}$ is very small, this value is usually neglected.

The fraction $N_{\mathsf{ee}}/N_{\mathsf{be}}$ has to be normalised to the amount of particles in the eb (be) slots and compared to the full beam population by multiplication with the FBCT intensity normalised to the DCCT intensity $I_{\mathsf{be}}/I_{total}$. The equation for the ghost charges in beam 1 results in

$$f_{ghost,1} = \frac{N_{\mathsf{ee}}}{N_{\mathsf{be}}} \cdot \frac{I_{\mathsf{be}}}{I_{total,1} \cdot \epsilon_{timing\ trigger,1}} \quad . \tag{4.1}$$

A trigger efficiency correction factor $\epsilon_{timing\ trigger}$ is applied to take into account the fact that ghost charges can spread over the bunch slot. As described in section 4.1, the length of one LHC bunch slot is 25 ns. The LHCb trigger setting is optimised for the nominally filled bucket in the centre of the bunch slot, where the vast majority of the beam-beam interactions take place.

The trigger efficiency is not constant over the 25 ns bunch slot but depends on the time difference between the interaction and the detector clock. Since the ghost charge interactions can occur at any time in the bunch slot, the average trigger efficiency is not equal to 1 and ghost charges can also exist at the beginning or end of a slot.

If a beam-gas event occurs in one of these extremes, it has a probability of being counted twice by the detectors due to the signal length given by the VELO. These "double counts" can be determined in the data by searching for two adjacent event numbers and can be corrected for. Events that have no adjacent event numbers are called "single counts".

There are two trigger efficiency values given per beam, one for single counts and one for double counts. The differentiation between single and double counts is relevant for the calculation of systematic errors, as is described in section 4.4.2.

The trigger efficiency was measured in 2013 and is given in table 4.3 [53].

	single counts		double counts	
	beam 1	beam 2	beam 1	beam 2
ϵ_i	0.927	0.859	1.048	0.903
σ_{ϵ_i}	0.02	0.01	0.03	0.01
$\sigma_{\epsilon_i}/\epsilon_i$	0.0216	0.0116	0.0286	0.0111

Table 4.3.: Trigger efficiencies with their respective errors. Here, i is either double (ϵ_d) or single (ϵ_s) counts for beams $j = 1, 2$. Source: C. Barschel [53].

4.4.2. Calculation of systematic errors

While the statistical error is determined by the amount of data that were taken during a luminosity calibration fill, the systematic errors are dominated by the trigger efficiencies $\epsilon_{timing\ trigger}$ for the single or double counts of the ee vertices. The systematic error for double and single count trigger efficiencies ϵ_d and ϵ_s is calculated by multiplying the average single and double ghost charge counts $a_{d,j}$, $a_{s,j}$ by the respective efficiency factors given in table 4.3, and adding the average difference between the trigger efficiency corrected ghost charge counts (δ_{ϵ_j}). The complete equation for the systematic error calculation is

$$\sigma^2_{f_{syst,trig,j}} = (a_{d,j} \cdot \frac{\sigma_{\epsilon_{d,j}}}{\epsilon_{d,j}} + a_{s,j} \cdot \frac{\sigma_{\epsilon_{s,j}}}{\epsilon_{s,j}})^2 + \delta^2_{\epsilon_j}$$

$$\text{with } \delta_{\epsilon_j} = \left| \frac{a_{d,j}}{\epsilon_{d,j}} - \frac{a_{s,j}}{\epsilon_{s,j}} \right| \cdot \frac{1}{2} \quad . \tag{4.2}$$

There are no consecutive triggers when the RICH is included, and thus no double counted ghost charges. As a result, the calculation for the systematic error has to be modified and is estimated directly through the trigger efficiency.

Equation 4.3 shows how the trigger efficiency systematic error is calculated in the case of single count ghost charges only. The values for the trigger efficiencies ϵ and their errors σ_ϵ are again given in table 4.3.

$$\sigma^2_{f_{syst,trig,j}} = (\frac{\epsilon_{d,j} - \epsilon_{s,j}}{2})^2 + \sigma^2_{\epsilon_{d,j}} + \sigma^2_{\epsilon_{s,j}} \tag{4.3}$$

Since the trigger efficiency contribution to the systematic error is fully correlated between the beams, the systematic uncertainties per beam are added linearly,

$$\sigma_{f_{syst,trig}} = \sigma_{f_{syst,trig,1}} + \sigma_{f_{syst,trig,2}} \quad . \tag{4.4}$$

The total uncertainty for the ghost charge fractions for both beams is calculated from $\sigma^2_f = \sigma^2_{f_{syst,trig}} + \sigma^2_{f_{stat}}$.

An additional systematic error must be considered for lead fills, due to the large amount of nominally filled bunch slots. This is further explained in section 4.7.1.

4.5. Ghost charge results for pp fills 3580, 4266, and 4269

The fills 3850, 4266 and 4269 were taken in June and August 2015 respectively. The proton beams had a centre of mass energy of $\sqrt{s} = 13$ TeV.

The LHCb BG data were taken with the RICH (RICH1 and RICH2) excluded, which means that there are consecutive triggers. As a result, the systematic error can be calculated as described in equations 4.2 and 4.4.

The results of ghost charges over time are given in tables A.2, A.3 and A.4 in the appendix. In addition, since the ghost charges remained constant over time, an average of ghost charge fractions per fill is given in table 4.4.

Fill	beam	LHCb Beam Gas				LDM
		GC fractions %	GC rms %	syst. error %	stat. error %	GC fractions %
3850	1	1.37	0.018	0.035	0.003	1.104
	2	1.01	0.020	0.011	0.003	0.802
4266	1	0.13	0.003	0.006	0.001	0.105
	2	0.08	0.031	0.003	0.001	0.062
4269	1	0.09	0.017	0.004	0.002	0.075
	2	0.05	0.015	0.003	0.002	0.034

Table 4.4.: Average ghost charge fractions for fills 3850, 4266 and 4269 from LHCb BG and LDM data.

Figures 4.2, 4.5, and 4.8 show the distribution of the normalised ghost charges (with respect to the FBCT/DCCT intensity) over the 3564 bunch slots in the LHC. The ghost charges are accumulated around the filled bunch slots which are indicated by grey vertical lines. The upper half of the plots show data from the LHCb BG method while the lower half shows the ghost charge distribution measured with the LDM for beam 1 and beam 2 respectively. The statistical errors for the LDM are too small to be visible in the plots.

Figures 4.3, 4.6, and 4.9 show the relation between the LHCb BG and LDM ghost charges per bunch. The data are in good agreement for both beams for fills 3850 and 4266.

For fill 4269, the deviation in beam 2 results from the baseline correction of LDM data (due to a substantial noise contribution) which results in lower ghost charge fractions in general and in a smaller amount of concerned bunch slots in particular.

The baseline correction causes parts of the unbunched charges to be removed as well, hence the LDM results for the three fills are (artificially) lower than for LHCb BG, as can be seen in figures 4.4, 4.7, and 4.10.
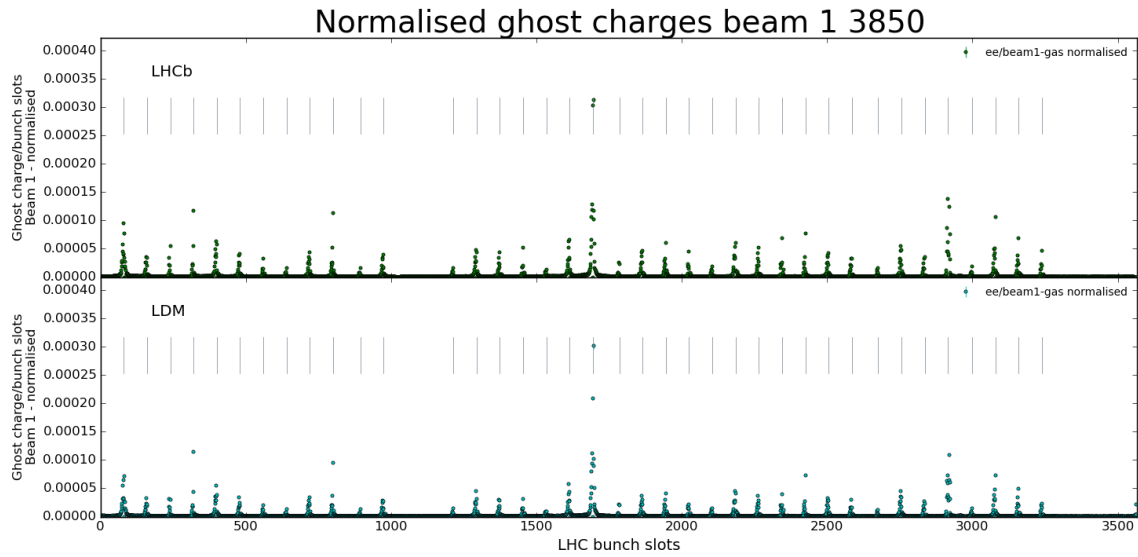
(a) Normalised ghost charge distribution for fill 3850 over the LHC bunch slots for beam 1. The upper plot shows the normalised ghost charge distribution measured by LHCb while the lower plot shows the normalised ghost charge distribution measured with the LDM.
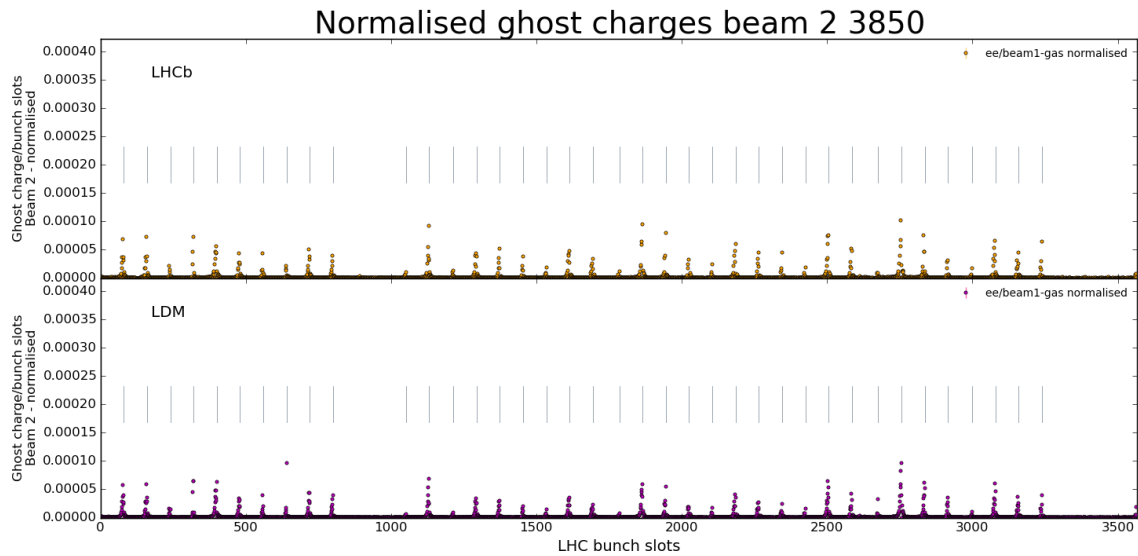
(b) Normalised ghost charge distribution for fill 3850 over the LHC bunch slots for beam 2. The upper plot shows the normalised ghost charge distribution measured by LHCb while the lower plot shows the normalised ghost charge distribution measured with the LDM.

Figure 4.2.: Ghost charge distribution over the LHC bunch slots for beam 1 4.2a and beam 2 4.2b.
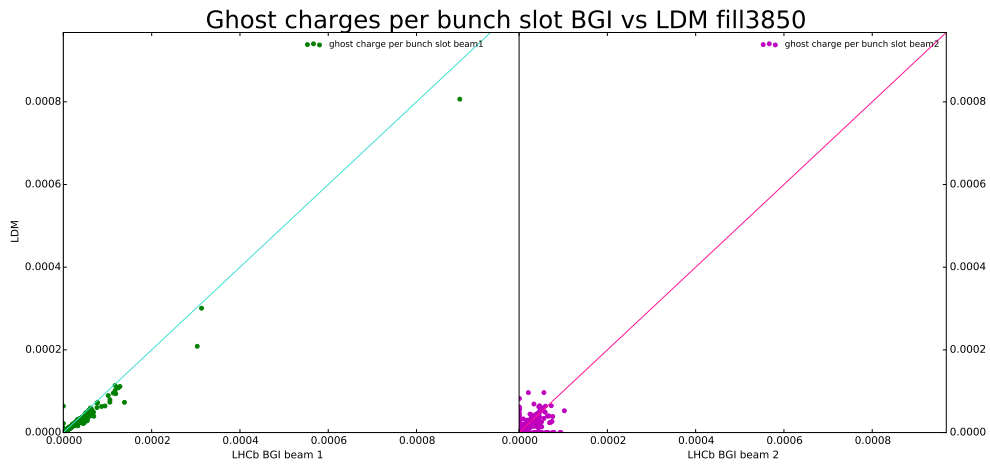
Figure 4.3.: Relation between the LHCb BG and LDM ghost charges per bunch for fill 3850.
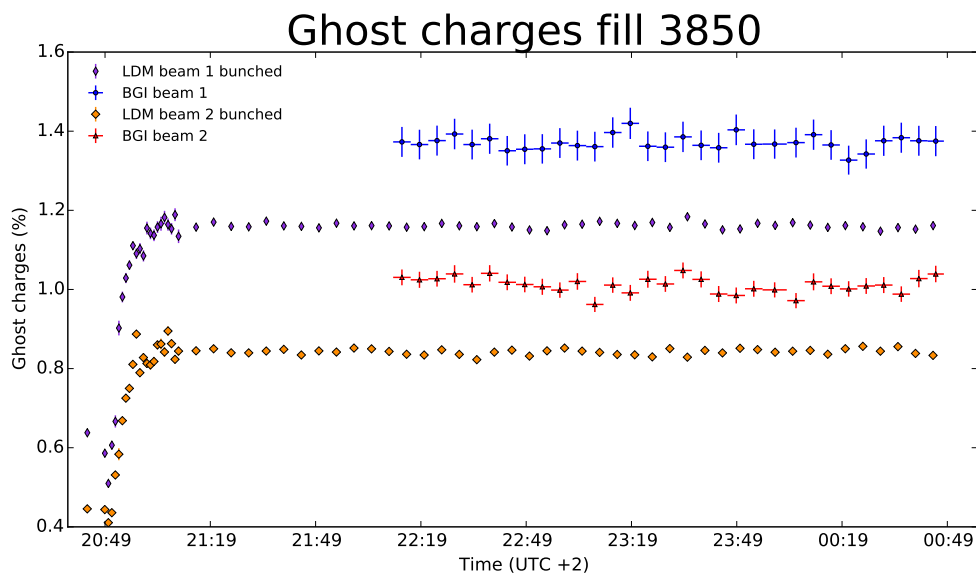
Figure 4.4.: Ghost charge fractions over time for fill 3850. The ghost charge fractions over time are given in table A.2.
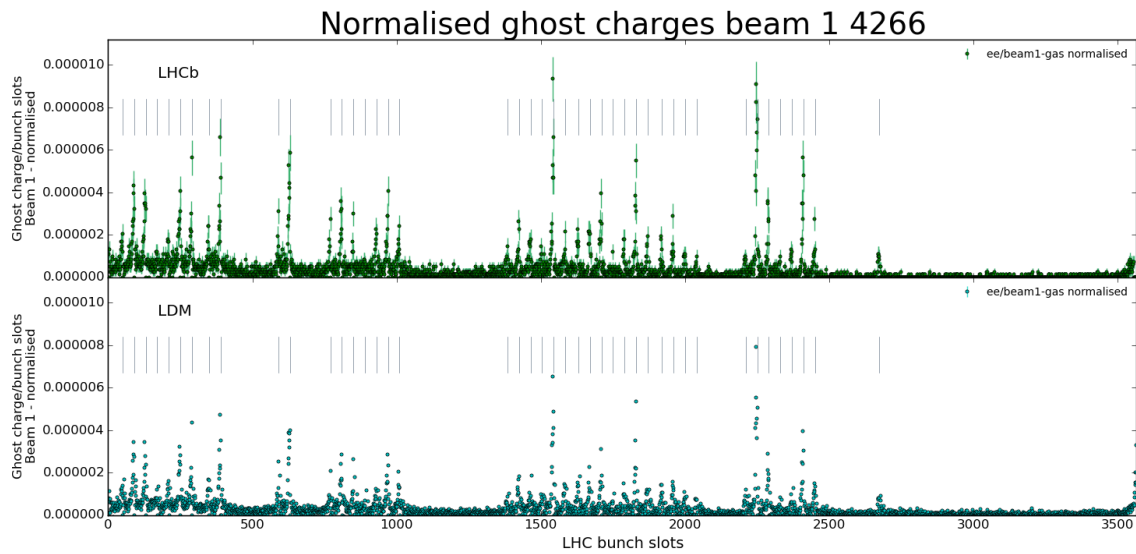
(a) Normalised ghost charge distribution for fill 4266 over the LHC bunch slots for beam 1. The upper plot shows the normalised ghost charge distribution measured by LHCb while the lower plot shows the normalised ghost charge distribution measured with the LDM.
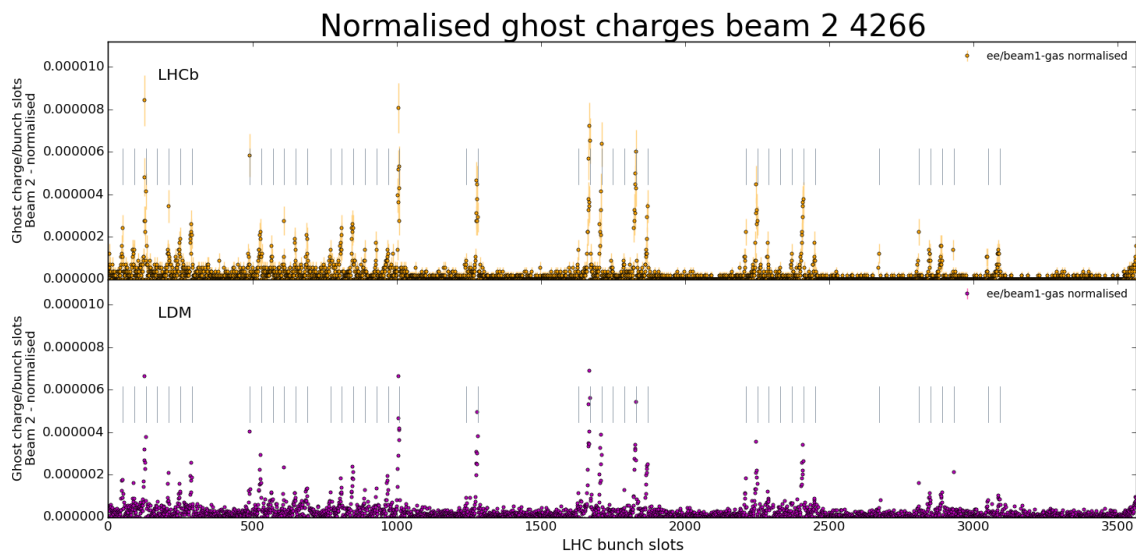
(b) Normalised ghost charge distribution for fill 4266 over the LHC bunch slots for beam 2. The upper plot shows the normalised ghost charge distribution measured by LHCb while the lower plot shows the normalised ghost charge distribution measured with the LDM.

Figure 4.5.: Ghost charge distribution over the LHC bunch slots for beam 1 4.5a and beam 2 4.5b.
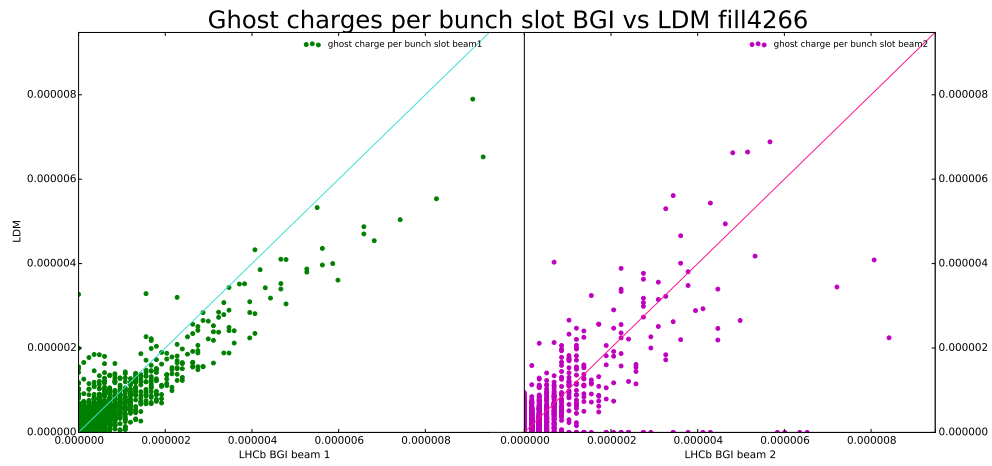
Figure 4.6.: Relation between the LHCb BG and LDM ghost charges per bunch for fill 4266.
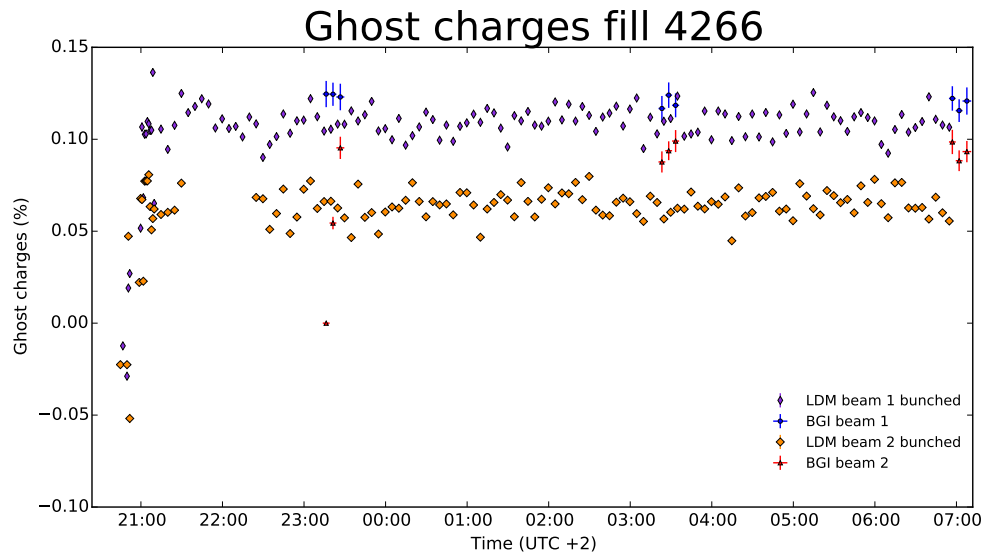
Figure 4.7.: Ghost charge fractions over time for fill 4266. The ghost charge fractions over time are given in table A.3.
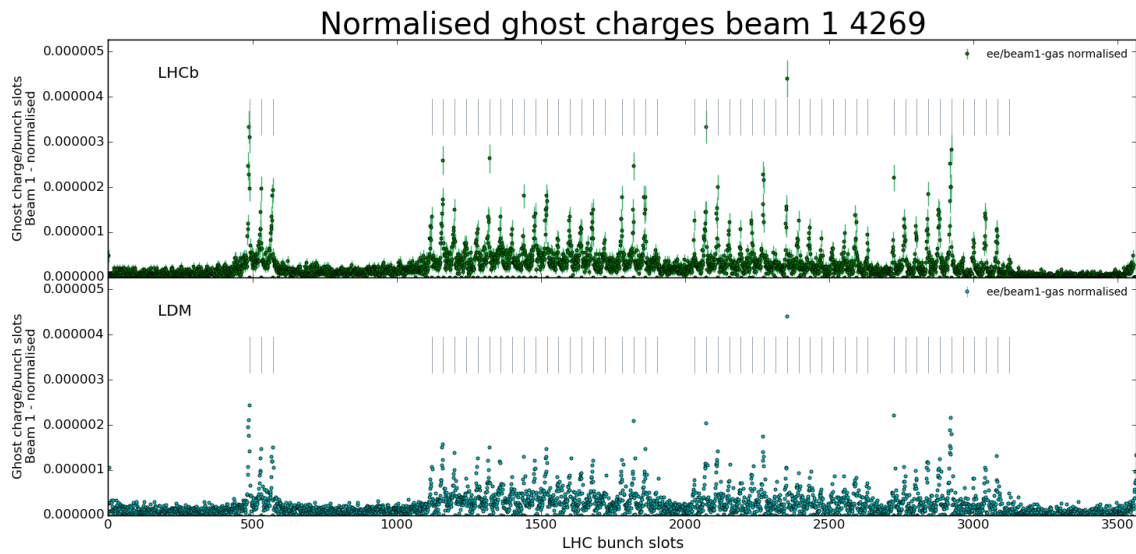
(a) Normalised ghost charge distribution for fill 4269 over the LHC bunch slots for beam 1. The upper plot shows the normalised ghost charge distribution measured by LHCb while the lower plot shows the normalised ghost charge distribution measured with the LDM.
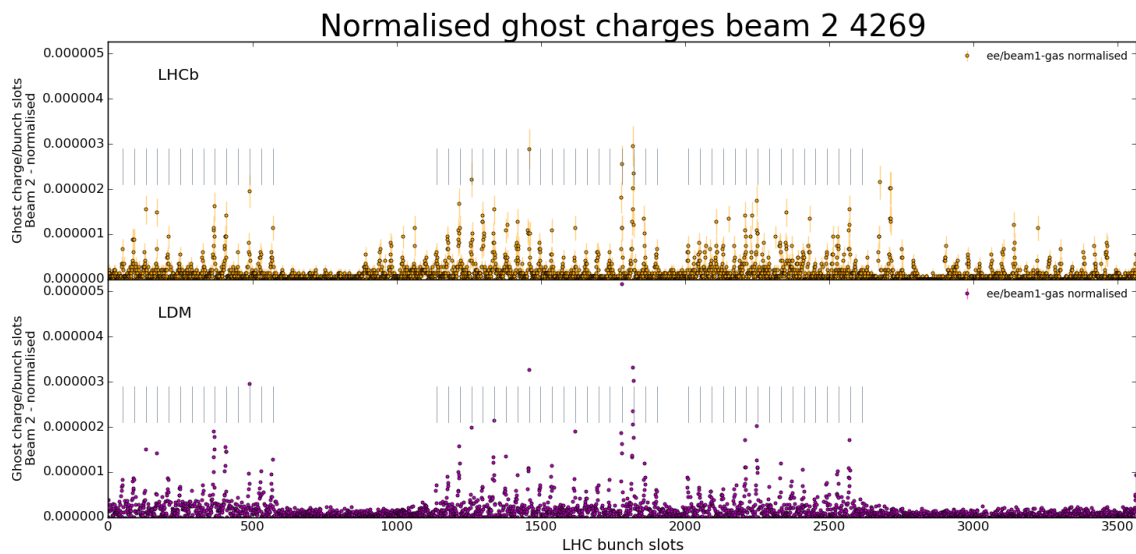
(b) Normalised ghost charge distribution for fill 4269 over the LHC bunch slots for beam 2. The upper plot shows the normalised ghost charge distribution measured by LHCb while the lower plot shows the normalised ghost charge distribution measured with the LDM.

Figure 4.8.: Ghost charge distribution over the LHC bunch slots for beam 1 4.8a and beam 2 4.8b.
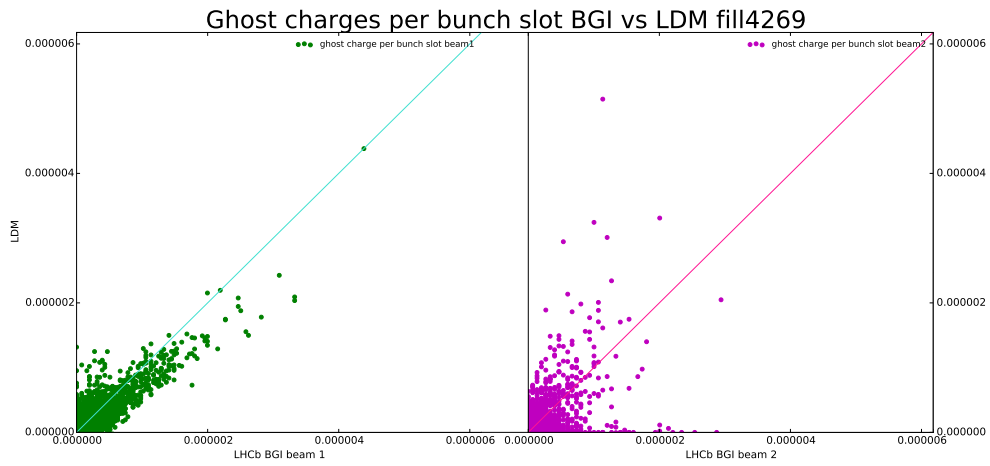
Figure 4.9.: Relation between the LHCb BG and LDM ghost charges per bunch for fill 4269.
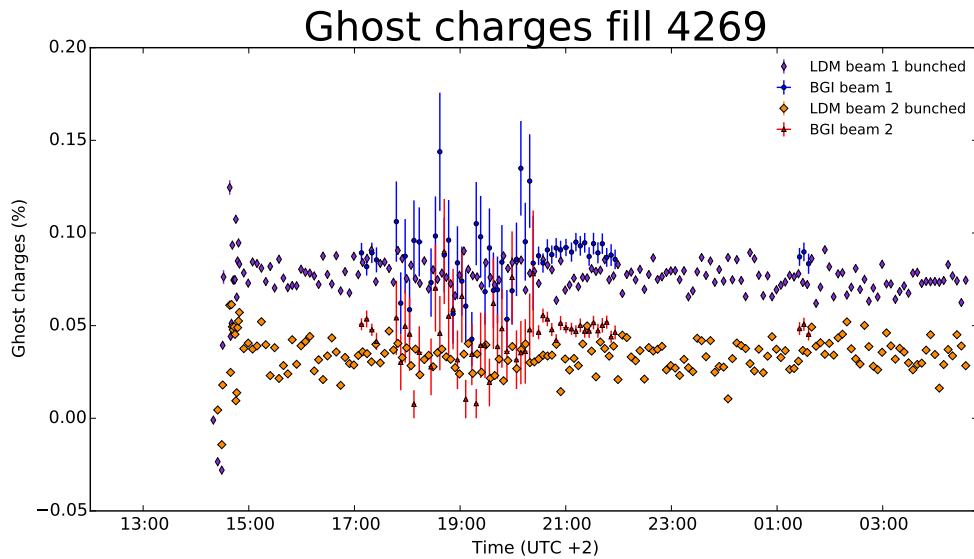
Figure 4.10.: Ghost charge fractions over time for fill 4269. The ghost charge fractions over time are given in table A.4.

4.6. Ghost charge results for intermediate energy pp fill 4634
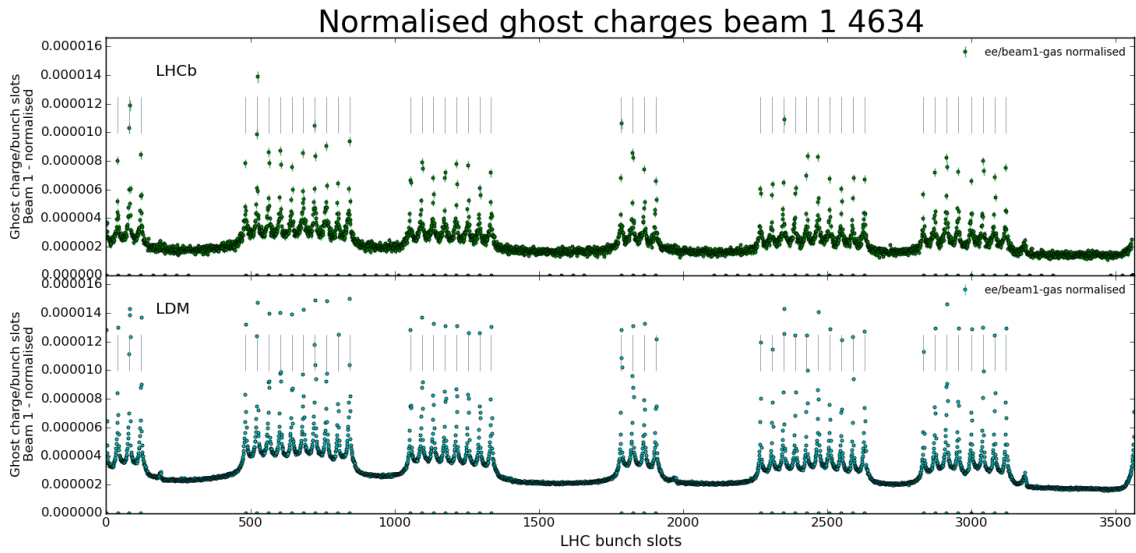
(a) Normalised ghost charge distribution for fill 4634 over the LHC bunch slots for beam 1. The upper plot shows the normalised ghost charge distribution measured by LHCb while the lower plot shows the normalised ghost charge distribution measured with the LDM.
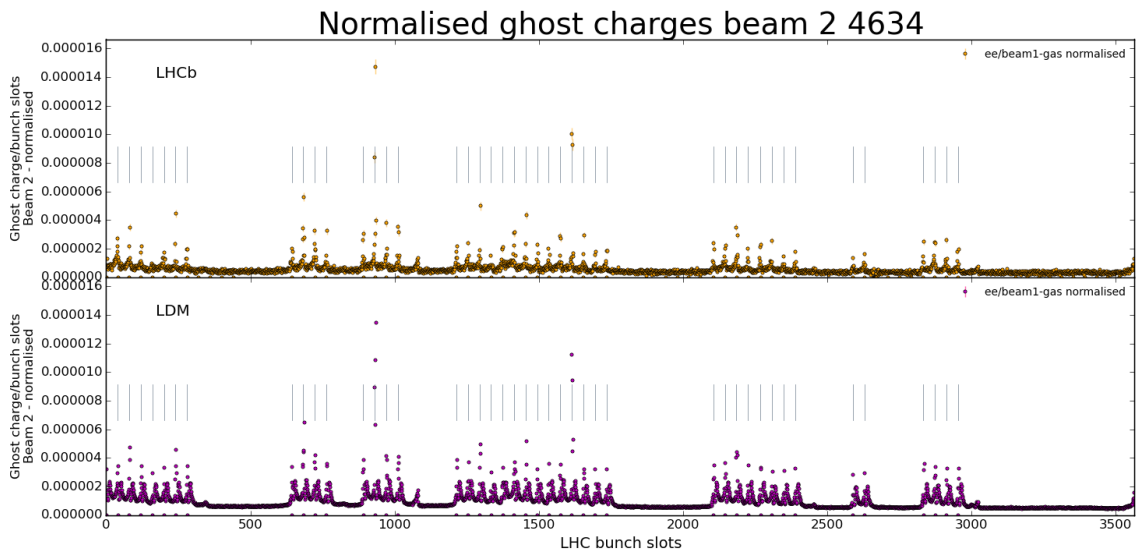
(b) Normalised ghost charge distribution for fill 4634 over the LHC bunch slots for beam 2. The upper plot shows the normalised ghost charge distribution measured by LHCb while the lower plot shows the normalised ghost charge distribution measured with the LDM.

Figure 4.11.: Ghost charge distribution over the LHC bunch slots for beam 1 4.11a and beam 2 4.11b.
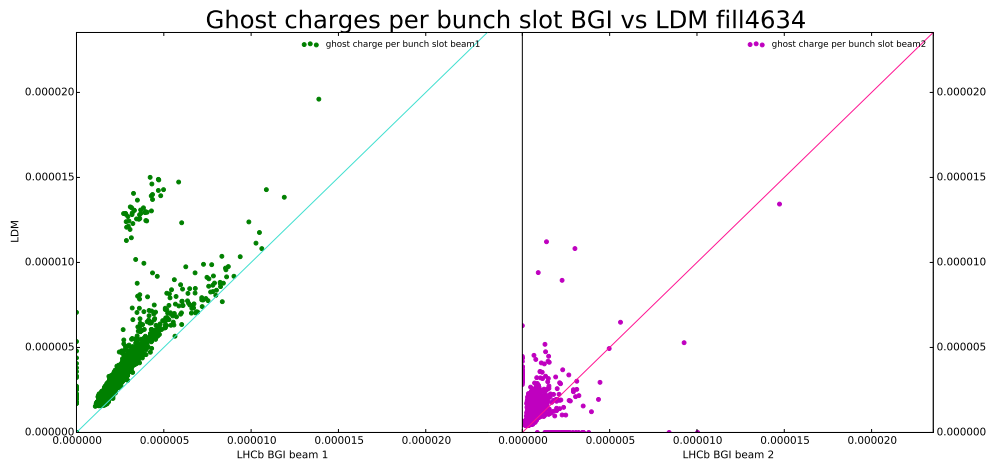
Figure 4.12.: Relation between the LHCb BG and LDM ghost charges per bunch for fill 4634.
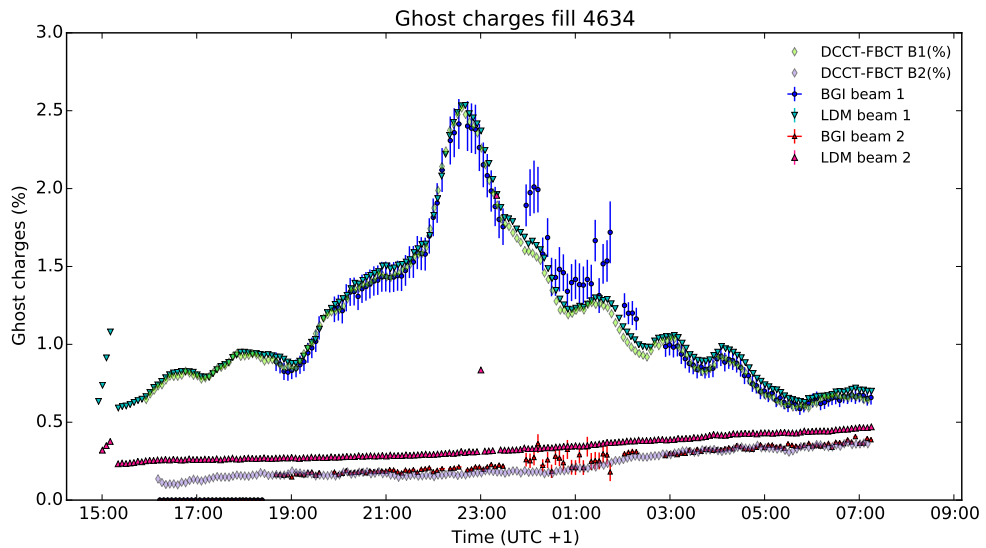
Figure 4.13.: Ghost charge fractions over time for fill 4634. The ghost charges for beam 1 increase and decrease again during the fill. In addition, data from the FBCT and DCCT is plotted and given in table A.5.

Fill 4634 was taken in November 2015. The beams had a centre of mass energy of $\sqrt{s} = 2.5$ TeV. The results of the ghost charge evolution can be found in the appendix in table A.5. For the time spans where LHCb BG data are not available, the DCCT/FBCT data are provided. The DCCT/FBCT data are normalised to the first ghost charge value per beam, taken from LHCb BG data.

Figures 4.11 as well as 4.12 show the agreement between LHCb BG and LDM data per LHC bunch slot while the time evolution of the ghost charges in figure 4.13 shows the ghost charge fractions in the whole LHC at any given time during the fill.

As can be seen from figure 4.13, the ghost charge in beam 1 increased and decreased during the fill. After discussing with RF experts from the beams department[1], several reasons for the behaviour of the ghost charges of beam 1 in this fill could be identified:
The LHC's RF system was not set up for protons but for a low-intensity ion run, so the beam settings were not optimal. In addition, the controlled longitudinal emittance blow-up [55], a tool that stabilises the bunches of the beam, was disabled. This caused shorter bunch lengths and thus reduced the longitudinal stability of the bunches. As a result, the charges drifted out of the nominal bunch slot, causing the measured increase in ghost charges.
The bunch length increased over the fill time and became stable, which resulted in a decrease of the ghost charges seen in beam 1.
The described effects are not visible in beam 2 because the RF noise is about 10 dB lower than for beam 1. The beam 2 ghost charge increases slightly over the whole fill, similar to what is observed in other proton fills.

Since the RICH was included during the fill and no consecutive triggers were allowed, the systematic error is given by the trigger efficiency, as described in equation 4.3 and results in the relative uncertainties $\sigma_{f_{syst,trig,1}} = 0.0704$ for beam 1 and $\sigma_{f_{syst,trig,2}} = 0.0262$ for beam 2. Again, the trigger contribution is fully correlated between the beams, therefore the systematic uncertainty per beam is added linearly.

---

[1]E. Chapochnikova, H. Timko, J. E. Muller

4.7. Ghost charge results for PbPb runs 4689, 4690, and 4691

4.7.1. Additional systematic errors - Lead fills

As mentioned in section 4.4.1, an additional systematic error for lead fills has to be considered. The reason for this is that the standard procedure to measure ghost charge fractions only uses ee beam crossings in the numerator and ignores be or eb crossings (which are only used in the denominator), see equation 4.1.

While this method is sufficiently accurate for fills where only a few bunch slots are nominally filled and the ghost charge is known to accumulate predominantly near the filled bunches of the given beam, this is not accurate for fills with a large number of nominal bunches or a larger dispersion of the ghost charges around the ring.

The two mentioned conditions are not met for the Pb fills (4689, 4690, 4691), where a considerable fraction of bunch slots (400 to 500) was filled. This results in a significant increase of be and eb crossings which, by the standard analysis procedure, are not taken into account for the ghost charge event counting, while there can be beam 1 (beam 2) ghost charge in the empty slots of a eb (be) crossing.

The data taken for fills 4689, 4690 and 4691 do not allow for measuring this contribution from actual eb (be) vertices, due to z-cuts applied in the HLT beam-gas lines. Instead, a correction is applied based on the assumption that the ghost charge is homogeneously distributed over all empty slots, as supported by the data, see figures 4.14, 4.17 and 4.20. The correction factor c_j for beam $j = 1, 2$ is estimated as

$$beam\,1:\, c_1 = \frac{3564 - n_{\mathsf{bb}} - n_{\mathsf{be}}}{3564 - n_{\mathsf{bb}} - n_{\mathsf{be}} - n_{\mathsf{eb}}},$$

$$beam\,2:\, c_2 = \frac{3564 - n_{\mathsf{bb}} - n_{\mathsf{eb}}}{3564 - n_{\mathsf{bb}} - n_{\mathsf{be}} - n_{\mathsf{eb}}}\,.$$

(4.5)

Here n_x is the number of bunch slots of crossing type $x =$ bb, be, eb at Point 8. For example for fill 4689, this correction results in

$$beam\,1:\, c_1 = \frac{3564 - 24 - 426}{3564 - 24 - 426 - 424} = 1.1576,$$

$$beam\,2:\, c_2 = \frac{3564 - 24 - 424}{3564 - 24 - 426 - 424} = 1.1584\,.$$

(4.6)

The correction factors c_j for each of the 2015 Pb-fills are given in table 4.5.

Fill	beam 1	beam 2
4689	1.1576	1.1584
4690	1.1576	1.1584
4691	1.1829	1.1829

Table 4.5.: Correction factors c_j for the PbPb fills.

The ghost charge fraction $f_{ghost,j}$ from equation 4.1 is multiplied by the correction factor c_j to obtain a corrected ghost charge:

$$f_{ghost,j}^{corr} = c_j \cdot f_{ghost,j} \ . \tag{4.7}$$

The corrected results $f_{ghost,j}^{corr}$ are presented in tables A.6, A.7 and A.8.

A (conservative) systematic uncertainty due to this correction is assigned, which covers the range $\pm c_j$: $\sigma_{f_{syst, \ corr, \ j}} = \pm \left| 1 - c_j \right|$. The total systematic uncertainty $\sigma_{f_{syst,j}}$ results from the trigger efficiency contribution $\sigma_{f_{syst,trig,j}}$, which is described in equation 4.4, and the correction factor contribution. Since these two values are not correlated, they are added in quadrature: $\sigma_{f_{syst, \ j}}^2 = \sigma_{f_{syst, \ corr, \ j}}^2 + \sigma_{f_{syst, \ trig, \ j}}^2$.
Unlike the trigger efficiency, which is correlated between the beams, the correction factor is not considered correlated between the beams, thus the results per beam are added in quadrature.

The LHCb BG data for fills 4689, 4690, and 4691 were taken with the RICH included, which does not allow for consecutive triggers. This means that there can be no double counts for these fills, so the systematic error from the trigger efficiency contribution has to be calculated using equation 4.3.
Taking the trigger efficiencies given in table 4.3 into account, the trigger efficiency systematic error results in $\sigma_{f_{syst,trig,1}} = 0.0704$ for beam 1 and $\sigma_{f_{syst,trig,2}} = 0.0262$ for beam 2.

The systematic uncertainty including the trigger efficiency and correction factors c_j for both beams is calculated as shown in equation 4.8.

$$\sigma_{f_{syst}}^2 = (\sigma_{f_{syst,trig,1}} + \sigma_{f_{syst,trig,2}})^2 + \sigma_{c_1}^2 + \sigma_{c_2}^2 \tag{4.8}$$

The results for the systematic errors for both beams combined are shown in table 4.6 for fills 4689, 4690 and 4691 respectively. The systematic uncertainty is a relative uncertainty. Since the systematic and statistic error are not correlated, the errors can be added in quadrature.

Fill	$\sigma_{f_{syst}}$
4689	0.243
4690	0.243
4691	0.276

Table 4.6.: Systematic error of both beam 1 and beam 2 combined per fill including trigger efficiency and correction factors.

4.7.2. Fill 4689

The distribution of ghost charges is shown in figure 4.14, where the normalised ghost charges of beam 1 (top) and beam 2 (bottom) as measured with LHCb BG and LDM are plotted against the 3564 bunch slots of the LHC. The LHCb BG data contains the counted ghost charge events per bunch slot, multiplied by the FBCT-DCCT data to normalise it to the total charge in the LHC. The LDM data represents the baseline corrected population of the bunch slots. The ghost charges for beam 1 and beam 2 are more strongly spread over the 3654 bunch slots and do not only accumulate close to the filled bunch slots as compared to the proton fills.
The correlation between the LHCb BG and LDM ghost charge data per bunch slot is shown in figure 4.15. The data are in good agreement for both beams.

Figure 4.16 displays the total ghost charge evolution over the fill time. The ghost charges are underestimated for LHCb BG and corrected through the procedure discussed in 4.7.1. An increase of ghost charge over time is expected and stronger than for proton fills.

The behaviour of the ghost charges for fills 4690 and 4691 is similar to fill 4689 and their plots are given in the next two subsections.
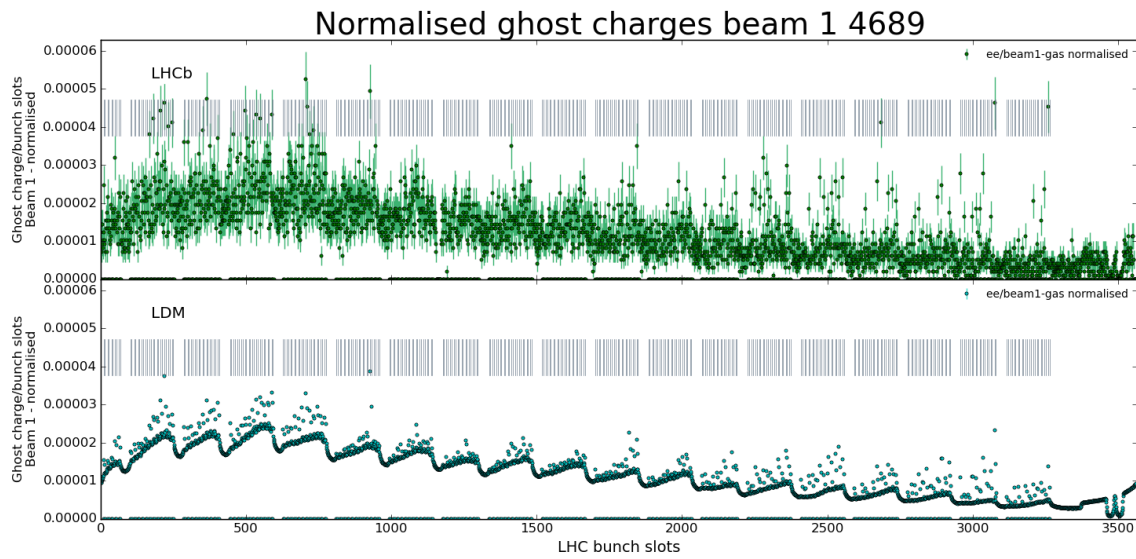
(a) Normalised ghost charge distribution for fill 4689 over the LHC bunch slots for beam 1. The upper plot shows the normalised ghost charge distribution measured by LHCb while the lower plot shows the normalised ghost charge distribution measured with the LDM.
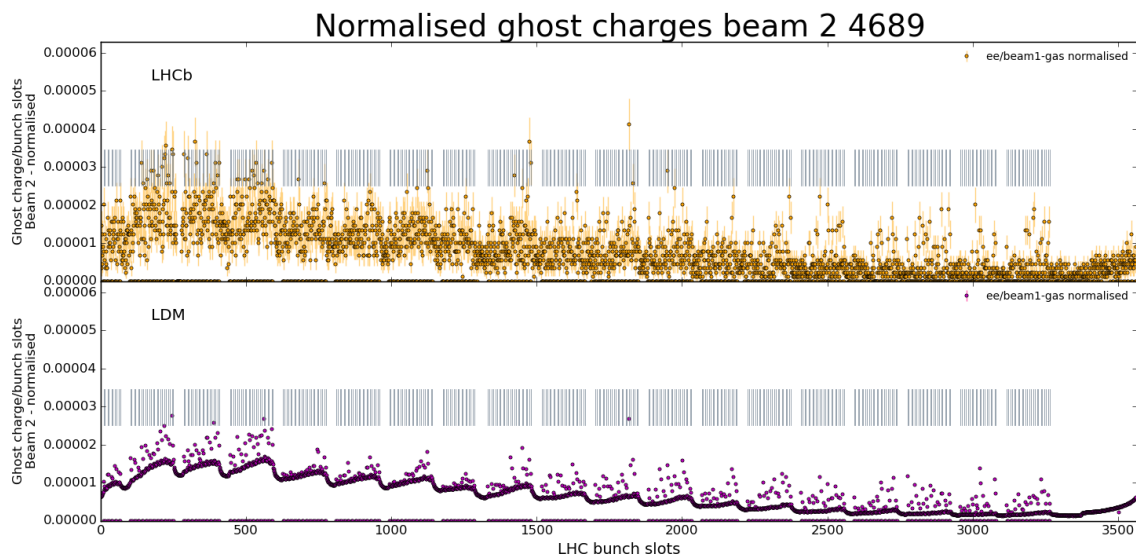
(b) Normalised ghost charge distribution for fill 4689 over the LHC bunch slots for beam 2. The upper plot shows the normalised ghost charge distribution measured by LHCb while the lower plot shows the normalised ghost charge distribution measured with the LDM.

Figure 4.14.: Ghost charge distribution over the LHC bunch slots for beam 1 4.14a and beam 2 4.14b.
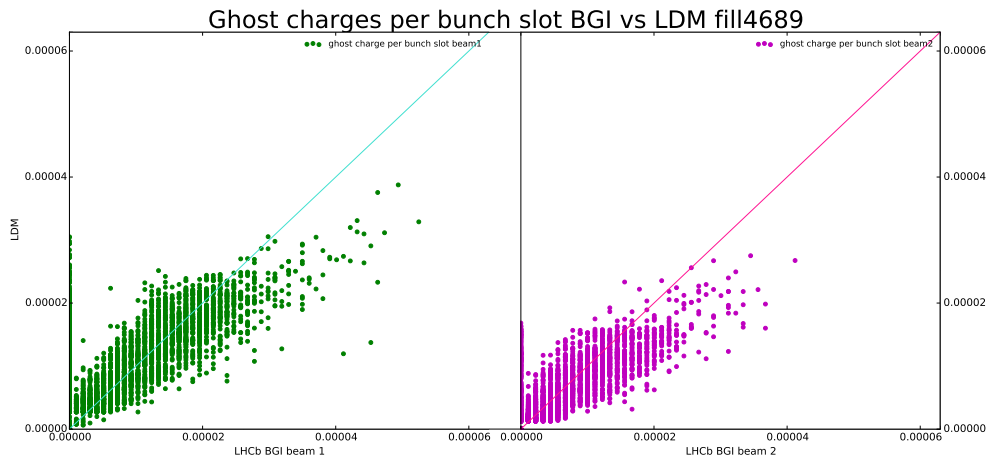
Figure 4.15.: Relation between the LHCb BG and LDM ghost charges per bunch for fill 4689.
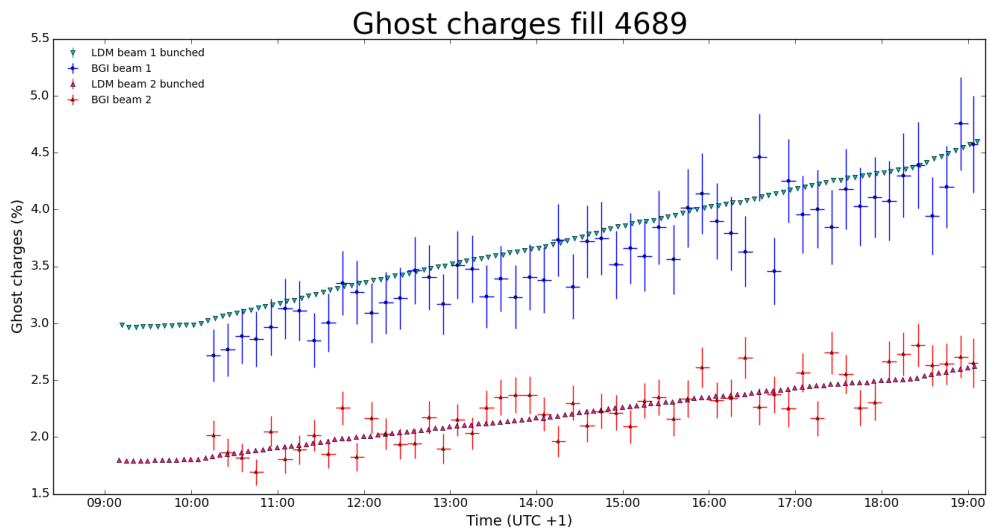
Figure 4.16.: Ghost charge fractions over time for fill 4689.

4.7.3. Fill 4690
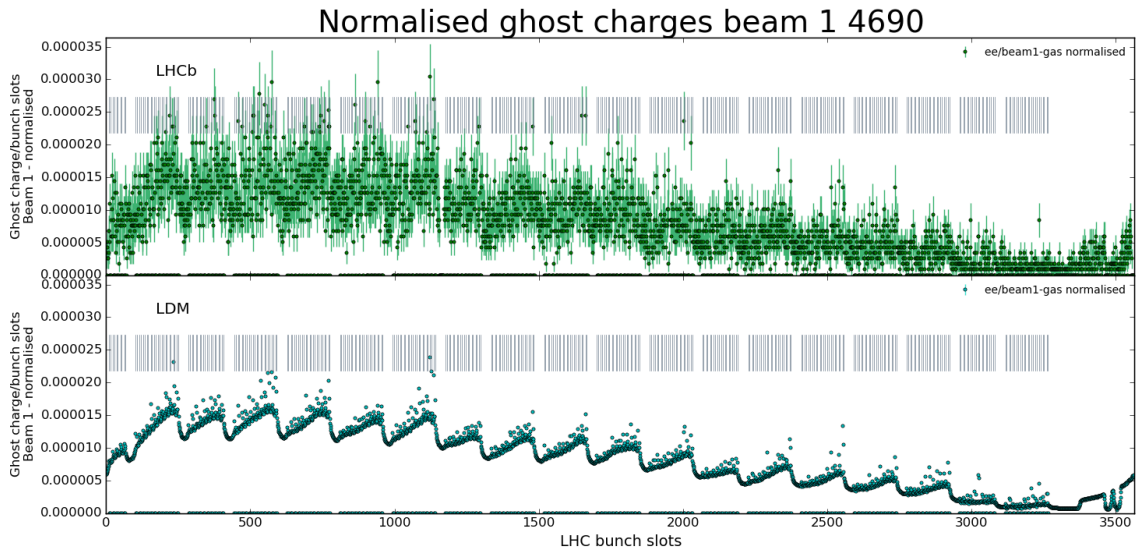
(a) Normalised ghost charge distribution for fill 4690 over the LHC bunch slots for beam 1. The upper plot shows the normalised ghost charge distribution measured by LHCb while the lower plot shows the normalised ghost charge distribution measured with the LDM.
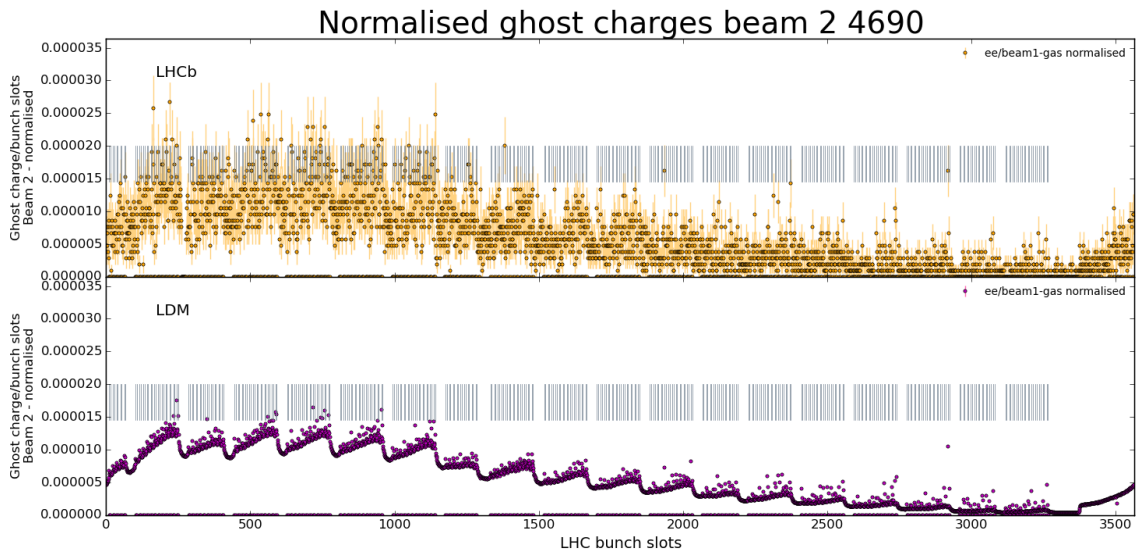
(b) Normalised ghost charge distribution for fill 4690 over the LHC bunch slots for beam 2. The upper plot shows the normalised ghost charge distribution measured by LHCb while the lower plot shows the normalised ghost charge distribution measured with the LDM.

Figure 4.17.: Ghost charge distribution over the LHC bunch slots for beam 1 4.17a and beam 2 4.17b.
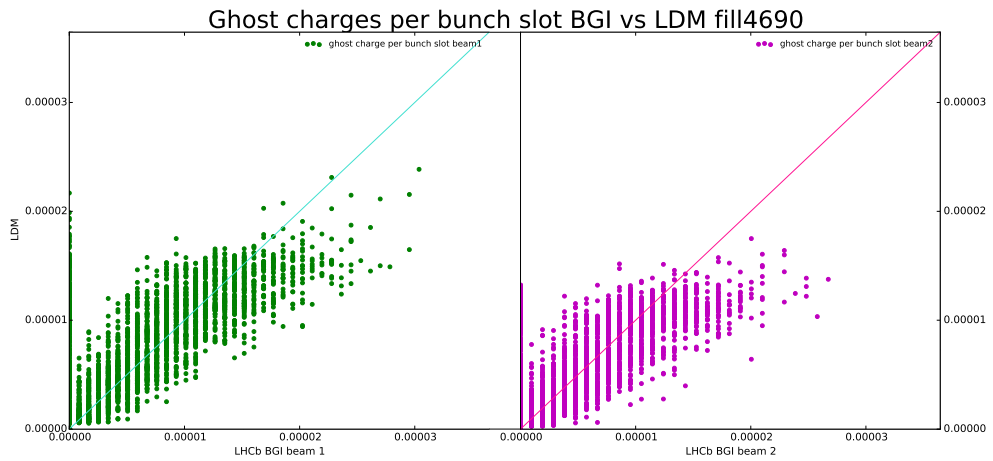
Figure 4.18.: Relation between the BGI and LDM ghost charges per bunch for fill 4690.
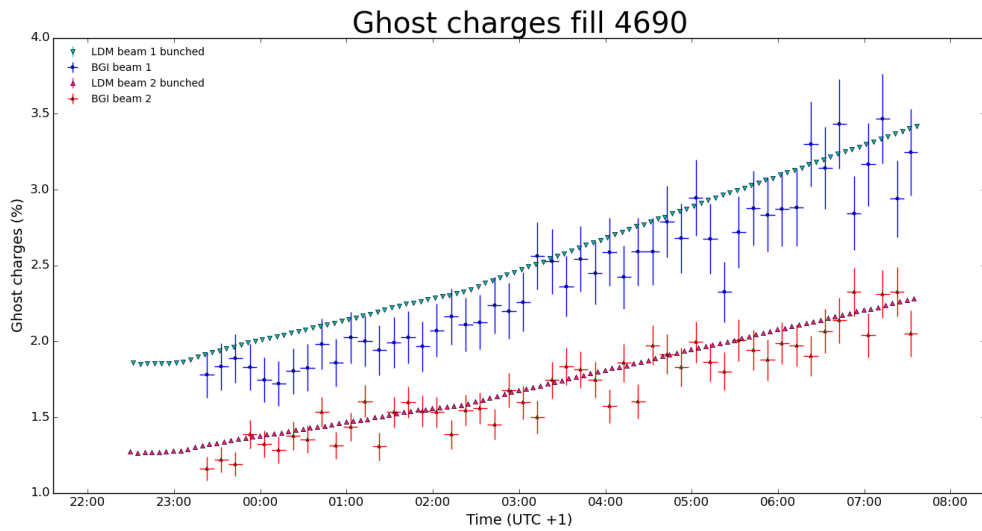
Figure 4.19.: Ghost charge fractions over time for fill 4690.

4.7.4. Fill 4691
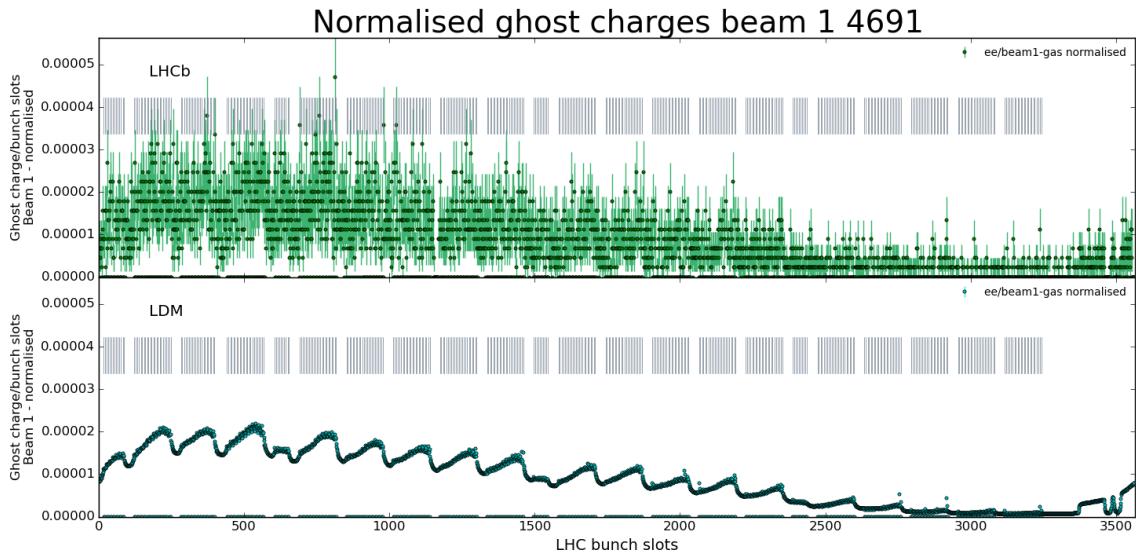
(a) Normalised ghost charge distribution for fill 4691 over the LHC bunch slots for beam 1. The upper plot shows the normalised ghost charge distribution measured by LHCb while the lower plot shows the normalised ghost charge distribution measured with the LDM.
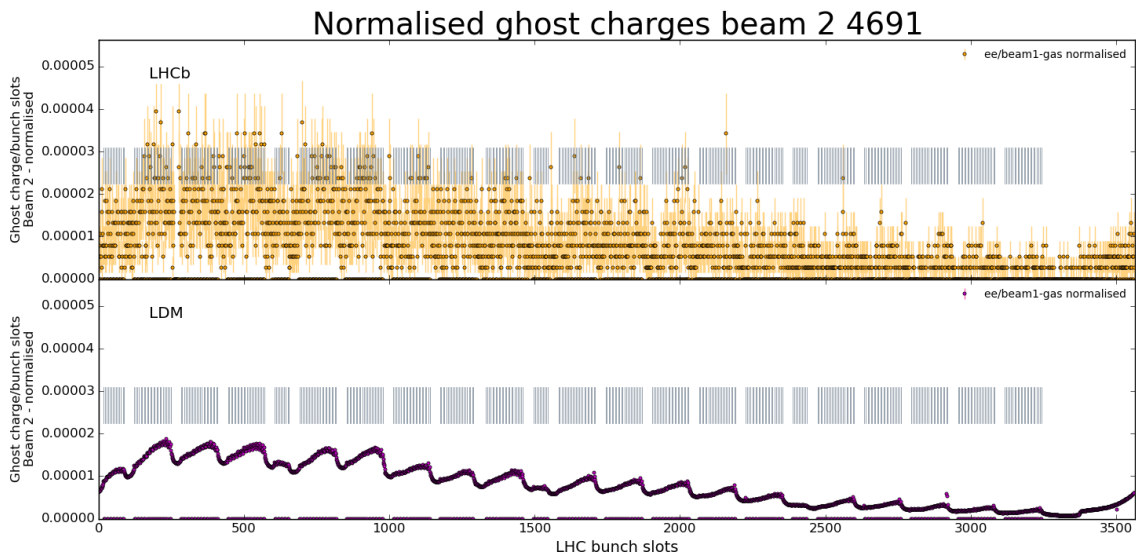
(b) Normalised ghost charge distribution for fill 4691 over the LHC bunch slots for beam 2. The upper plot shows the normalised ghost charge distribution measured by LHCb while the lower plot shows the normalised ghost charge distribution measured with the LDM.

Figure 4.20.: Ghost charge distribution over the LHC bunch slots for beam 1 4.20a and beam 2 4.20b.
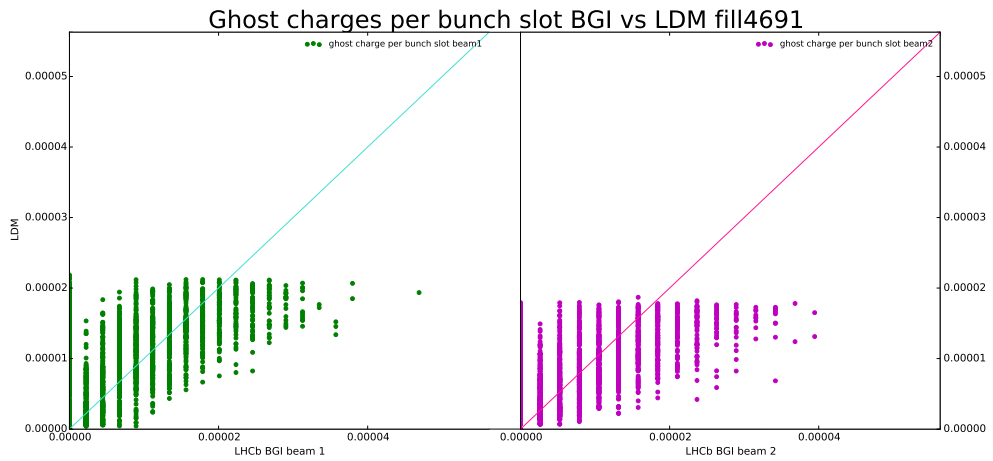
Figure 4.21.: Relation between the BGI and LDM ghost charges per bunch for fill 4691.
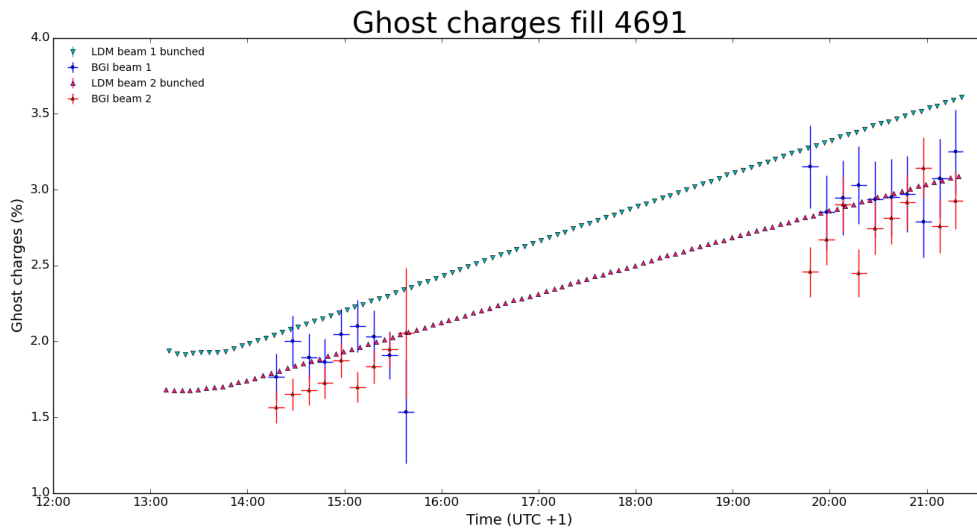
Figure 4.22.: Ghost charge fractions over time for fill 4691.

5. Summary and outlook

A novel beam profile monitor was successfully installed at LHC's Point 4 to measure the transverse beam profile of beam 2. The method to monitor the beam profile is based on a method that was premiered at LHCb in 2012. Hereby, protons from the beam interact inelastically with injected neon gas (at a pressure of up to $2.5 \cdot 10^{-8}$ mbar). The beam-gas vertex detector (BGV) measures the tracks from the particles that were produced in these interactions in two tracking detector stations. These tracks allow to derive the vertices of the interactions. The ensemble of vertices is used to derive the transverse beam profile.

A detector control and data acquisition was set up, using components from LHCb's VELO system and implementing adjustments for the BGV. The system is compatible with the CERN-wide experiment control and can be used by LHC's beam engineering team to monitor the beam.

One major aspect of commissioning was the study of timing parameters to ensure data quality. The ideal timing was measured for each hardware component and implemented in the system.

In addition, a pulse-height spectrum was acquired for the complete detector. The results of these studies can be used to set thresholds for further data acquisition.

The BGV team has taken beam-gas data during the last year to implement track and vertex reconstruction and to further improve the data acquisition parameters. Data from these campaigns are currently analysed offline.
To increase the processing speed and enable "online" data analysis, several parameters have to be implemented in the TELL1 boards. These parameters include zero-suppression, pedestal subtraction, header correction, channel reordering, Mean Common Mode Suppression (MCMS), and clustering.
The BGV team is currently working on an online tool to make the transverse beam profile available for the LHC beam group to monitor the beam width in real time.

Further future applications of the BGV are measurement of ghost charges, relative bunch populations, or tilt of the beam. With an additional, faster trigger, it could also be possible to measure the longitudinal beam profile.

Luminosity calibration runs were performed in 2015 by the four experiments at different energies and with different particles. The results of these luminosity calibration runs can be found in [56] and [57] for the ALICE and CMS experiment respectively.

The ghost charges were measured with two different methods, the LHCb beam-gas method, which was developed and premiered at LHCb in 2012, and the longitudinal density monitors (one per beam). The GC results from the LHCb BG and LDM method are in good agreement for all evaluated fills.

Due to the baseline correction of LDM data, the GC results for the $\sqrt{s} = 13$ TeV runs are artificially lower than from the LHCb BG.

The beam 1 GC evolution of the intermediate energy ($\sqrt{s} = 2.5$ TeV) can be explained by a non-ideal setup of the beams and a generally higher RF-noise for beam 1 compared to beam 2.

The GC results in lead ion runs show that the ghost charges are spread more strongly over the bunch slots and increase more strongly over time than in proton runs. This different GC behaviour can be explained by intra-beam scattering, which is introduced at injection into the LHC and increases over the duration of the fill [58].

A. Appendices

A.1. Phase Delay results

The cable delay is set to $delay_{cable} = 29$ for all modules. One unit of cable delay equals 25 ns. The cycle delay is zero for all 64 links in all 8 modules respectively. The cycle delay enables a 25 ns delay per unit for any individual link.

The phase delay per link, resulting from the data and analysis described in section 3.5.4 is given in table A.1.

	module	Tell1	a-link							phase delay								
	Top QRL 10-4L	bgvtell09	link 0-15	3	3	3	1	1	3	3	1	3	2	1	2	3	3	2	0
			link 16-31	1	1	1	0	1	3	1	1	3	0	0	0	2	3	1	0
			link 32-47	2	1	1	0	1	3	2	1	3	1	1	1	3	3	2	0
			link 48-63	1	1	1	0	1	3	2	1	3	2	1	1	3	3	2	0
	Bottom Path 08-4L	bgvtell06	link 0-15	5	5	5	4	4	5	4	4	5	4	4	4	7	5	5	3
			link 16-31	4	3	4	3	3	4	3	3	4	3	3	3	4	4	4	2
			link 32-47	4	4	4	3	3	4	3	3	4	3	3	3	4	4	4	3
			link 48-63	3	3	3	3	2	4	3	3	4	3	2	3	4	4	3	2
upstream	Bottom QRL 07-4L	bgvtell05	link 0-15	3	3	4	3	3	4	3	3	4	3	3	3	4	4	3	2
			link 16-31	3	3	3	2	3	4	3	3	4	3	2	3	4	4	3	1
			link 32-47	5	4	5	4	4	5	4	4	6	4	4	4	6	5	5	3
			link 48-63	3	3	3	1	2	4	3	3	4	3	2	3	4	4	3	1
	Top Path 09-4L	bgvtell04	link 0-15	3	4	1	3	3	5	3	3	4	3	2	3	4	4	3	1
			link 16-31	4	3	3	2	3	4	3	3	4	3	3	3	4	4	3	2
			link 32-47	3	3	0	3	3	4	3	3	4	3	2	3	3	4	3	1
			link 48-63	4	4	5	3	3	5	4	3	5	4	3	3	5	5	4	3
	Top QRL 01-5L	bgvtell01	link 0-15	4	4	4	3	3	5	3	3	5	4	3	3	5	5	4	3
			link 16-31	3	3	0	3	3	5	3	3	5	3	2	3	4	4	3	1
			link 32-47	4	4	5	3	4	5	4	3	5	4	3	4	5	5	4	3
			link 48-63	4	4	4	3	3	5	4	3	4	3	3	3	5	5	4	3
	Bottom Path 02-5L	bgvtell07	link 0-15	3	4	4	3	3	4	3	3	4	3	3	3	4	4	4	2
			link 16-31	3	3	3	3	3	4	3	3	4	3	3	3	4	4	4	2
			link 32-47	4	3	4	3	3	4	3	3	4	3	3	3	4	4	4	2
downstream			link 48-63	3	3	4	3	3	4	3	3	4	3	3	3	4	4	4	3
	Bottom QRL 03-5L	bgvtell08	link 0-15	4	4	4	3	3	5	4	3	5	4	3	3	5	5	4	3
			link 16-31	4	4	4	3	3	4	3	3	4	3	3	3	4	4	4	2
			link 32-47	5	4	5	4	4	5	4	4	6	4	4	4	6	5	5	3
			link 48-63	4	4	4	3	3	4	3	3	5	4	3	3	4	5	4	3
	Top Path 05-5L	bgvtell02	link 0-15	6	6	6	4	4	7	4	4	7	4	4	4	7	7	5	4
			link 16-31	4	4	3	4	1	6	4	3	7	4	3	4	4	5	4	3
			link 32-47	6	5	5	4	4	7	4	4	7	4	4	4	7	7	5	4
			link 48-63	3	3	4	3	3	4	3	3	4	3	3	3	4	4	4	2

Table A.1.: Phase delays derived from the ADC delay scan. The phase delay is given in ns, and have to be set in the configuration file of each Tell1.

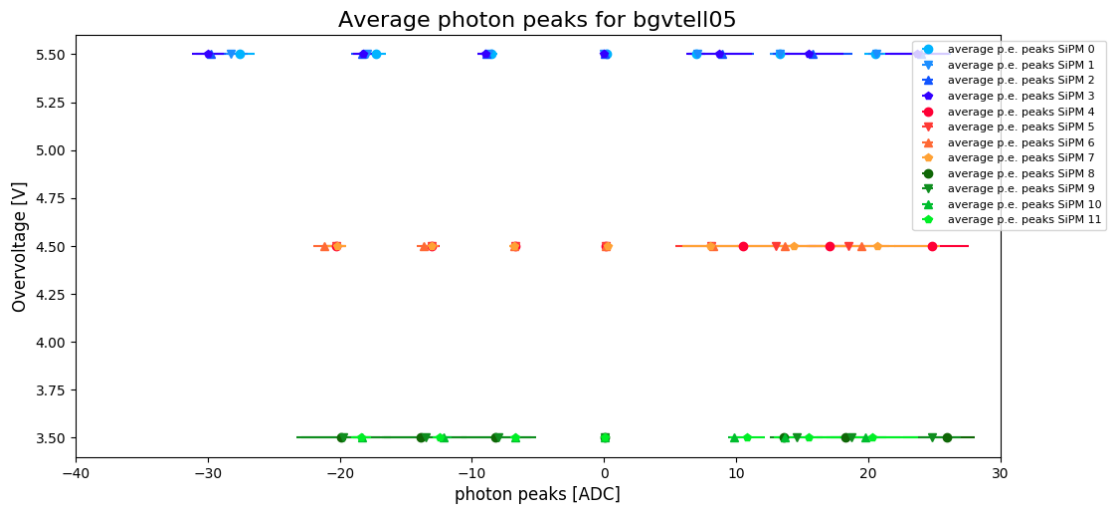## A.2. P.E. peaks results
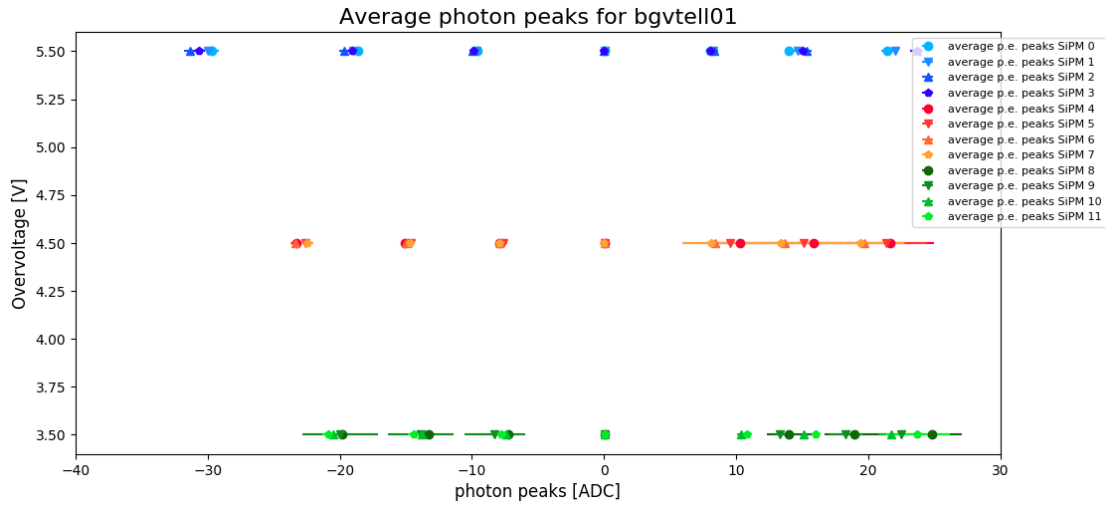
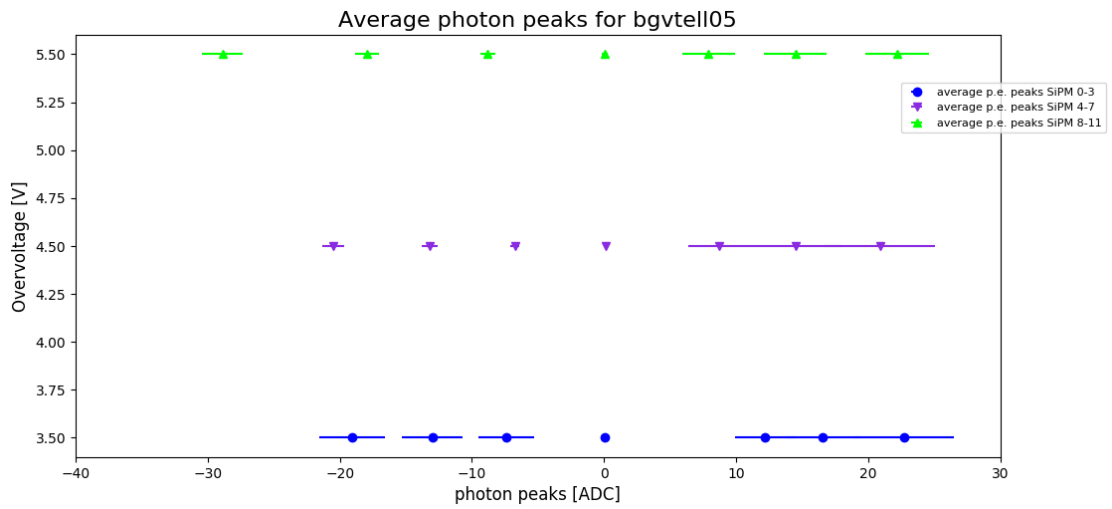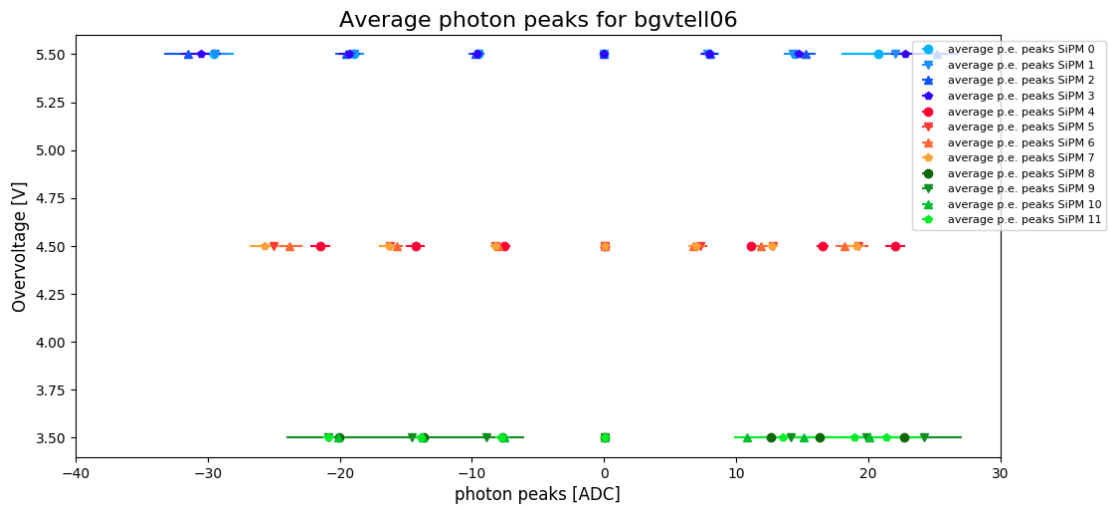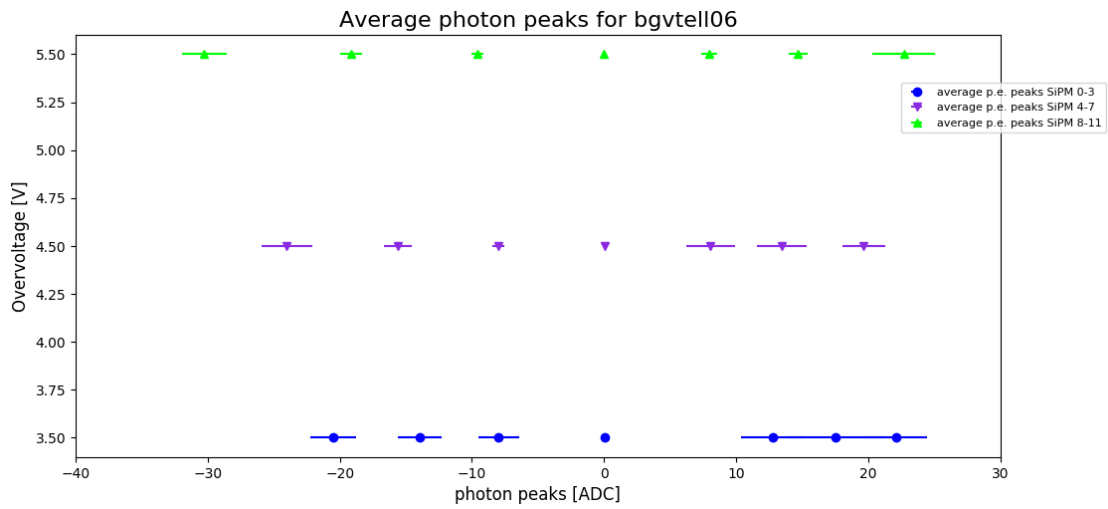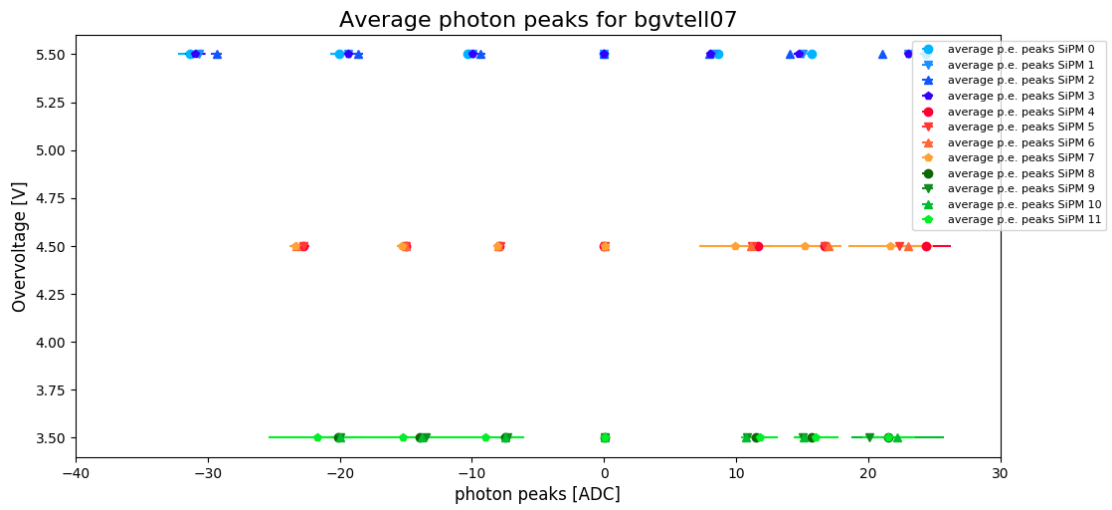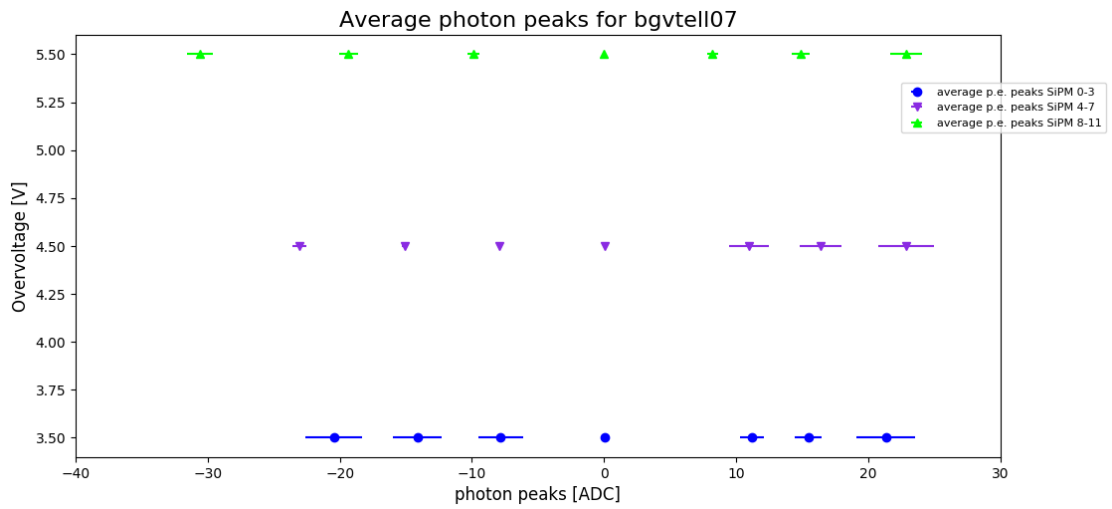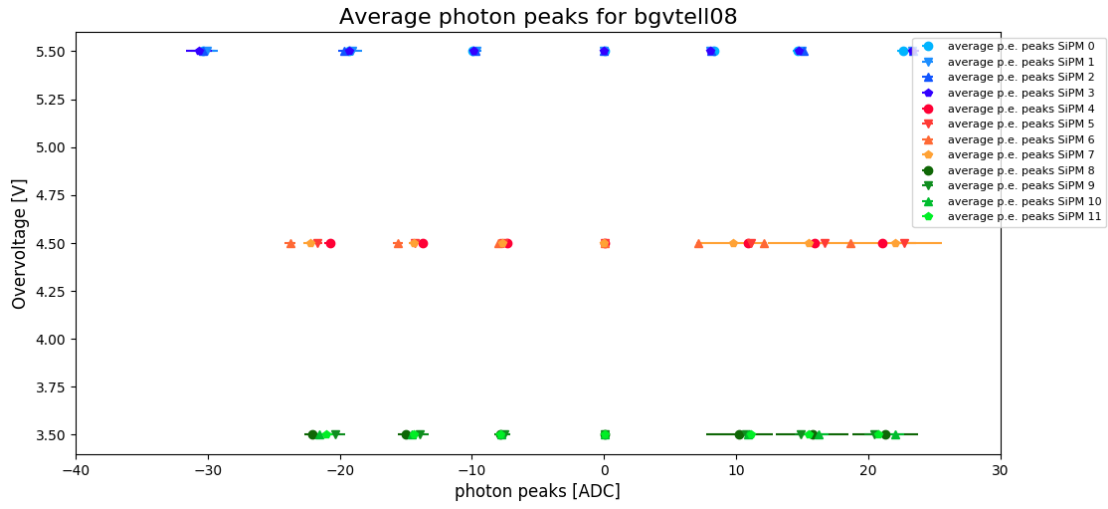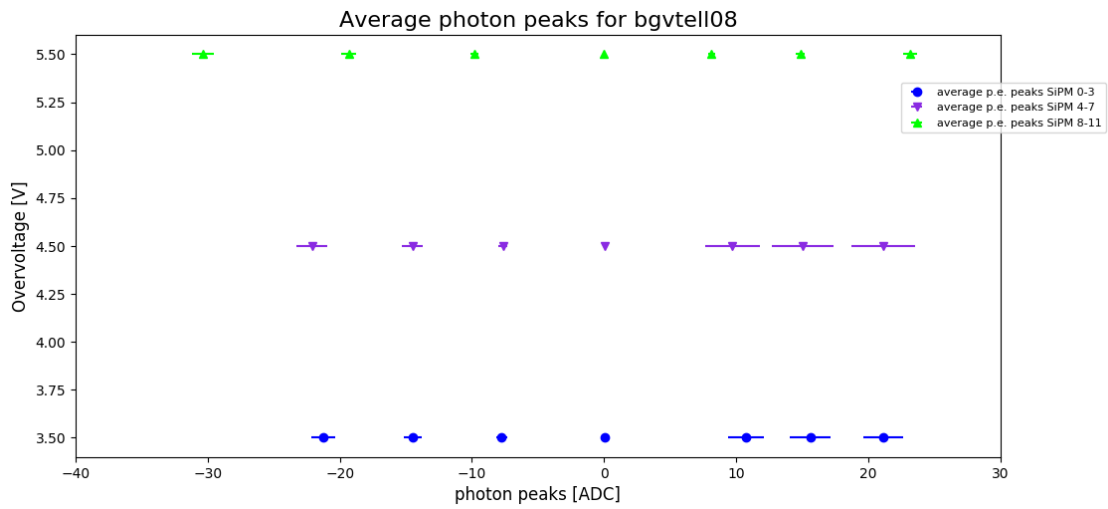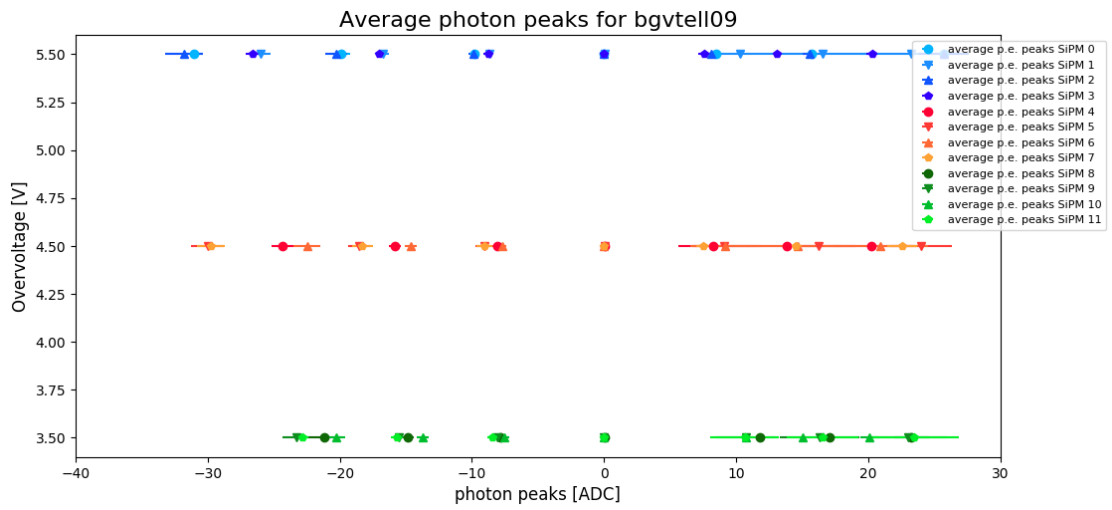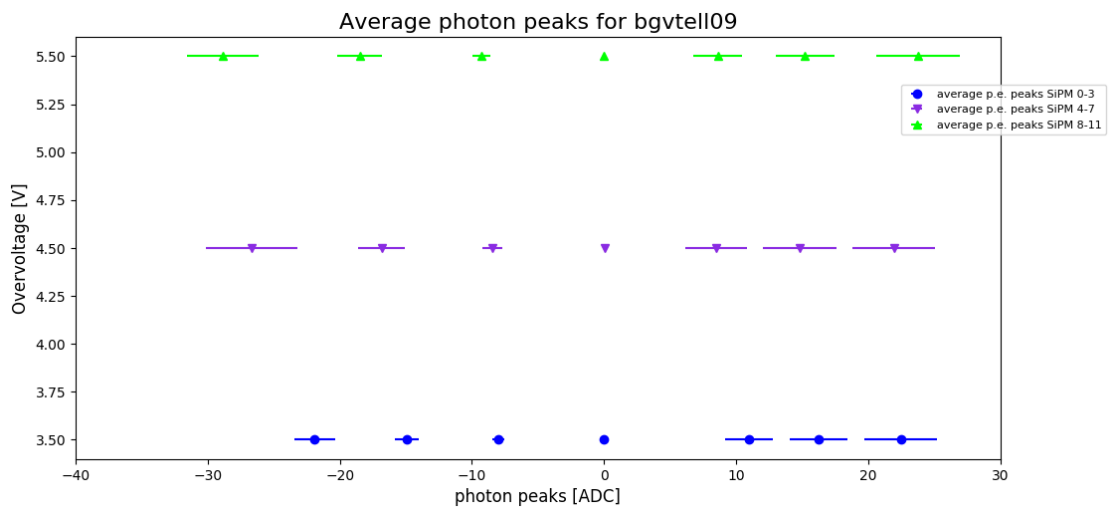(a) Temperature-averaged photoelectron peak distances at OVs 5.5 V, 4.5 V, and 3.5 V.
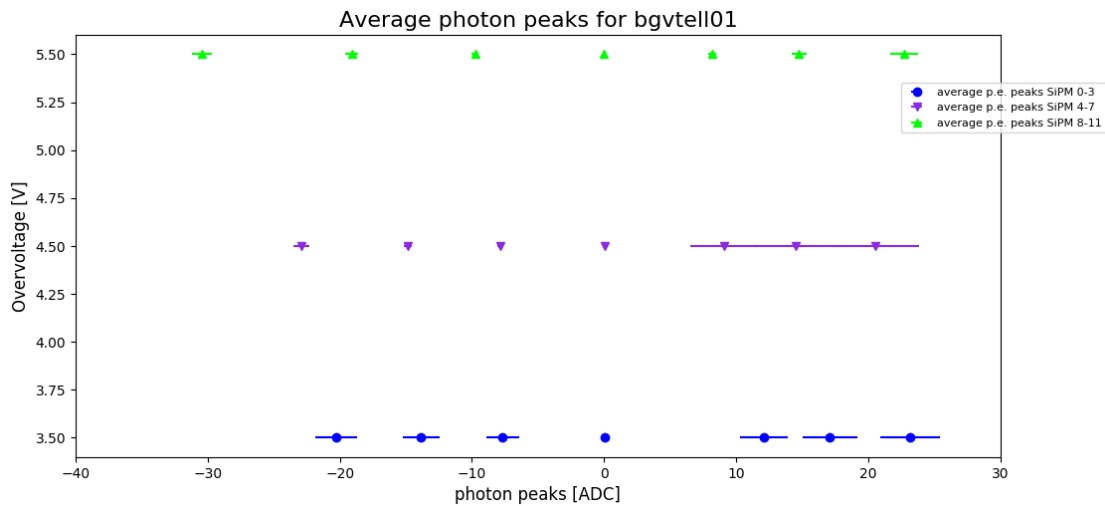
(b) Average PE peaks for all SiPMs at all temperatures in ADC counts at OVs of 5.5 V, 4.5 V, and 3.5 V.

Figure A.1.: Average PE peaks in ADC counts at OVs of 5.5 V, 4.5 V, and 3.5 V for module 01-5, bgvtell01.
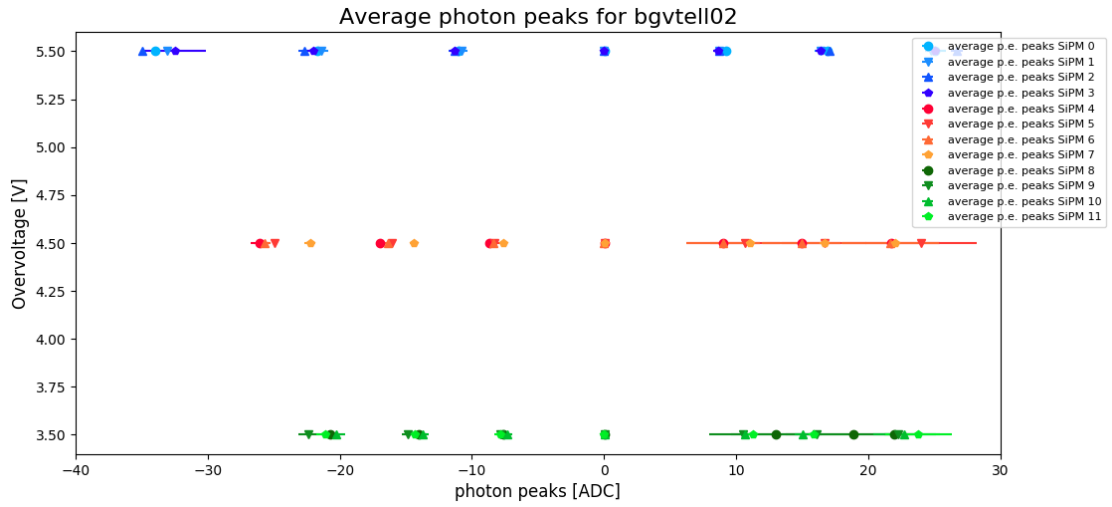
(a) Temperature-averaged photoelectron peak distances at OVs 5.5 V, 4.5 V, and 3.5 V.
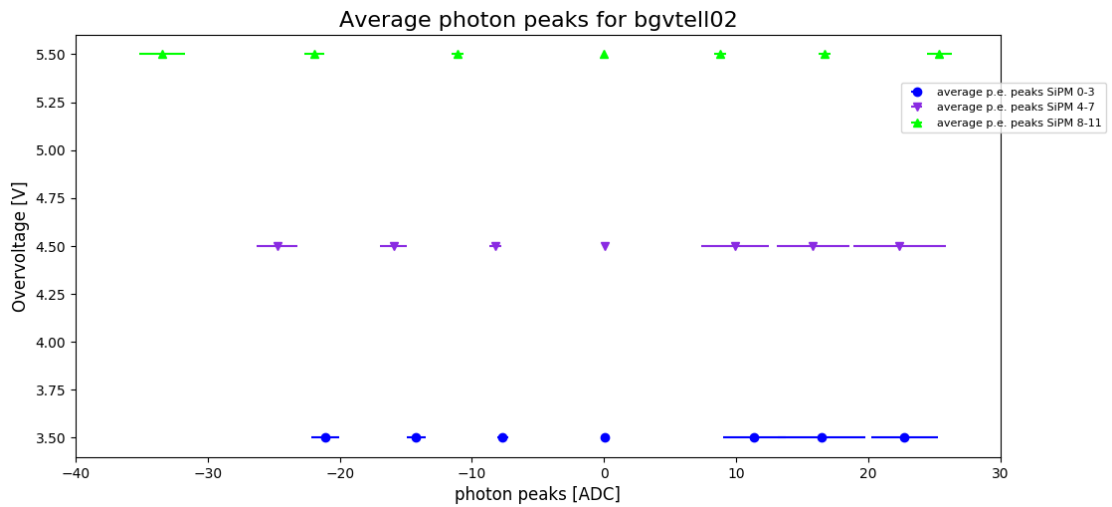
(b) Average PE peaks for all SiPMs at all temperatures in ADC counts at OVs of 5.5 V, 4.5 V, and 3.5 V.

Figure A.2.: Average PE peaks in ADC counts at OVs of 5.5 V, 4.5 V, and 3.5 V for module 05-5, bgvtell02.
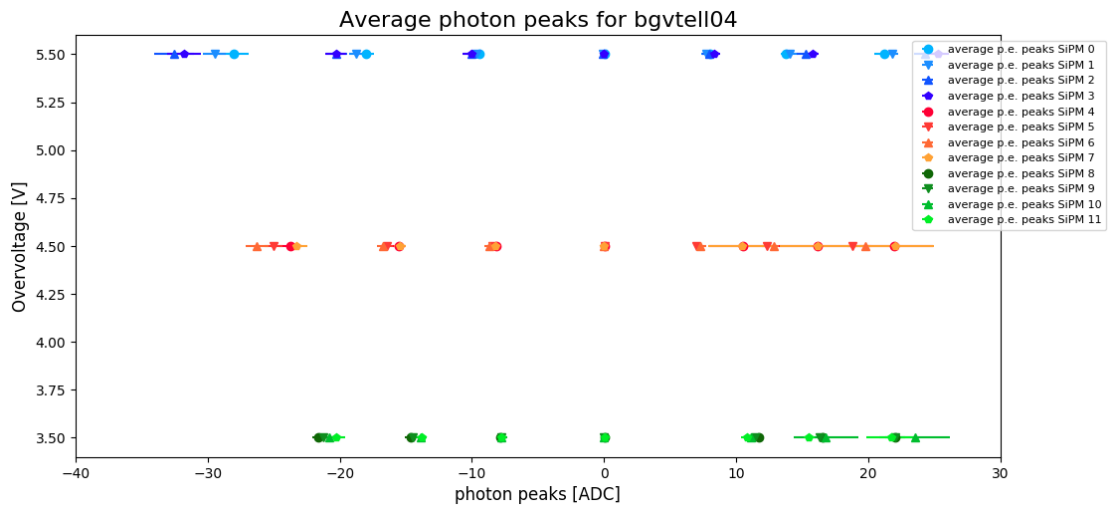
(a) Temperature-averaged photoelectron peak distances at OVs 5.5 V, 4.5 V, and 3.5 V.
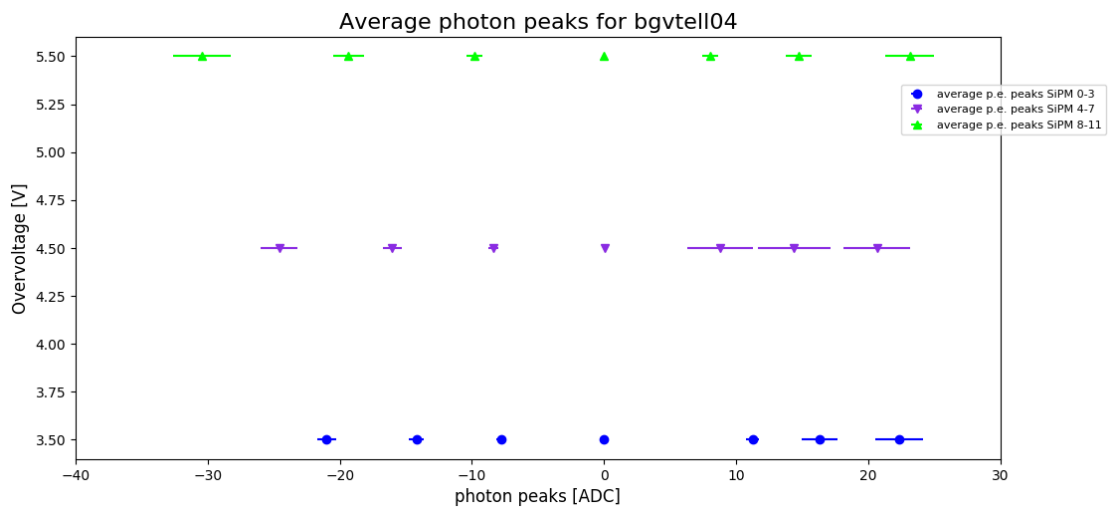
(b) Average PE peaks for all SiPMs at all temperatures in ADC counts at OVs of 5.5 V, 4.5 V, and 3.5 V.

Figure A.3.: Average PE peaks in ADC counts at OVs of 5.5 V, 4.5 V, and 3.5 V for module 09-4, bgvtell04.

(a) Temperature-averaged photoelectron peak distances at OVs 5.5 V, 4.5 V, and 3.5 V.

(b) Average PE peaks for all SiPMs at all temperatures in ADC counts at OVs of 5.5 V, 4.5 V, and 3.5 V.

Figure A.4.: Average PE peaks in ADC counts at OVs of 5.5 V, 4.5 V, and 3.5 V for module 07-4, bgvtell05.

(a) Temperature-averaged photoelectron peak distances at OVs 5.5 V, 4.5 V, and 3.5 V.

(b) Average PE peaks for all SiPMs at all temperatures in ADC counts at OVs of 5.5 V, 4.5 V, and 3.5 V.

Figure A.5.: Average PE peaks in ADC counts at OVs of 5.5 V, 4.5 V, and 3.5 V for module 08-4, bgvtell06.

(a) Temperature-averaged photoelectron peak distances at OVs 5.5 V, 4.5 V, and 3.5 V.

(b) Average PE peaks for all SiPMs at all temperatures in ADC counts at OVs of 5.5 V, 4.5 V, and 3.5 V.

Figure A.6.: Average PE peaks in ADC counts at OVs of 5.5 V, 4.5 V, and 3.5 V for module 02-5, bgvtell07.

(a) Temperature-averaged photoelectron peak distances at OVs 5.5 V, 4.5 V, and 3.5 V.

(b) Average PE peaks for all SiPMs at all temperatures in ADC counts at OVs of 5.5 V, 4.5 V, and 3.5 V.

Figure A.7.: Average PE peaks in ADC counts at OVs of 5.5 V, 4.5 V, and 3.5 V for module 03-5, bgvtell08.

(a) Temperature-averaged photoelectron peak distances at OVs 5.5 V, 4.5 V, and 3.5 V.

(b) Average PE peaks for all SiPMs at all temperatures in ADC counts at OVs of 5.5 V, 4.5 V, and 3.5 V.

Figure A.8.: Average PE peaks in ADC counts at OVs of 5.5 V, 4.5 V, and 3.5 V for module 10-4, bgvtell09.
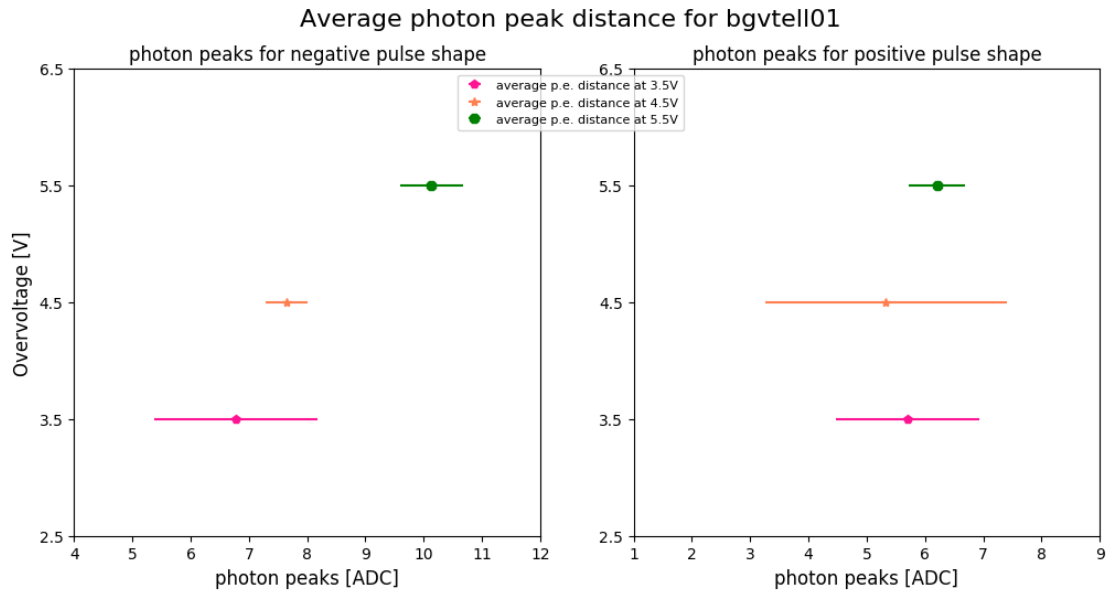
Figure A.9.: Average PE distance at OVs of 5.5 V, 4.5 V, and 3.5 V for upstream top passage module (01-5, bgvtell01).
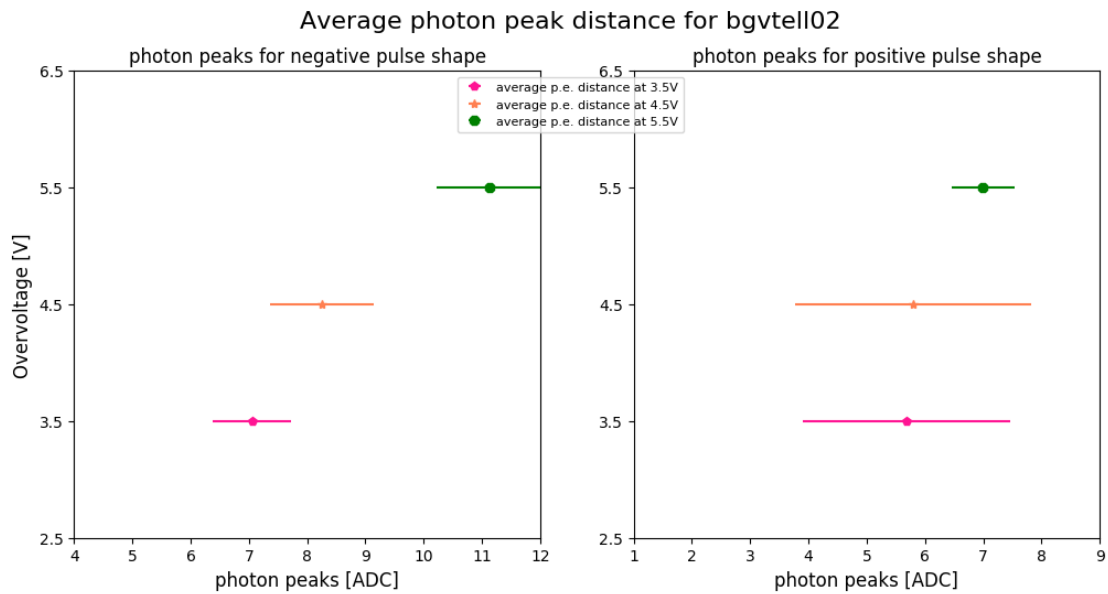
Figure A.10.: Average PE distance at OVs of 5.5 V, 4.5 V, and 3.5 V for upstream top passage module (05-5, bgvtell02).
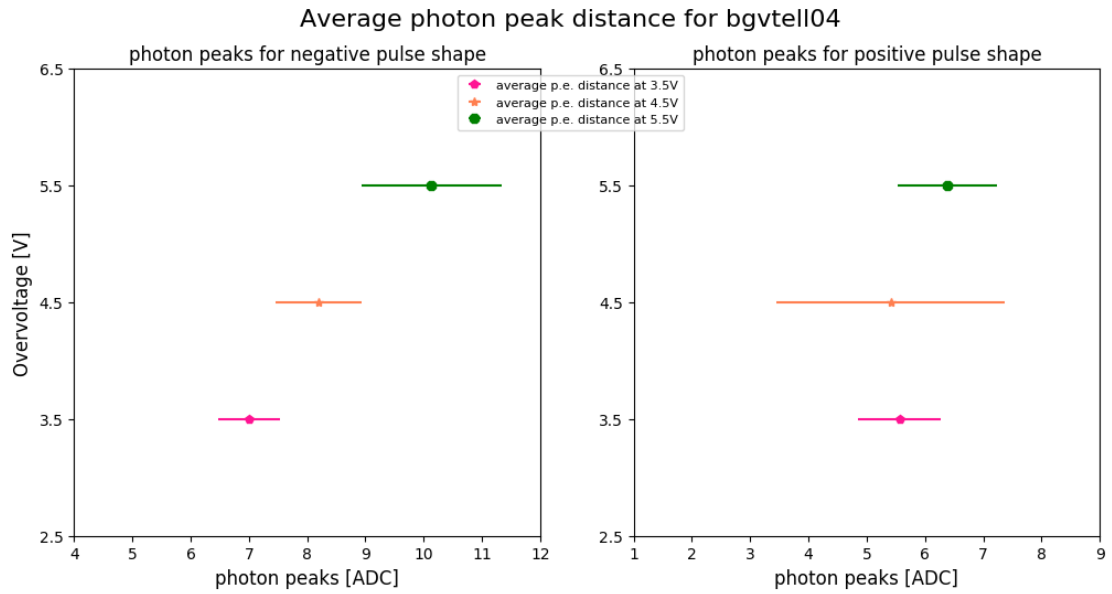
Figure A.11.: Average PE distance at OVs of 5.5 V, 4.5 V, and 3.5 V for upstream top passage module (09-4, bgvtell04).
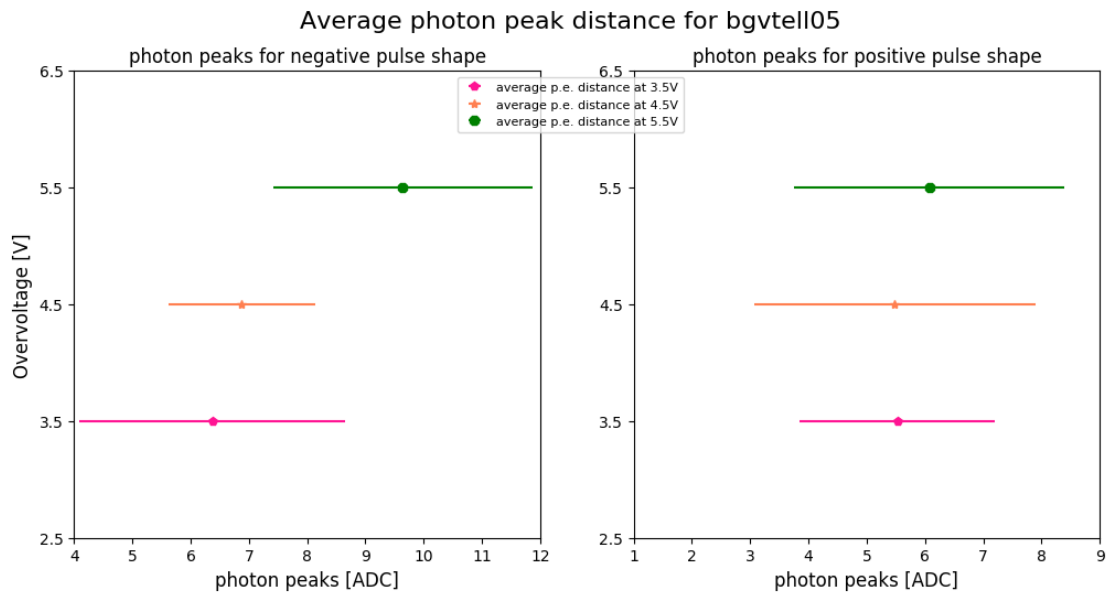
Figure A.12.: Average PE distance at OVs of 5.5 V, 4.5 V, and 3.5 V for upstream top passage module (07-4, bgvtell05).
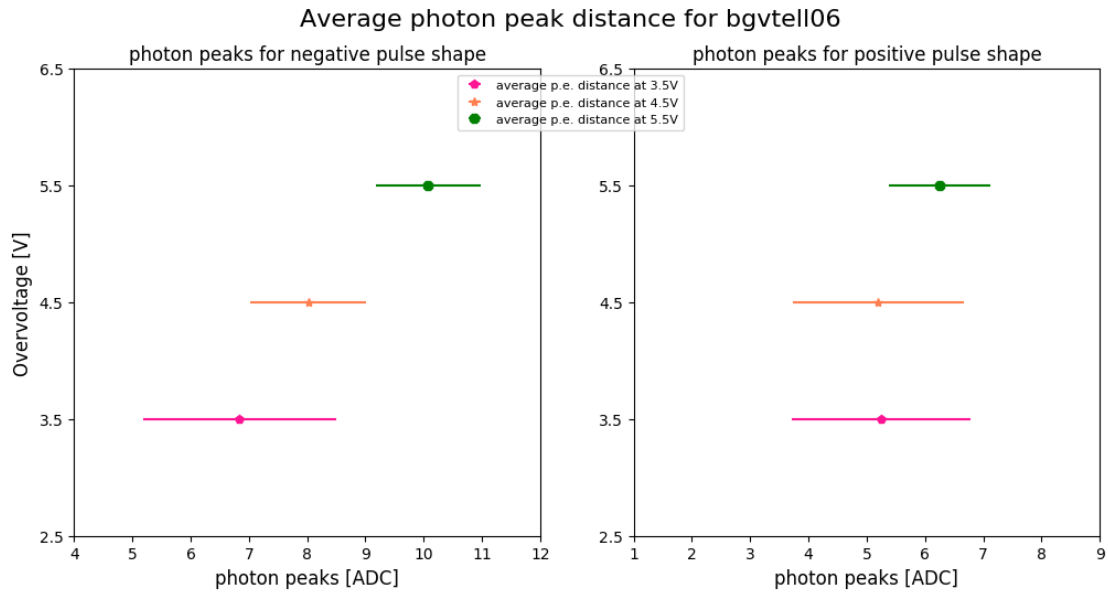
Figure A.13.: Average PE distance at OVs of 5.5 V, 4.5 V, and 3.5 V for upstream top passage module (08-4, bgvtell06).
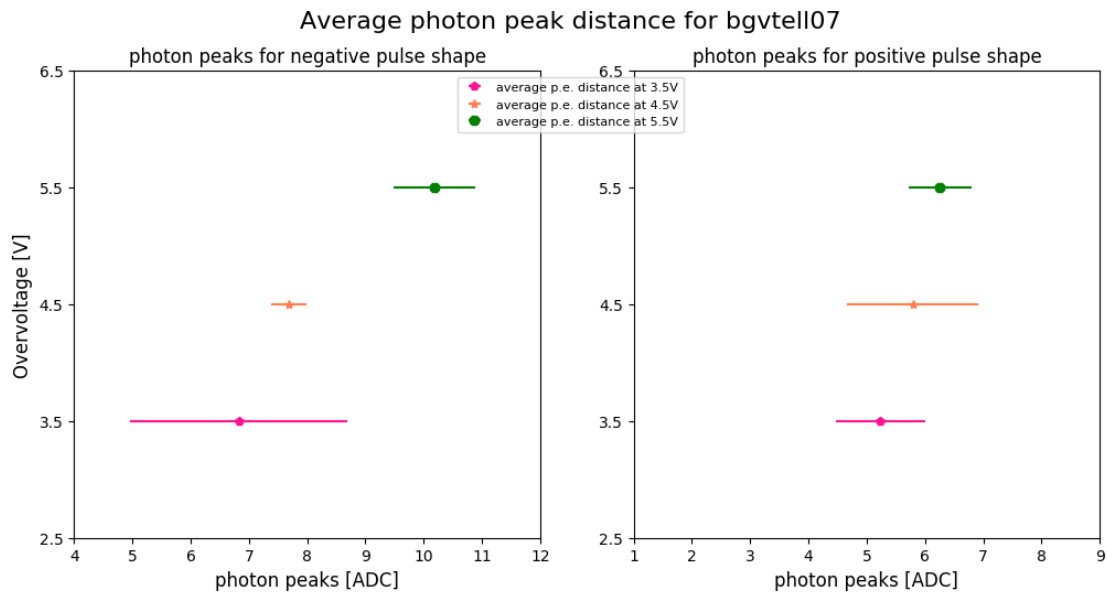
Figure A.14.: Average PE distance at OVs of 5.5 V, 4.5 V, and 3.5 V for upstream top passage module (02-5, bgvtell07).
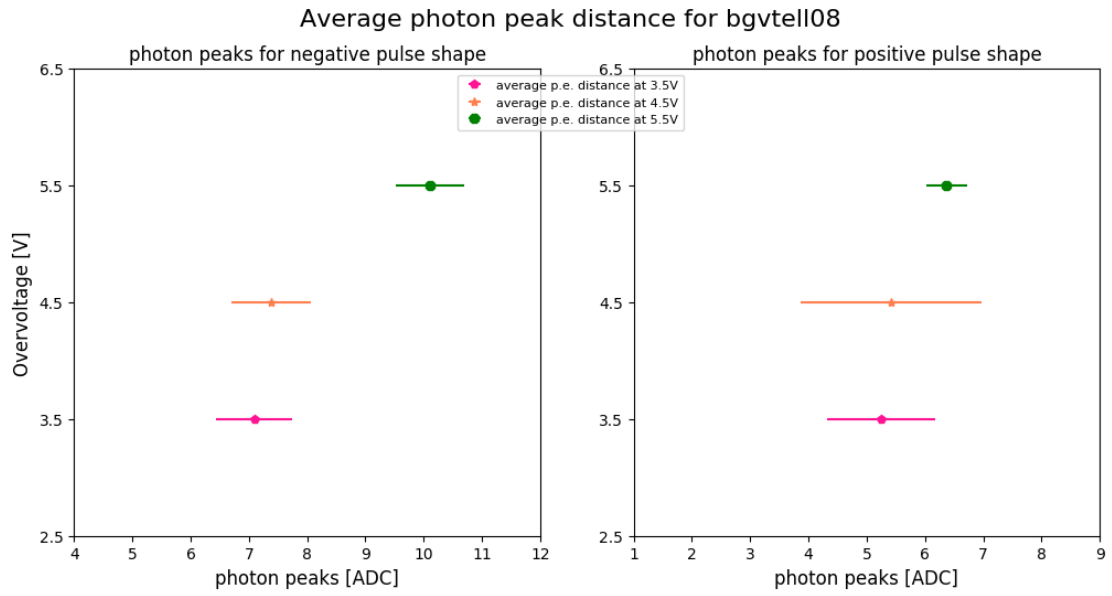
Figure A.15.: Average PE distance at OVs of 5.5 V, 4.5 V, and 3.5 V for upstream top passage module (03-5, bgvtell08).
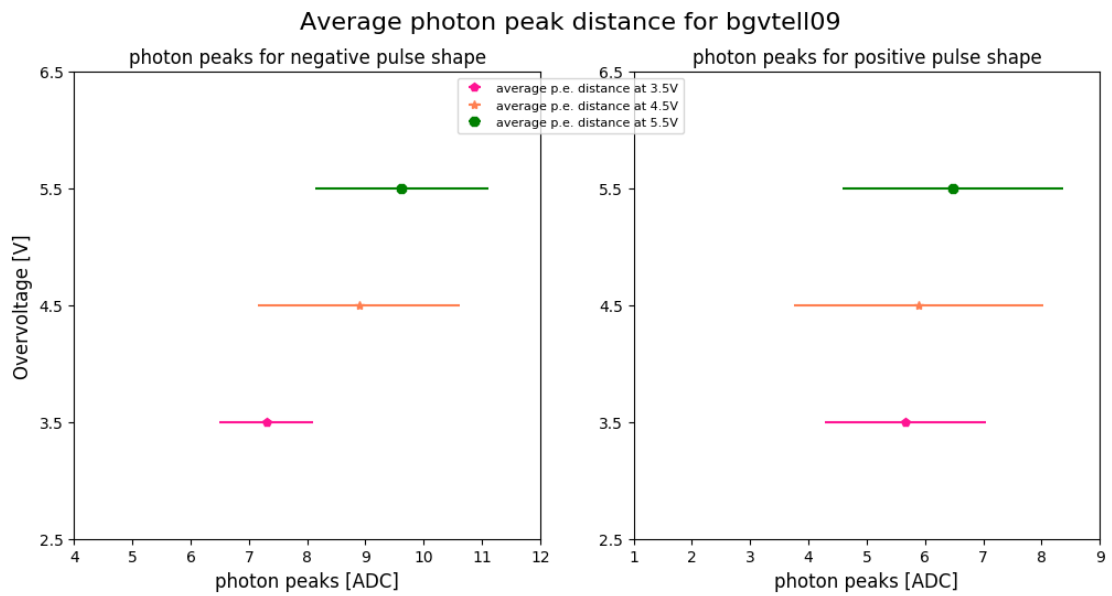
Figure A.16.: Average PE distance at OVs of 5.5 V, 4.5 V, and 3.5 V for upstream top passage module (10-4, bgvtell09).

A.3. Fill 3850

Table A.2.: Ghost charge measurement over time for fill **3850**. The systematic uncertainties are correlated from one point to the next. The gps time represents the center of the integration interval dt.

gps	dt (s)	beam 1			beam 2		
		$f_{ghost,1}$ (%)	syst. (%)	stat. (%)	$f_{ghost,2}$ (%)	syst. (%)	stat. (%)
1433967232.0	300.0	1.373	0.035	0.015	1.031	0.011	0.017
1433967532.0	300.0	1.366	0.034	0.015	1.024	0.011	0.017
1433967832.0	300.0	1.376	0.035	0.015	1.027	0.011	0.017
1433968132.0	300.0	1.393	0.035	0.016	1.039	0.014	0.017
1433968432.0	300.0	1.366	0.034	0.015	1.012	0.011	0.017
1433968732.0	300.0	1.381	0.035	0.015	1.041	0.012	0.017
1433969032.0	300.0	1.351	0.034	0.015	1.018	0.011	0.017
1433969332.0	300.0	1.354	0.035	0.015	1.013	0.010	0.017
1433969632.0	300.0	1.355	0.034	0.015	1.007	0.012	0.017
1433969932.0	300.0	1.370	0.034	0.015	0.998	0.010	0.017
1433970232.0	300.0	1.364	0.034	0.015	1.020	0.012	0.017
1433970530.0	300.0	1.361	0.034	0.015	0.962	0.010	0.016
1433970836.0	300.0	1.397	0.035	0.016	1.011	0.010	0.017
1433971136.0	300.0	1.420	0.036	0.016	0.991	0.011	0.017
1433971436.0	300.0	1.362	0.034	0.015	1.026	0.013	0.017
1433971736.0	300.0	1.360	0.034	0.015	1.014	0.011	0.017
1433972037.0	300.0	1.386	0.035	0.015	1.048	0.011	0.017
1433972347.0	300.0	1.364	0.034	0.015	1.025	0.011	0.017
1433972647.0	300.0	1.358	0.034	0.015	0.989	0.012	0.017
1433972947.0	300.0	1.403	0.035	0.016	0.985	0.012	0.016
1433973247.0	300.0	1.367	0.034	0.015	1.002	0.011	0.017
1433973604.0	300.0	1.367	0.035	0.013	0.999	0.013	0.014
1433973969.0	300.0	1.371	0.034	0.016	0.972	0.010	0.016
1433974269.0	300.0	1.391	0.035	0.016	1.019	0.013	0.017
1433974569.0	300.0	1.365	0.034	0.015	1.008	0.011	0.017
1433974869.0	300.0	1.327	0.033	0.015	1.001	0.010	0.017
1433975169.0	300.0	1.342	0.034	0.015	1.009	0.011	0.017
1433975469.0	300.0	1.376	0.035	0.016	1.011	0.011	0.017
1433975769.0	300.0	1.383	0.035	0.016	0.988	0.011	0.017
1433976069.0	300.0	1.376	0.034	0.016	1.028	0.014	0.017
1433976358.0	289.0	1.375	0.035	0.016	1.039	0.011	0.018

A.4. Fill 4266

Table A.3.: Ghost charge measurement over time for fill **4266**. The systematic uncertainties are correlated from one point to the next. The gps time represents the center of the integration interval dt.

		beam 1			beam 2		
gps	dt (s)	$f_{ghost,1}$ (%)	syst. (%)	stat. (%)	$f_{ghost,2}$ (%)	syst. (%)	stat. (%)
1440450994.0	300.0	0.125	0.006	0.004	0.000	0.000	0.000
1440451294.0	300.0	0.124	0.005	0.004	0.054	0.002	0.003
1440451619.0	325.0	0.123	0.006	0.004	0.095	0.005	0.004
1440465814.0	14195	0.117	0.006	0.004	0.088	0.004	0.004
1440466114.0	300.0	0.124	0.006	0.004	0.094	0.003	0.004
1440466419.5	305.5	0.118	0.005	0.004	0.099	0.004	0.004
1440478635.0	300.0	0.122	0.005	0.004	0.099	0.005	0.004
1440478935.0	12215.5	0.116	0.005	0.004	0.088	0.004	0.004
1440479276.0	341.0	0.121	0.007	0.003	0.093	0.004	0.004

A.5. Fill 4269

Table A.4.: Ghost charge measurement over time for fill **4269**. The systematic uncertainties are correlated from one point to the next. The gps time represents the center of the integration interval dt.

		beam 1			beam 2		
gps	dt (s)	$f_{ghost,1}$ (%)	syst. (%)	stat. (%)	$f_{ghost,2}$ (%)	syst. (%)	stat. (%)
1440515297.0	300.0	0.089	0.004	0.003	0.051	0.001	0.003
1440515649.5	352.5	0.082	0.004	0.003	0.054	0.003	0.003
1440516003.0	353.5	0.089	0.005	0.003	0.048	0.002	0.003
1440516317.0	314.0	0.085	0.005	0.005	0.041	0.002	0.004
1440517672.0	1355.0	0.106	0.005	0.021	0.054	0.002	0.020
1440517972.0	300.0	0.062	0.003	0.016	0.030	0.001	0.015
1440518272.0	300.0	0.087	0.004	0.020	0.050	0.003	0.020
1440518572.0	300.0	0.059	0.003	0.016	0.045	0.006	0.019
1440518872.0	300.0	0.096	0.006	0.021	0.008	0.000	0.008
1440519233.0	361.0	0.095	0.006	0.018	0.036	0.002	0.014
1440520036.0	803.0	0.073	0.002	0.018	0.028	0.003	0.015
1440520336.0	300.0	0.098	0.004	0.021	0.070	0.002	0.023
1440520636.0	300.0	0.144	0.019	0.026	0.046	0.007	0.019
1440520936.0	300.0	0.088	0.003	0.020	0.090	0.010	0.027

Table A.4.: Ghost charge fractions over time for fill **4269** continued.

gps	dt (s)	beam 1			beam 2		
		$f_{ghost,1}$ (%)	syst. (%)	stat. (%)	$f_{ghost,2}$ (%)	syst. (%)	stat. (%)
1440521236.0	300.0	0.096	0.006	0.021	0.055	0.001	0.021
1440521536.0	300.0	0.056	0.002	0.016	0.059	0.003	0.022
1440521836.0	300.0	0.084	0.003	0.020	0.032	0.001	0.016
1440522136.0	300.0	0.074	0.002	0.019	0.066	0.010	0.023
1440522400.5	264.5	0.061	0.003	0.019	0.010	0.000	0.010
1440522816.0	415.5	0.043	0.004	0.014	0.035	0.003	0.016
1440523116.0	300.0	0.105	0.005	0.022	0.008	0.000	0.008
1440523416.0	300.0	0.098	0.006	0.021	0.039	0.001	0.018
1440523716.0	300.0	0.068	0.002	0.018	0.039	0.001	0.018
1440524016.0	300.0	0.092	0.006	0.020	0.019	0.003	0.012
1440524286.5	270.5	0.069	0.005	0.020	0.062	0.003	0.024
1440524565.0	278.5	0.069	0.003	0.018	0.039	0.001	0.017
1440524865.0	300.0	0.084	0.002	0.020	0.048	0.007	0.020
1440525207.5	342.5	0.053	0.005	0.015	0.036	0.001	0.016
1440525558.0	350.5	0.069	0.005	0.018	0.076	0.002	0.025
1440525858.0	300.0	0.086	0.002	0.020	0.032	0.001	0.016
1440526158.0	300.0	0.135	0.006	0.025	0.035	0.003	0.017
1440526458.0	300.0	0.095	0.003	0.021	0.036	0.003	0.017
1440526758.0	300.0	0.128	0.007	0.024	0.048	0.001	0.020
1440526997.5	239.5	0.084	0.003	0.025	0.078	0.011	0.032
1440527364.0	366.5	0.088	0.004	0.003	0.046	0.002	0.003
1440527664.0	300.0	0.084	0.004	0.003	0.055	0.002	0.003
1440527964.0	300.0	0.091	0.005	0.003	0.054	0.002	0.003
1440528264.0	300.0	0.088	0.004	0.003	0.048	0.002	0.003
1440528564.0	300.0	0.092	0.004	0.003	0.042	0.002	0.003
1440528864.0	300.0	0.091	0.004	0.003	0.051	0.002	0.003
1440529231.5	367.5	0.092	0.004	0.003	0.049	0.002	0.002
1440529608.0	376.5	0.090	0.004	0.003	0.048	0.002	0.003
1440529908.0	300.0	0.095	0.004	0.003	0.047	0.001	0.003
1440530208.0	300.0	0.093	0.004	0.003	0.050	0.002	0.003
1440530508.0	300.0	0.095	0.004	0.003	0.047	0.002	0.003
1440530808.0	300.0	0.087	0.004	0.003	0.047	0.002	0.003
1440531108.0	300.0	0.094	0.005	0.003	0.052	0.002	0.003
1440531408.0	300.0	0.089	0.005	0.003	0.047	0.003	0.003
1440531708.0	300.0	0.094	0.005	0.003	0.050	0.003	0.003
1440532008.0	300.0	0.087	0.004	0.003	0.052	0.002	0.003
1440532308.0	300.0	0.088	0.005	0.003	0.044	0.002	0.003
1440532580.0	272.0	0.086	0.004	0.003	0.046	0.002	0.003
1440545146.0	12566	0.087	0.004	0.003	0.048	0.002	0.003
1440545446.0	300.0	0.090	0.004	0.003	0.051	0.002	0.003
1440545764.0	318.0	0.083	0.005	0.003	0.045	0.002	0.003

A.6. Fill 4634

Table A.5.: Ghost charge fractions over time for fill **4634**. The gps time represents the center of the integration interval dt.

gps	dt (s)	BGI beam 1		BGI beam 2		FBCT-DCCT	
		$f_{ghost,1}$ (%)	stat. (%)	$f_{ghost,2}$ (%)	stat. (%)	$f_{ghost,1}$ (%)	$f_{ghost,2}$ (%)
1447946009	300	0.000	0.000	0.000	0.000	0.732	0.136
1447946309	300	0.000	0.000	0.000	0.000	0.740	0.113
1447946609	300	0.000	0.000	0.000	0.000	0.771	0.100
1447946909	300	0.000	0.000	0.000	0.000	0.796	0.104
1447947209	300	0.000	0.000	0.000	0.000	0.794	0.105
1447947509	300	0.000	0.000	0.000	0.000	0.795	0.098
1447947809	300	0.000	0.000	0.000	0.000	0.802	0.115
1447948109	300	0.000	0.000	0.000	0.000	0.827	0.112
1447948409	300	0.000	0.000	0.000	0.000	0.815	0.126
1447948709	300	0.000	0.000	0.000	0.000	0.801	0.134
1447949009	300	0.000	0.000	0.000	0.000	0.798	0.129
1447949309	300	0.000	0.000	0.000	0.000	0.776	0.123
1447949609	300	0.000	0.000	0.000	0.000	0.784	0.130
1447949909	300	0.000	0.000	0.000	0.000	0.794	0.137
1447950209	300	0.000	0.000	0.000	0.000	0.819	0.144
1447950509	300	0.000	0.000	0.000	0.000	0.844	0.151
1447950809	300	0.000	0.000	0.000	0.000	0.852	0.147
1447951109	300	0.000	0.000	0.000	0.000	0.864	0.148
1447951409	300	0.000	0.000	0.000	0.000	0.885	0.146
1447951709	300	0.000	0.000	0.000	0.000	0.923	0.154
1447952009	300	0.000	0.000	0.000	0.000	0.941	0.160
1447952309	300	0.000	0.000	0.000	0.000	0.922	0.157
1447952609	300	0.000	0.000	0.000	0.000	0.926	0.155
1447952909	300	0.000	0.000	0.000	0.000	0.929	0.153
1447953209	300	0.000	0.000	0.000	0.000	0.940	0.161
1447953509	300	0.000	0.000	0.000	0.000	0.933	0.160
1447953809	300	0.000	0.000	0.000	0.000	0.915	0.176
1447954109	300	0.000	0.000	0.000	0.000	0.892	0.171
1447954409	300	0.000	0.000	0.000	0.000	0.901	0.158
1447954709	300	0.888	0.012	0.164	0.006	-	-
1447955009	300	0.872	0.012	0.163	0.006	-	-
1447955309	300	0.827	0.012	0.160	0.006	-	-
1447955609	300	0.822	0.012	0.163	0.006	-	-
1447955909	300	0.833	0.012	0.149	0.006	-	-
1447956209	300	0.846	0.012	0.169	0.006	-	-

Table A.5.: Ghost charge fractions over time for fill **4634** continued.

| gps | dt (s) | BGI beam 1 | | BGI beam 2 | | FBCT-DCCT | |
		$f_{ghost,1}$ (%)	stat. (%)	$f_{ghost,2}$ (%)	stat. (%)	$f_{ghost,1}$ (%)	$f_{ghost,2}$ (%)
1447956509	300	0.869	0.012	0.167	0.006	-	-
1447956809	300	0.888	0.012	0.163	0.006	-	-
1447957109	300	0.945	0.013	0.176	0.006	-	-
1447957409	300	0.977	0.013	0.179	0.006	-	-
1447957709	300	1.019	0.013	0.161	0.006	-	-
1447958009	300	1.106	0.017	0.176	0.008	-	-
1447958309	300	0.000	0.000	0.000	0.000	1.122	0.161
1447958609	300	0.000	0.000	0.000	0.000	1.168	0.159
1447958909	300	0.000	0.000	0.000	0.000	1.192	0.157
1447959209	300	1.225	0.015	0.180	0.006	-	-
1447959509	300	1.235	0.015	0.164	0.006	-	-
1447959809	300	1.216	0.015	0.172	0.006	-	-
1447960109	300	1.299	0.015	0.189	0.007	-	-
1447960409	300	1.336	0.015	0.175	0.006	-	-
1447960709	300	1.339	0.016	0.178	0.006	-	-
1447961009	300	1.308	0.015	0.179	0.006	-	-
1447961309	300	1.357	0.016	0.185	0.007	-	-
1447961609	300	1.372	0.016	0.175	0.006	-	-
1447961909	300	1.388	0.016	0.187	0.007	-	-
1447962209	300	1.407	0.016	0.183	0.007	-	-
1447962509	300	1.412	0.016	0.185	0.007	-	-
1447962809	300	1.434	0.016	0.187	0.007	-	-
1447963109	300	1.435	0.016	0.186	0.007	-	-
1447963409	300	1.429	0.016	0.195	0.007	-	-
1447963709	300	1.432	0.016	0.193	0.007	-	-
1447964009	300	1.441	0.016	0.181	0.007	-	-
1447964309	300	1.439	0.016	0.174	0.006	-	-
1447964609	300	1.475	0.017	0.193	0.007	-	-
1447964909	300	1.528	0.017	0.187	0.007	-	-
1447965209	300	1.529	0.017	0.196	0.007	-	-
1447965509	300	1.589	0.017	0.178	0.007	-	-
1447965809	300	1.582	0.017	0.198	0.007	-	-
1447966109	300	1.579	0.017	0.201	0.007	-	-
1447966409	300	1.696	0.018	0.207	0.007	-	-
1447966709	300	1.815	0.019	0.182	0.007	-	-
1447967009	300	1.907	0.019	0.190	0.007	-	-
1447967309	300	2.119	0.017	0.202	0.006	-	-
1447967609	300	0.000	0.000	0.000	0.000	2.142	0.160
1447967909	300	2.309	0.021	0.202	0.007	-	-
1447968209	300	2.359	0.022	0.206	0.007	-	-
1447968509	300	2.415	0.019	0.213	0.006	-	-
1447968809	300	0.000	0.000	0.000	0.000	2.476	0.158

Table A.5.: Ghost charge fractions over time for fill **4634** continued.

		BGI beam 1		BGI beam 2		FBCT-DCCT	
gps	dt (s)	$f_{ghost,1}$ (%)	stat. (%)	$f_{ghost,2}$ (%)	stat. (%)	$f_{ghost,1}$ (%)	$f_{ghost,2}$ (%)
1447969109	300	0.000	0.000	0.000	0.000	2.517	0.165
1447969409	300	2.401	0.022	0.194	0.007	-	-
1447969709	300	2.388	0.022	0.200	0.007	-	-
1447970009	300	2.380	0.022	0.213	0.007	-	-
1447970309	300	2.263	0.021	0.212	0.007	-	-
1447970609	300	2.152	0.021	0.198	0.007	-	-
1447970909	300	2.083	0.021	0.213	0.007	-	-
1447971209	300	1.985	0.020	0.228	0.008	-	-
1447971509	300	1.885	0.020	0.215	0.007	-	-
1447971809	300	1.802	0.019	0.224	0.007	-	-
1447972109	300	1.755	0.019	0.218	0.007	-	-
1447972409	300	0.000	0.000	0.000	0.000	1.773	0.173
1447972709	300	0.000	0.000	0.000	0.000	1.756	0.180
1447973009	300	0.000	0.000	0.000	0.000	1.717	0.188
1447973309	300	0.000	0.000	0.000	0.000	1.681	0.187
1447973609	300	1.892	0.099	0.260	0.044	-	-
1447973909	300	1.974	0.107	0.253	0.046	-	-
1447974209	300	2.010	0.110	0.273	0.050	-	-
1447974509	300	1.993	0.112	0.363	0.058	-	-
1447974809	300	0.000	0.000	0.000	0.000	1.561	0.182
1447975109	300	1.580	0.085	0.223	0.038	-	-
1447975409	300	1.685	0.106	0.258	0.051	-	-
1447975709	300	1.432	0.097	0.185	0.043	-	-
1447976009	300	1.429	0.098	0.282	0.054	-	-
1447976309	300	1.482	0.102	0.270	0.052	-	-
1447976609	300	1.460	0.100	0.240	0.051	-	-
1447976909	300	1.340	0.096	0.325	0.057	-	-
1447977209	300	1.396	0.100	0.211	0.047	-	-
1447977509	300	1.417	0.101	0.209	0.047	-	-
1447977809	300	1.383	0.100	0.291	0.056	-	-
1447978109	300	1.380	0.101	0.209	0.047	-	-
1447978409	300	1.417	0.103	0.343	0.062	-	-
1447978709	300	1.389	0.101	0.248	0.052	-	-
1447979009	300	1.666	0.112	0.254	0.053	-	-
1447979309	300	1.313	0.099	0.252	0.053	-	-
1447979609	300	1.517	0.107	0.297	0.057	-	-
1447979909	300	1.535	0.107	0.290	0.057	-	-
1447980209	300	1.719	0.149	0.181	0.059	-	-
1447980509	300	0.000	0.000	0.000	0.000	1.197	0.242
1447980809	300	0.000	0.000	0.000	0.000	1.139	0.254
1447981109	300	1.250	0.015	0.297	0.009	-	-
1447981409	300	1.200	0.015	0.306	0.009	-	-

Table A.5.: Ghost charge fractions over time for fill **4634** continued.

gps	dt (s)	BGI beam 1		BGI beam 2		FBCT-DCCT	
		$f_{ghost,1}$ (%)	stat. (%)	$f_{ghost,2}$ (%)	stat. (%)	$f_{ghost,1}$ (%)	$f_{ghost,2}$ (%)
1447981709	300	1.201	0.015	0.312	0.009	-	-
1447982009	300	1.163	0.015	0.310	0.009	-	-
1447982309	300	0.000	0.000	0.000	0.000	0.959	0.282
1447982609	300	0.000	0.000	0.000	0.000	0.941	0.279
1447982909	300	0.000	0.000	0.000	0.000	0.930	0.276
1447983209	300	0.000	0.000	0.000	0.000	0.919	0.275
1447983509	300	0.000	0.000	0.000	0.000	0.959	0.281
1447983809	300	0.000	0.000	0.000	0.000	1.005	0.285
1447984109	300	0.000	0.000	0.000	0.000	0.992	0.285
1447984409	300	0.986	0.015	0.286	0.009	-	-
1447984709	300	0.996	0.015	0.299	0.009	-	-
1447985009	300	0.982	0.015	0.299	0.009	-	-
1447985309	300	0.989	0.015	0.292	0.009	-	-
1447985609	300	0.938	0.014	0.301	0.009	-	-
1447985909	300	0.908	0.014	0.300	0.009	-	-
1447986209	300	0.877	0.014	0.321	0.009	-	-
1447986509	300	0.867	0.014	0.306	0.009	-	-
1447986809	300	0.838	0.013	0.325	0.009	-	-
1447987109	300	0.855	0.014	0.313	0.009	-	-
1447987409	300	0.838	0.014	0.326	0.009	-	-
1447987709	300	0.842	0.014	0.325	0.010	-	-
1447988009	300	0.847	0.014	0.320	0.009	-	-
1447988309	300	0.908	0.014	0.324	0.009	-	-
1447988609	300	0.923	0.014	0.324	0.009	-	-
1447988909	300	0.886	0.014	0.329	0.010	-	-
1447989209	300	0.904	0.014	0.335	0.010	-	-
1447989509	300	0.896	0.014	0.330	0.010	-	-
1447989809	300	0.879	0.014	0.350	0.010	-	-
1447990109	300	0.850	0.014	0.343	0.010	-	-
1447990409	300	0.799	0.013	0.330	0.010	-	-
1447990709	300	0.799	0.013	0.329	0.010	-	-
1447991009	300	0.746	0.013	0.326	0.010	-	-
1447991309	300	0.734	0.013	0.339	0.010	-	-
1447991609	300	0.696	0.012	0.355	0.010	-	-
1447991909	300	0.700	0.013	0.337	0.010	-	-
1447992209	300	0.675	0.012	0.353	0.010	-	-
1447992509	300	0.687	0.012	0.354	0.010	-	-
1447992809	300	0.641	0.012	0.341	0.010	-	-
1447993109	300	0.657	0.012	0.344	0.010	-	-
1447993409	300	0.627	0.012	0.333	0.010	-	-
1447993709	300	0.607	0.012	0.361	0.010	-	-
1447994009	300	0.627	0.012	0.352	0.010	-	-

Table A.5.: Ghost charge fractions over time for fill **4634** continued.

		BGI beam 1		BGI beam 2		FBCT-DCCT	
gps	dt (s)	$f_{ghost,1}$ (%)	stat. (%)	$f_{ghost,2}$ (%)	stat. (%)	$f_{ghost,1}$ (%)	$f_{ghost,2}$ (%)
1447994309	300	0.614	0.012	0.346	0.010	-	-
1447994609	300	0.587	0.012	0.343	0.010	-	-
1447994909	300	0.605	0.012	0.351	0.010	-	-
1447995209	300	0.622	0.012	0.364	0.010	-	-
1447995509	300	0.640	0.012	0.347	0.010	-	-
1447995809	300	0.652	0.012	0.353	0.010	-	-
1447996109	300	0.620	0.012	0.347	0.010	-	-
1447996409	300	0.628	0.012	0.356	0.010	-	-
1447996709	300	0.644	0.012	0.363	0.010	-	-
1447997009	300	0.655	0.014	0.338	0.011	-	-
1447997309	300	0.661	0.012	0.370	0.010	-	-
1447997609	300	0.641	0.012	0.369	0.010	-	-
1447997909	300	0.667	0.012	0.363	0.010	-	-
1447998209	300	0.662	0.012	0.386	0.011	-	-
1447998509	300	0.675	0.013	0.373	0.010	-	-
1447998809	300	0.663	0.012	0.407	0.011	-	-
1447999109	300	0.674	0.013	0.364	0.010	-	-
1447999409	300	0.671	0.013	0.366	0.010	-	-
1447999709	300	0.651	0.012	0.395	0.011	-	-

A.7. Fill 4689

Table A.6.: **Corrected** ghost charge fractions over time for fill **4689**. The global relative systematic uncertainty for this fill is 24.3%, as shown in table 4.6. The gps time represents the center of the integration interval dt.

		beam 1		beam 2	
gps	dt (s)	$f_{ghost,1}^{corr}$ (%)	stat. (%)	$f_{ghost,2}^{corr}$ (%)	stat. (%)
1449134132.0	600.0	3.144	0.140	2.335	0.121
1449134732.0	600.0	3.204	0.145	2.160	0.114
1449135332.0	600.0	3.344	0.150	2.108	0.113
1449135932.0	600.0	3.313	0.150	1.959	0.107
1449136532.0	600.0	3.432	0.156	2.375	0.124
1449137132.0	600.0	3.619	0.165	2.089	0.114
1449137732.0	600.0	3.603	0.163	2.187	0.117
1449138332.0	600.0	3.299	0.151	2.334	0.125
1449138932.0	600.0	3.480	0.159	2.147	0.116

Table A.6.: Ghost charge fractions over time for fill **4689** continued.

		beam 1		beam 2	
gps	dt (s)	$f_{ghost,1}^{corr}$ (%)	stat. (%)	$f_{ghost,2}^{corr}$ (%)	stat. (%)
1449139532.0	600.0	3.884	0.176	2.613	0.135
1449140132.0	600.0	3.789	0.176	2.113	0.113
1449140732.0	600.0	3.574	0.164	2.511	0.131
1449141332.0	600.0	3.680	0.172	2.351	0.125
1449141932.0	600.0	3.726	0.172	2.245	0.123
1449142532.0	600.0	4.009	0.182	2.251	0.120
1449143132.0	600.0	3.940	0.177	2.515	0.134
1449143732.0	600.0	3.665	0.167	2.197	0.120
1449144332.0	600.0	4.066	0.185	2.491	0.130
1449144932.0	600.0	4.024	0.185	2.354	0.129
1449145532.0	600.0	3.744	0.172	2.615	0.138
1449146132.0	600.0	3.927	0.179	2.719	0.143
1449146732.0	600.0	3.739	0.177	2.745	0.146
1449147332.0	600.0	3.942	0.179	2.744	0.150
1449147932.0	600.0	3.912	0.183	2.550	0.137
1449148532.0	600.0	4.318	0.198	2.275	0.126
1449149132.0	600.0	3.844	0.182	2.664	0.140
1449149732.0	600.0	4.304	0.200	2.432	0.135
1449150332.0	600.0	4.338	0.203	2.580	0.141
1449150932.0	600.0	4.069	0.187	2.565	0.142
1449151532.0	600.0	4.235	0.193	2.421	0.135
1449152132.0	600.0	4.154	0.198	2.686	0.143
1449152732.0	600.0	4.447	0.206	2.722	0.147
1449153332.0	600.0	4.120	0.194	2.502	0.141
1449153932.0	600.0	4.645	0.217	2.706	0.151
1449154532.0	600.0	4.791	0.223	3.025	0.164
1449155132.0	600.0	4.510	0.213	2.690	0.146
1449155732.0	600.0	4.386	0.209	2.715	0.151
1449156332.0	600.0	4.203	0.198	3.124	0.170
1449156932.0	600.0	5.162	0.247	2.623	0.149
1449157532.0	600.0	4.001	0.189	2.748	0.150
1449158132.0	600.0	4.922	0.233	2.604	0.146
1449158732.0	600.0	4.577	0.218	2.971	0.159
1449159332.0	600.0	4.636	0.221	2.506	0.143
1449159932.0	600.0	4.450	0.211	3.175	0.173
1449160532.0	600.0	4.836	0.225	2.957	0.159
1449161132.0	600.0	4.659	0.220	2.617	0.145
1449161732.0	600.0	4.755	0.226	2.670	0.149
1449162332.0	600.0	4.718	0.227	3.084	0.166
1449162932.0	600.0	4.976	0.240	3.159	0.176
1449163532.0	600.0	5.079	0.245	3.254	0.172
1449164132.0	600.0	4.561	0.220	3.044	0.163

Table A.6.: Ghost charge fractions over time for fill **4689** continued.

		beam 1		beam 2	
gps	dt (s)	$f_{ghost,1}^{corr}$ (%)	stat. (%)	$f_{ghost,2}^{corr}$ (%)	stat. (%)
1449164732.0	600.0	4.860	0.235	3.062	0.166
1449165332.0	600.0	5.502	0.262	3.135	0.175
1449165835.0	503.0	5.293	0.303	3.071	0.204

A.8. Fill 4690

Table A.7.: **Corrected** ghost charge measurement over time for fill **4690**. The global relative systematic uncertainty for this fill is 24.3%, as shown in table 4.6. The gps time represents the center of the integration interval dt.

		beam 1		beam 2	
gps	dt (s)	$f_{ghost,1}^{corr}$ (%)	stat. (%)	$f_{ghost,2}^{corr}$ (%)	stat. (%)
1449181382.0	600.0	2.058	0.091	1.346	0.072
1449181982.0	600.0	2.121	0.095	1.411	0.077
1449182582.0	600.0	2.183	0.097	1.377	0.074
1449183182.0	600.0	2.116	0.094	1.606	0.084
1449183782.0	600.0	2.022	0.092	1.529	0.081
1449184382.0	600.0	1.992	0.092	1.485	0.081
1449184982.0	600.0	2.086	0.094	1.594	0.084
1449185582.0	600.0	2.113	0.097	1.568	0.083
1449186182.0	600.0	2.296	0.104	1.776	0.091
1449186782.0	600.0	2.152	0.098	1.520	0.081
1449187382.0	600.0	2.343	0.105	1.662	0.087
1449187982.0	600.0	2.318	0.104	1.859	0.097
1449188582.0	600.0	2.247	0.102	1.513	0.083
1449189182.0	600.0	2.305	0.107	1.775	0.093
1449189782.0	600.0	2.344	0.107	1.850	0.095
1449190382.0	600.0	2.274	0.101	1.784	0.094
1449190982.0	600.0	2.398	0.109	1.774	0.094
1449191582.0	600.0	2.502	0.115	1.604	0.088
1449192182.0	600.0	2.442	0.110	1.788	0.092
1449192782.0	600.0	2.460	0.113	1.807	0.094
1449193382.0	600.0	2.589	0.117	1.682	0.091
1449193982.0	600.0	2.546	0.117	1.941	0.105
1449194582.0	600.0	2.615	0.124	1.849	0.101
1449195182.0	600.0	2.964	0.142	1.739	0.100
1449195782.0	600.0	2.923	0.131	2.019	0.109

Table A.7.: Ghost charge fractions over time for fill **4690** continued.

gps	dt (s)	beam 1		beam 2	
		$f_{ghost,1}^{corr}$ (%)	stat. (%)	$f_{ghost,2}^{corr}$ (%)	stat. (%)
1449196382.0	600.0	2.733	0.125	2.124	0.112
1449196982.0	600.0	2.941	0.135	2.099	0.109
1449197582.0	600.0	2.835	0.129	2.022	0.109
1449198182.0	600.0	2.995	0.144	1.820	0.103
1449198782.0	600.0	2.804	0.134	2.151	0.114
1449199382.0	600.0	2.997	0.142	1.856	0.104
1449199982.0	600.0	2.998	0.140	2.286	0.119
1449200582.0	600.0	3.228	0.150	2.217	0.119
1449201182.0	600.0	3.100	0.145	2.118	0.116
1449201782.0	600.0	3.411	0.160	2.312	0.124
1449202382.0	600.0	3.095	0.148	2.156	0.115
1449202982.0	600.0	2.689	0.130	2.087	0.114
1449203582.0	600.0	3.148	0.151	2.325	0.126
1449204182.0	600.0	3.330	0.158	2.251	0.122
1449204782.0	600.0	3.279	0.156	2.174	0.124
1449205382.0	600.0	3.322	0.158	2.298	0.127
1449205982.0	600.0	3.335	0.168	2.283	0.128
1449206582.0	600.0	3.820	0.177	2.203	0.122
1449207182.0	600.0	3.639	0.173	2.394	0.136
1449207782.0	600.0	3.972	0.188	2.477	0.138
1449208382.0	600.0	3.292	0.158	2.692	0.148
1449208982.0	600.0	3.663	0.176	2.361	0.133
1449209582.0	600.0	4.012	0.188	2.676	0.147
1449210182.0	600.0	3.402	0.164	2.695	0.150
1449210752.0	570.0	3.758	0.188	2.372	0.142

A.9. Fill 4691

Table A.8.: **Corrected** ghost charge measurement over time for fill **4691**. The global relative systematic uncertainty for this fill is 27.6%, as shown in table 4.6. The gps time represents the center of the integration interval dt.

gps	dt (s)	beam 1		beam 2	
		$f_{ghost,1}^{corr}$ (%)	stat. (%)	$f_{ghost,2}^{corr}$ (%)	stat. (%)
1449235094.0	600.0	2.088	0.099	1.851	0.097
1449235694.0	600.0	2.367	0.106	1.951	0.097
1449236294.0	600.0	2.241	0.092	1.984	0.091

Table A.8.: Ghost charge fractions over time for fill **4691** continued.

gps	dt (s)	beam 1		beam 2	
		$f_{ghost,1}^{corr}$ (%)	stat. (%)	$f_{ghost,2}^{corr}$ (%)	stat. (%)
1449236894.0	600.0	2.204	0.093	2.040	0.092
1449237494.0	600.0	2.420	0.100	2.215	0.101
1449238094.0	600.0	2.484	0.101	2.009	0.092
1449238694.0	600.0	2.404	0.101	2.167	0.098
1449239294.0	600.0	2.254	0.095	2.301	0.103
1449239894.0	600.0	1.816	0.327	2.429	0.427
1449254894.0	15000.0	3.725	0.176	2.906	0.150
1449255494.0	600.0	3.370	0.151	3.158	0.149
1449256094.0	600.0	3.483	0.152	3.434	0.164
1449256694.0	600.0	3.582	0.157	2.896	0.143
1449257294.0	600.0	3.471	0.157	3.247	0.156
1449257894.0	600.0	3.489	0.156	3.327	0.154
1449258494.0	600.0	3.512	0.159	3.450	0.164
1449259094.0	600.0	3.300	0.148	3.718	0.179
1449259694.0	600.0	3.634	0.164	3.263	0.159
1449260272.5	578.5	3.844	0.176	3.462	0.173

List of Figures

Bibliography

[1] T. S. Petterson and P. Lefevre, "The Large Hadron Collider: conceptual design," Tech. Rep. CERN-AC-95-05-LHC, CERN, 1995.

[2] CERN, "The accelerator complex," October 2016.

[3] O. S. Brüning, P. Collier, P. Lebrun, S. Myers, R. Ostojic, J. Poole, and P. Proudlock, "LHC Design Report - Main Ring," *CERN*, vol. Vol. 1, 2004.

[4] F. Marcastel, "CERN's Accelerator Complex. La chaîne des accélérateurs du CERN," October 2013.

[5] P. Grafström and W. Kozanecki, "Luminosity determination at proton colliders," *Progress in Particle and Nuclear Physics*, vol. 81, pp. 97–148, 2015.

[6] W. Herr and B. Muratori, "Concept of Luminosity," tech. rep., CERN, 2006.

[7] K. Wille, *The Physics of Particle Accelerators: An Introduction.* Oxford University Press, 2000.

[8] R. Jones, "LHC Beam Instrumentation: Beam Profile Measurements (2/3)," tech. rep., CERN, 2014.

[9] B. Dehning, "CERN Wire Scanner Design," February 2009.

[10] M. Gasior, T. Lefevre, R. Jones, K. Wittenburg, and H. Schmickler, "Support Booklet for the Beam Instrumentation Course Warsaw - Poland," tech. rep., CERN, 2015.

[11] M. Sapinski, B. Dehning, A. Guerrero, J. Koopman, and E. Metral, "Carbon Fiber Damage in Accelerator Beam," Tech. Rep. CERN-BE-2009-028, CERN, 2009.

[12] A. Goldblatt, E. Bravin, F. Roncarolo, and G. Trad, "Design and performance of the upgraded LHC synchrotron light monitor," *Proceedings of IBIC2013, Oxford, UK*, 2013.

[13] F. Caspers, A. Goldblatt, A. Nosych, F. Roncarolo, G. Trad, C. Völlinger, and M. Wendt, "The LHC synchrotron light monitor BSRT," Tech. Rep. CERN-ACC-SLIDES-2014-0049, CERN, April 2014.

[14] M. Sapinski, W. Andreazza, B. Dehning, A. Guerrero, M. Patecki, and R. Versteegen, "The first experience with LHC Beam Gas Ionization Monitor," Tech. Rep. CERN-ATS-2012-286, CERN, 2012.

[15] The LHCb collaboration, "A Large Hadron Collider beauty experiment," Tech. Rep. CERN-LHCC-98-004, CERN, 1998.

[16] The LHCb collaboration, "LHCb reoptimized detector design and performance," Tech. Rep. CERN-LHCC-2003-030, CERN, 2003.

[17] The LHCb Collaboration, "The LHCb Detector at the LHC," *Journal of Instrumentation*, vol. 3, no. 08, p. S08005, 2008.

[18] The LHCb collaboration, "LHCb VELO (VErtex LOcator): Technical Design Report," Tech. Rep. CERN-LHCC-2001-011, CERN, 2001.

[19] M. Agari, N. van Bakel, C. Bauer, and et al., "Beetle—a radiation hard readout chip for the LHCb experiment," *Nucl. Instr. Meth. Phys. Res. Sect. A*, vol. 518, no. 1–2, pp. 468 – 469, 2004.

[20] BGV Collaboration, "BGV Twiki," 2012-2016.

[21] P. Hopchev, "A new device for the LHC: first conceptual design studies." BGV internal presentation, October 2012.

[22] Q. Veyrat, "BGV Full MC Simulation - Effects of additional material." BGV internal presentation, January 2014.

[23] O. Girard, "Beetle board attenuators and bgv fibre module light yield," tech. rep., EPFL, 2014.

[24] Q. Veyrat, "BGV Full MC Simulation - Particles fluence/dose on SiPM." BGV internal presentation, January 2014.

[25] The LHCb Collaboration, "LHCb Tracker Upgrade Technical Design Report," *Technical Design Report LHCb*, vol. 15, no. CERN-LHCC-2014-001. LHCB-TDR-015, 2014.

[26] G. Bregliozzi, N. Chritin, B. Dehning, and et al., "Beam Gas Vertex (BGV) Demonstrator of a Beam Profile Monitor in LHC," tech. rep., CERN, 2014.

[27] T. Kirn, R. Greim, W. Karpinski, and et al., "Production of Scintillating Fibre Modules for high resolution tracking devices," *PoS*, vol. TIPP2014, p. 108, 2014.

[28] Kuraray, "Plastic Scintillating Fibers." online, 12 2016.

[29] A. Kuonen, O. Girard, and G. Haefeli, "Characterisation of the Hamamatsu MPPC multichannel array for LHCb SciFi Tracker v.9.2014," tech. rep., EPFL, 2015.

[30] L. Eklund and LHCb VELO Group, "Control and Monitoring of VELO and Pile-Up Level 0 Electronics," tech. rep., CERN, 2005.

[31] O. Girard, L. An, A. Kuonen, H. Li, and G. Haefeli, "BGV fibre module read-out, signal correction and clustering," tech. rep., EPFL and Tsinghua University, 2016.

[32] G. Haefeli, A. Bay, A. Gong, H. Gong, M. Muecke, N. Neufeld, and O. Schneider, "The LHCb DAQ interface board TELL1," *Nucl. Instr. Meth. Phys. Res. Sect. A*, vol. 560, no. 2, pp. 494 – 502, 2006.

[33] ELMB group, "Embedded Local Monitor Board ELMB128," tech. rep., CERN, 2004.

[34] "CERN EOS Service," 2016.

[35] C. Barschel, "BGV blade DAQ network." BGV internal presentation, December 2014.

[36] D. Breton, D. Charlet, P. Robbe, and I. Videau, "SPECS: A Serial Protocol for the Experiment Control System of LHCb," tech. rep., Laboratoire de l'Accelerateur Lineaire (LAL), 2005.

[37] C. Gaspar and B. Franek, "Tools for the automation of large distributed control systems," *IEE Trans. Nucl. Sci*, vol. 53, 2006.

[38] F. Calheiros, P. Golonka, and F. Varela, "Automating the configuration of the control system of the LHC experiments," *Proceedings of ICALEPS07*, 2007.

[39] C. Gaspar, "LHCb's Experiment Control System." Presentation, September 2001.

[40] I. Mous, "Tuning of the timing of the LHCb VELO detector," Tech. Rep. CERN-LHCb-PUB-2010-006, NIKHEF and CERN, 2012.

[41] K. Akiba, "Description of the VELO timing system and its configuration," Tech. Rep. LHCb-PUB-2011-012, CERN, 2012.

[42] P. Buzhan, B. Dolgoshein, L. Filatov, A. Ilyin, V. Kantzerov, V. Kaplin, A. Karakash, F. Kayumov, S. Klemin, E. Popova, and S. Smirnov, "Silicon photomultiplier and its possible applications," *Nucl. Instr. Meth. Phys. Res. Sect. A*, vol. 504, 2003.

[43] M. Rihl, "Efficiency and uniformity of a sipm array combined with a light concentrator," Master's thesis, University of Vienna, 2012.

[44] V. Golovin and V. Savelev, "Novel type of avalanche photodetector with geiger mode operation," *Nucl. Instrum. Meth.*, vol. A518, 2004.

[45] O. Girard, "Optimisation and validation of the cooling design and read-out electronics for the LHC Beam Gas Vertex detector modules," tech. rep., EPFL, 2014.

[46] "ROOT v. 5.34," April 2016.

[47] "ROOT Class: TSpectrum," January 2000.

[48] A. Alici, G. Anders, N.Bacchetta, and et al., "Study of the LHC Ghost charge and satellite bunches for luminosity calibration," CERN-ATS-Note-2012-029 PERF (BCNWG Note 4), CERN, June 2012.

[49] V. Lebedev and V. Shiltsev, eds., *Accelerator Physics at the Tevatron Collider*. Springer, 2014.

[50] The LHCb Collaboration, "Precision luminosity measurements at LHCb," *Journal of Instrumentation*, vol. 9, no. 12, p. P12005, 2014.

[51] C. Barschel, M. Ferro-Luzzi, J. Gras, M. Ludwig, P. Odier, and S. Thoulet, "Results of the LHC DCCT calibration studies," Tech. Rep. CERN-ATS-Note-2012-026 PERF, CERN, May 2012.

[52] D. Belohrad, *Fast Beam Intensity Measurements for the LHC*. PhD thesis, Czech Technical University in Prague, 2010.

[53] C. Barschel, *Precision luminosity measurement at LHCb with beam-gas imaging*. PhD thesis, RWTH Aachen, 2014.

[54] S. van der Meer, "Calibration of the effective beam height in the ISR," Tech. Rep. CERN-ISR-PO- 68-31, CERN, 1968.

[55] T. Bohl, T. Linnecar, E. Chapochnikova, and J. Tückmantel, "Longitudinal emittance blow-up and hollow bunches with arbitrarily-shaped noise in the SPS as LHC testbed," Tech. Rep. CERN-AB-Note-2008-019, CERN, 2008.

[56] ALICE Collaboration, "ALICE luminosity determination for pp collisions at $\sqrt{s} = 13$ TeV," Tech. Rep. ALICE-PUBLIC-2016-002, CERN, June 2016.

[57] CMS Collaboration, "CMS luminosity measurement for the 2015 data-taking period," Tech. Rep. CMS-PAS-LUM-15-001, CERN, 2017.

[58] M. Schaumann and J. M. Jowett, "Bunch-by-Bunch Analysis of the LHC Heavy-Ion Luminosity," Tech. Rep. CERN-ACC-2013-0136, CERN, 2013.

Acknowledgements

Curriculum Vitae

Mariana Rihl

Work Experience

10/2017-present	**Systems Test Engineer**, **Cruise Automation**
	- Ensuring quality of autonomous vehicles by analysing test drive data.
09/2013-12/2016	**Graduate research assistant**, **CERN**
	- Ensured quality of all electronic data acquisition components for a new beam-imaging detector (beam-gas vertex detector, BGV) for the LHC.
	- Developed and integrated an automated control system with WinCC OA for the BGV.
	- Installation and system bring-up of the BGV in the LHC tunnel.
	- Data analysis for BGV commissioning and for the LHCb collaboration.
7/2011	**Intern**, **ASACUSA Experiment at CERN,**
	Stefan Meyer Institute of the Austrian Academy of Sciences
	- Data acquisition for studying the hyperfine structure of $\bar{p}$-helium.
05/2008-12/2011	**Business Analyst** (25hrs./week), **Microsoft Austria GmBH**
	- Budget planning and (OPEX-) performance oversight for the Austrian consumer business division.
	- Responsibility for financial month- and year-end close.
	- Developed a tool to improve forecast accuracy of marketing expenses by 50%.
09/2007-02/2008	**Intern**, **Deloitte Austria**
	- Preparation of annual audit, credit checks, SAP.
07/2007	**Intern**, **SAP Austria GmBH**
	- SAP skills training, managing of business partner data.
07-08/2006	**Intern**, **SAP Austria GmBH**
	- SAP skills training, managing of business partner data.
07-08/2005	**Intern**, **Baxter AG Austria**
	- general personal assistant tasks, completion of a publication database for the R&D division.

Education

04/2013-10/2017	**Ph.D. Student** in **Physics**
	Vienna University of Technology
	Thesis title: "Development of a non-destructive beam profile monitor based on scintillating fiber planes and SIPMs"
	Participation in following schools:
	CERN Accelerator School, Introduction to accelerators, RF technology, beam monitors
	School on Trigger and Data Acquisition, introduction to triggers, DAQ, VME and NIM standards
10/2005-12/2012	**Diploma student** in **Physics**
	University of Vienna, Magistra rerum naturalium
	Thesis title: "Efficiency and uniformity of a SiPM array combined with a light concentrator"
09/2004-06/2008	**Diploma studies "European economy and management"**
	Fachhochschule des bfi Wien, graduation with Mag.(FH) diploma
	Sept. - Dec. 2006: Participation in Erasmus programme
	ESC Dijon, France
06/2004	High school graduation with merit
	Musikgymnasium Vienna

Relevant Skills and Qualifications

Electronics Skills	Solid testing of (particle) detector electronics, debugging, signal verification (oscilloscope, function generators, etc.), familiarity with Gerber files, soldering
Software Skills:	Programming: Python, C, Unix/Linux shell scripting, LabView, WinCC OA (PVSS), MatLab
	Scientific Editing: LaTeX, QTIPlot, Origin, matplotlib,
	Other: Microsoft Office, VBA, Mac OS, Inkscape, Photoshop
Other skills	Electronics assembly, cooling technology, laser setup and operation, accelerator physics and engineering, project management, business controlling and economics, Austria-licensed snowboard instructor for beginner levels
Languages	English (fluent), French (fluent), German (native), Spanish (elementary proficiency)

Relevant publications as leading author

M. Rihl on behalf of the BGV Collaboration:
Employing Beam-Gas Interaction Vertices for Transverse Profile Measurements,
submitted to JACoW (2016).

M. Rihl on behalf of the LHCb and BGV Collaborations:
Imaging the LHC beams with silicon and scintillating fiber vertex detectors,
Nucl. Instrum. Meth. A, in press, doi:10.1016/j.nima.2016.04.051 (2016).

M. Rihl, S.E. Brunner, L. Gruber, J. Marton, K. Suzuki:
Efficiency and uniformity of a SiPM array combined with a light concentrator,
Nucl. Instrum. Meth. A, 732, 419-422 (2013).

Relevant presentations

Employing Beam-Gas Interaction Vertices for Transverse Profile Measurements,
International Particle Accelerator Conference, IPAC, Busan, Korea (2016).
Imaging the LHC beams with silicon and scintillating fiber vertex detectors,
Vienna Conference on Instrumentation (2016).
Efficiency and uniformity of a SiPM array combined with a light concentrator,
Vienna Conference on Instrumentation (2013).